Nanostructures for Coherent Light Sources and Photodetectors

Vinh Xuan Ho

Dissertation submitted to the faculty of the
Virginia Polytechnic Institute and State University
in partial fulfillment of the requirements for the degree of

Doctor of Philosophy
in
Physics

Vinh Q. Nguyen, Chair
Giti A. Khodaparast
Michael P. Cooney
James R. Mahan
Satoru Emori
James Gray

April 22, 2020
Blacksburg, Virginia

Keywords: Lasing, GaN:Er, Graphene Photodetector, Mid-infrared, Near-infrared

Nanostructures for Coherent Light Sources and Photodetectors

Vinh Xuan Ho

ABSTRACT

Large-scale optoelectronic integration is limited by the lack of efficient light sources and broadband photodetectors, which could be integrated with the silicon complementary metal-oxide-semiconductor (CMOS) technology. Persistent efforts continue to achieve efficient light emission as well as broadband photodetection from silicon in extending the silicon technology into fully integrated optoelectronic circuits. Recent breakthroughs, including the demonstration of high-speed optical modulators, photodetectors, and waveguides in silicon, have brought the concept of transition from electrical to optical interconnects closer to realization. The on-chip light sources based on silicon are still a key challenge due to the indirect bandgap of silicon that impedes coherent light sources. To overcome this issue, we have studied, fabricated, and characterized nanostructures including single semiconductor epilayers, multiple quantum wells, and graphene-semiconductor heterostructures to develop coherent light sources and photodetectors in silicon.

To develop coherent light sources, we reported the demonstration of room-temperature lasing at the technologically crucial 1.5 μm wavelength range from Er-doped GaN epilayers and Er-doped GaN multiple-quantum wells grown on silicon and sapphire. The realization of room-temperature lasing at the minimum loss window of optical fiber and in the eye-safe wavelength region of 1.5 μm is highly sought-after for use in many applications in various fields including defense, industrial processing, communication, medicine, spectroscopy and imaging. The results

laid the foundation for achieving hybrid GaN-Si lasers providing a new pathway towards full photonic integration for silicon optoelectronics.

Silicon photodiodes contribute a large portion in the photodetector market. However, silicon photodetectors are sensitive in the UV to near infrared region. Photodetection in the mid-infrared is based on thermal radiation detectors, narrow bandgap materials (InGaAs, HgCdTe) semiconductors, photo-ionization of shallow impurities in semiconductors (Si:As, Ge:Ga), and quantum well structures. Such technology requires complicated fabrication processes or cryogenic operation, resulting in manufacturing costs and severe integration issues. To develop broadband photodetectors, we focus on graphene photodetectors on silicon. Graphene generates photocarriers by absorbing photons in a broadband spectrum from the deep-ultraviolet to the terahertz region. Graphene can be realized as the next generation broadband photodetection material, especially in the infrared to terahertz region. Here, we have demonstrated high-performance hybrid photodetectors operating from the deep-ultraviolet to the mid-infrared region with high sensitivity and ultrafast response by coupling graphene with a p-type semiconductor photosensitizer, nitrogen-doped Ta_2O_5 thin film.

Nanostructures for Coherent Light Sources and Photodetectors

Vinh Xuan Ho

GENERAL AUDIENCE ABSTRACT

According to Moor's law, the number of transistors per die area doubles every 18 months with no increase in power consumption, which means that digital devices including smart phones and computers will become significantly faster and more energy-efficient than those of the previous generation. Photons (light) travel with the highest speed permitted by the known law of physics. The idea of optical interconnects, using photons instead of electrons, enables faster data transfer. Two important elements of the integrated circuits (ICs) based on photons are the coherent light source (laser) and the photodetector. We investigated the optical properties of erbium doped gallium nitride epilayers and multiple quantum wells grown on silicon and sapphire and demonstrated lasing from these materials at 1.5 μm. We also fabricated and characterized graphene photodetectors that can detect the light from the deep ultraviolet to the mid-infrared region. The results provided a new pathway towards full photonic integration for silicon optoelectronics. Besides, they are the heart of many important applications ranging from gas sensing, aerospace sensors and systems, thermal imaging, biomedical imaging, infrared spectroscopy, and lidar-to-optical telecommunications.

To My Beloved Family

Acknowledgments

The journey I have taken in my Doctoral education has consummated in the completion of this dissertation. I have successfully reached this finishing line thanks to the invaluable and immense support in numerous aspects of the following people who I am blessed to spend time with.

First and foremost, I would like to express my profound gratitude to my supervisor, Dr. Vinh Nguyen for his meticulous guidance and frequent encouragement throughout the program. It is him who opens the door of optoelectronics for me and shows me the effective research approach in this field. He is not only a wise and visionary advisor in academic research, but also a mentor in life who gave the foundation in his advice and the springboad in my favorable learning conditions to make a better me. His profound knowledge, rich experience, rigorous attitude, and challenging spirit have been great values for me as a student, a researcher, and a teacher also. I truly felt the greatest honor to be supervised by Dr. Nguyen during my entire student life at Virginia Tech. Largely thanks to Dr. Vinh Nguyen, what I have been through at the university's Physics department become precious life-changing experiences for me.

I am also very grateful to my other committee members, Dr. Giti A. Khodaparast, Dr. J. Robert Mahan, Dr. Michael P. Cooney, Dr. James Gray, Dr. Satoru Emori for all the constructive and helpful suggestions I receive. My special thanks go to Dr. J. Robert Mahan for his guidance on the language and organization for my presentation. I also would like to thank Dr. Camillo Mariani for his guidance through formatting my PhD dissertation.

My very special thanks go to my colleagues Yifei Wang and Yizhou Wang. As a team, we have worked on several projects. I especially appreciate Yifei's help during device fabrication with her careful preparation for transferring graphene very early in the morning. I also really want to thank Yizhou for designing the photomasks very fast and for willingly redoing the redesign whenever I needed the correction. Furthermore, I would like to thank Victor Dao, Luke Patrick, Prashant Pradhan for designing experiment components. I could not have accomplished so much without the help of my lab mates. Besides, I really want to thank all my colleagues in my research group: Abhishek Singh, Luan Doan, Jiarong Cui, Leslie Howe.

I would like to thank Betty for her help to my paperwork before I came to US and until I finished my PhD program. Special thanks also go to the Center for Soft Matter and Biological Physics, Department of Physics, College of Science and Graduate School, Micro & Nano Fabrication Laboratory at Virginia Tech for their support during my PhD program.

In addition, I am thankful to my previous supervisors, teachers and colleagues at ITIMS, University of Science and Technology (HUST), and at Faculty of Natural Science, Quy Nhon University (QNU) for the kindest help and support from the very beginning of my PhD study.

I am also grateful to "Vietnamese village" in Blacksburg, Virginia for the warm friendship, the help and the enjoyable parties in Thanksgiving, Christmas, New Year and several other occasions we have had in the past 5 years. Especially, I feel lucky to get to know Mr. Vinh, Mrs. Hạnh, Mr. Vân, Mrs. Đức, Hòa, Luận, Phương, Chương, Trí, and VietTech community. Thanks to my room-mate Tam Nguyen for many helps and for nice sightseeing trips together.

I would like to thank my close friends (Ngoc Lam, Xuan Minh, Thang Nguyen, Duc Tuong, Nguyen Binh, Huu Phong, Van Hung, Duy Khanh, Quoc Dai, Ngoc Tri, Thanh Hien) for support, and nice time together whenever I come back to Vietnam. Also, I am thankful to my brothers Hanh & Hung, who have cared for my parents when I am away.

I would like to express my deepest gratitude to my parents, who have unconditionally loved and cared for me since birth, and especially during my hard time in my pursuit of the PhD study up to now. Five years has been the longest time I have been away from home and also have made my parents worry most. To my beloved parents, with all of my love and respect, I would like to give you this dissertation as a gift of my five-year craft and would love you to share the honor and the pride of this achievement with me.

Kính gửi ba má,

Con xin cảm ơn ba má đã yêu thương và động viên con trong suốt thời gian 5 năm qua. Đó là khoảng thời gian con xa nhà lâu nhất và con cũng không về nhà ăn cơm cùng ba má vào những cuối tuần như khi còn làm ở Quy Nhơn, cũng làm cho ba má lo lắng nhiều. Tuy nhiên, khoảng thời gian con đã học được nhiều hơn, đã trưởng thành hơn. Với tất cả sự yêu thương và kính trọng, con xin kính tặng ba má tất cả những gì con viết trong quyển luận án này.

The author gratefully acknowledges the financial support from National Science Foundation (ECCS-1358564), the IRAD program from NASA Langley Research Center's Office of Chief Technologist, the Earth Science Technology Office (ESTO), NASA. A portion of the nanostructure fabrication was conducted at the Center for Nanophase Materials Sciences (Oak Ridge National Laboratory), which is a DOE Office of Science User Facility. And some experiments were performed at the National High Magnetic Field Laboratory, Tallahassee, Florida.

Vinh Xuan Ho

Blacksburg, April 22, 2020

Table of Contents

List of Figures

List of Publications

Journal papers

1. V. X. Ho, S. P. Dail, T. V. Dao, H. X. Jiang, J. Y. Lin, J. M. Zavada, and N. Q. Vinh *Temperature dependence studies of Er optical centers in GaN epilayers grown by MOCVD*, MRS Advances, 2, 135 (2017).
2. V. X. Ho, T. V. Dao, H. X. Jiang, J. Y. Lin, J. M. Zavada, S. A. McGill, and N. Q. Vinh *Photoluminescence quantum efficiency of Er optical centers in GaN epilayers*, Scientific Reports, **7** 39997 (2017).
3. V. X. Ho, T. M. Al Tahtamouni, H. X. Jiang, J. Y. Lin, J. M. Zavada, and N. Q. Vinh *Room-temperature lasing action in GaN quantum wells in the infrared 1.5 μm region*, ACS Photonics 5**,** 1308 (2018).
4. J. R. Mahan, N. Q. Vinh, V. X. Ho, and N. B. Munir, *Monte Carlo ray-trace diffraction based on the Huygens-Fresnel principle*, Applied Optics 57**,** D56 (2018).
5. V. X. Ho, Y. Wang, B. Ryan, L. Patrick, H. X. Jiang, J. Y. Lin, and N. Q. Vinh, *Observation of Optical Gain in Er-Doped GaN Epilayers*, Journal of Luminescence 221**,** 117090 (2020).

Conference papers

1. V. X. Ho, H. X. Jiang, J. Y. Lin, J. M. Zavada, and N. Q. Vinh, *Rare Earth doped GaN for photonic devices*, Advanced Photonics (IPR, NOMA, Sensors, Networks, SPPCom, PS)**,** ITh2C.5 (2017).
2. V. X. Ho, Y. Wang, M. P. Cooney, and N. Q. Vinh, *Graphene-Based Photodetector at Room Temperature*, Proceedings of SPIE 10729, 1072907 (2018) Nanoscience + Engineering
3. V. X. Ho, T. M. Al Tahtamouni, Y. Wang, H. X. Jiang, J. Y. Lin, J. M. Zavada, and N. Q. Vinh, *Telecommunication-Wavelength Lasing in Er-doped GaN Multiple Quantum Wells at Room Temperature*, Laser Congress 2018 (ASSL), ATu4A.2 (2018).
4. Y. Wang, V. X. Ho, P. Pradhan, M. P. Cooney, and N. Q. Vinh, *Graphene-Germanium Quantum Dot Photodetector with High Sensitivity*, Proceedings of SPIE 11088, 110888 (2019) Nanoscience + Engineering

Chapter 1

Introduction

In this chapter we present the motivation and the basic concepts concerning optical properties of erbium-doped gallium nitride toward a coherent light source as well as graphene optoelectronic properties for photodetection.

1.1 Erbium-doped gallium nitride

1.1.1 Motivation

The development of complementary metal oxide semiconductor (CMOS) based on silicon has achieved breakthroughs in electronic applications from computers, smartphones to automation today. Currently, by downscaling the size of devices and wires to the nanometer scale, silicon technology has offered the 7-nm technology node. The 5-nm and 3-nm nodes are expected in the foreseeable future, that requires revolutionary new process methodologies as well as innovative, new equipment.[1] However, the high integration of components (for instance transistors) can lead to the problems of thermal dissipation, bandwidth and crosstalk, which has the potential to break abruptly Moore's law. The optical interconnects between logic devices as well as data transportation can maintain the progress on the speed, computational power, and enhance functionality of integrated circuits (ICs), and so Moore's law will be kept on track. Obviously, photons are much faster and more efficient than electrons. The silicon photodetectors, waveguides,[2] modulators,[3] optical switches and optical couplers have been well developed on silicon wafer for the optical interconnects. A coherent light-source is the important part that we are still missing. Toward fully integrated optoelectronics circuits based on Si-CMOS technology, persistent efforts have been devoted to realizing efficient light sources from silicon. However, on-chip coherent light sources based on silicon are still a challenge due to the indirect bandgap of silicon.[4, 5, 6, 7]

Recent advances in growing GaN:Er film on Si and observation of strong luminescence at the wavelength of 1.5 μm that matches the minimum loss window of optical fibers will open opportunities to develop the coherent light sources on Si. Thanks to an interesting feature of rare earth (RE) elements that the 4f-shell is partially filled while the outer shells are fully filled, the Er^{3+} ion can emit sharp, atomic-like spectra, and its optical and magnetic properties do not depend on the host materials.[8, 9] In the past, the goal of obtaining 1.5 μm Er-doped semiconductor lasers was unsuccessfully attempted using crystalline Si,[4, 5, 6, 7] latter of SiO_2:Er sensitized with Si nanocrystals,[10, 11, 12, 13] or GaAs and AlGaAs because of the strong thermal quenching effect occurring in narrow and/or indirect bandgap materials.[14, 15] Er-doped SiO_2 and Nd-doped YAG based materials are attractive for telecom application and high-power lasers. In these materials, resonant excitation is required for rare-earth elements. Excitation cross-section of the resonant excitation is several orders of magnitude lower than that of the band-to-band excitation.[16] This limitation is a big obstruction to further progress towards room-temperature 1.5-μm lasers based on Er in micro-optoelectronic applications.

Er-doped GaN film has been successfully grown on Si by the MOCVD method with good crystallinity and a high percentage of Er^{3+} optically active centers, resulting in predominant photoluminescence (PL) at room temperature.[17, 18, 19] GaN semiconductor has been an attractive host material for RE because of its direct and wide (~3.3 eV) bandgap properties. Er-doped GaN material exhibits a significant low degree of thermal luminescent quenching, and strong emission at room temperature under either electrical or optical excitation.[14, 16, 20] GaN possesses a high thermal conductivity ($\kappa \approx 253$ W/m.K)[21], and a low thermal expansion coefficient ($\alpha \approx 3.2 \times 10^{-6}$ K^{-1})[22, 23, 24] compared with other semiconductors and ceramics including silicon ($\kappa \approx 130$ W/m.K, $\alpha \approx 2.6 \times 10^{-6}$ K^{-1}),[24, 25] GaAs ($\kappa \approx 50$ W/m.K, $\alpha \approx 6.5 \times 10^{-6}$ K^{-1})[25], and YAG ($\kappa \approx 12$ W/m.K, $\alpha \approx 6.4 \times 10^{-6}$ K^{-1})[26, 27]. Thus, we can obtain high energy and high-power lasers in the Er-doped GaN material.

Silicon photonics combined the two most important inventions related to semiconductors: the silicon integrated circuit and semiconductor laser/photodetection. Silicon photodiodes are used for photodetection in the ultra-violet, visible and near infrared regions, because Si is transparent at wavelengths above 1.1 μm. Therefore, to obtain optoelectronic integrated circuits on a silicon chip, we need suitable photodetectors besides the light source. Photodetection at a wavelength of 1.5

μm and beyond are available with many options. However, such technology requires complicated fabrication process or cryogenic operation, resulting in manufacturing costs and severe integration issues. To overcome this issue, we have focused on the study of graphene-photodetectors on silicon that is compatible with CMOS technology. We will discuss the graphene-photodetector on silicon in Section 1.2.

1.1.2 Energy transfer processes

Under the photo-excitation process, photons excited electrons in matter from the ground state to the excited states. Both electron and hole are bound to each other forming either a free exciton or a bound exciton (BE). Free excitons are neutral; thus, they can move easily in the crystal. BEs typically are localized at specific positions. These excitons can transfer their energy to nearby RE ions.

1.1.2.1 RE ion excited by free excitons

Under over-bandgap excitation, electrons and holes are produced in the conduction and valence bands. These electrons and holes can create free excitons that interact with a RE ion via non-radiative energy transfer. The electron and hole are separated over several lattice constants, the exciton wavefunction is strongly delocalized and the exciton can move freely inside the crystal.

1.1.2.2 RE ion excited by bound excitons

The interaction between BEs and RE ions is the most dominant excitation mechanism in the RE-doped semiconductors. BEs can be formed through an over- or below-bandgap excitation. The electrons or holes can be captured by the RE ions or an impurity/local defect nearby the RE ions. If an electron in the conduction band can be taken by an acceptor-like trap in the bandgap, it will then attract a free hole in valance band by Coulomb attraction. A BE is formed. The BEs can also be created from donor-like trap capturing a hole, then hole attracts an electron. The spatial extension of the BEs can be approximately restricted to a single unit cell.

a) Over-bandgap (band-to-band) excitation

In Fig. 1.1, a free electron is created under band-to-band excitation (step 1). It is captured by an acceptor-like trap in the bandgap (step 2). This electron will attract a hole in valance band (step 3). In a final step, the non-radiative recombination of electron and hole in BE happens, then

transfers energy to the RE ion (step 4). In the excited RE ion, the electron will relax to the lower excited states, resulting in the emission of photon (step 5).

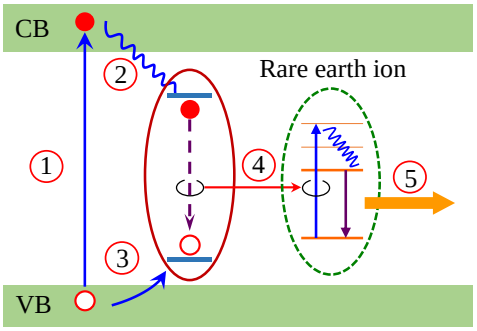

Figure 1.1: *Illustration of the band-to-band excitation process*

b) Below-bandgap excitation

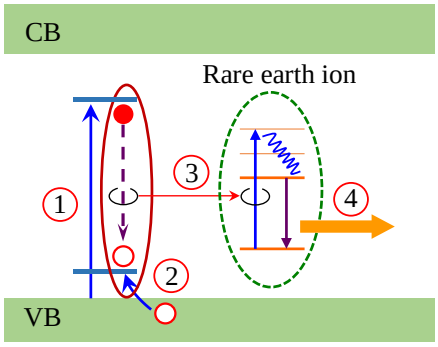

Figure 1.2: *Illustration of the below-gap excitation process*

BEs can also formed through below-bandgap excitation as Fig. 1.2. In this process, an electron is directly excited from the valance band to an acceptor-like trap (step 1). This electron will attract a free hole in valance band to create a BE (step 2). Next, energy is transferred to the RE ion from the non-radiative recombination of electron and hole in BE (step 4). The relaxation of excited RE ion results in light emission (step 5).

1.1.3 Energy "back-transfer" process

The reverse of the transfer energy process in the RE ion is an energy "back transfer". It involves the de-excitation of excited RE ion by transferring their energy to the deep defect level. It is believed to be responsible for the decrease of photoluminescence intensity in these systems.

1.1.4 Two kinds of optical centers in rare earths doped semiconductors

There are two important types of RE-related BEs. The first is the RE ion acting as an acceptor-like trap by capturing first an electron, and next attracting a hole as Fig. 1.3. (a). The second is the electrically active local defects nearby RE ion (for example a vacancy) acting as acceptor-like trap catching an electron, then a hole as shown in Fig. 1.3. (b).

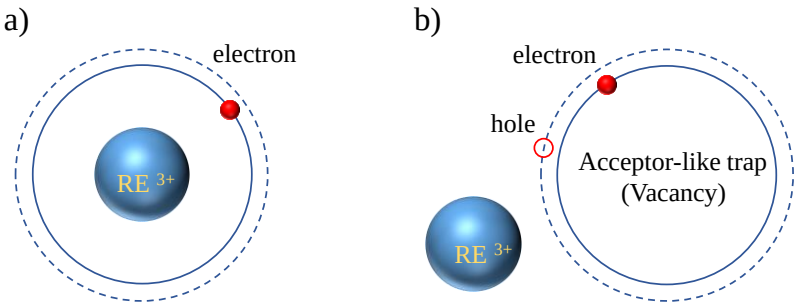

Figure 1.3: *Illustration of two kinds of RE-related BEs: (a) RE ion as an acceptor-like electron trap catching an electron, and then a hole (RE^{3+}, e) h. (b) Acceptor-like trap (local defect such as a vacancy) binding an exciton near a RE ion.*

Typically, in the first type of RE-related BEs, the RE ion is the isolated optical center that occupies substitutional site, and so it is considered as an isoelectronic impurity center. We call it an **isolated RE optical center**. This center can be excited by either resonant or band-to-band excitation. Under the excitation, an electron can be trapped at the isolated optical center by a local core potential. Next, a hole can be attracted by the Coulomb field of the electron. The electron and the hole will recombine non-radiatively to transfer energy to the RE ion.

In the other type of RE-related BEs, the RE ion can be excited by an electrically active defect nearby. This defect captures the exciton, and subsequently transfers energy to the nearby RE ion. It can only be observed through the over-bandgap excitation of the host, which involves a BE. This RE optical center is called a **defect related RE optical center**.

1.2 Graphene-based Photodetectors

1.2.1 Motivation

The ability to convert light into electrical signals is the heart of many important applications ranging from gas sensing, aerospace sensors and systems, thermal imaging, biomedical imaging, infrared spectroscopy, and lidar-to-optical telecommunications. The larger scale and diversity of application areas in the infrared are growing. The photodetection platform with high speed, efficient performance, complementary metal-oxide-semiconductor (CMOS) integrability, low costs and ultra-broadband wavelength range demands more urgent attention.

In the past, scientists knew one-atomic-layer crystal graphene existed, and even the pioneering work of Frindt and Yoffe produced 2D layers of MoS_2 in 1963,[28] then the optical properties of single layers of MoS_2 has been reported since the 1980s.[29] However, no one had worked out how to obtain single-layer graphene from graphite, until Geim and Novoselov frequently held "Friday night project" – This did not relate to the duty of their day job. The two scientists successfully obtained single-layer graphene on one Friday in 2004.[30] This is the interesting story about how graphene was discovered. Their experiment had led to graphene being isolated for the first time. Graphene has been paid extensive attention for research on its unique optoelectronic properties for both fundamental and experimental studies.[30, 31] It can generate photocarriers by absorbing very broadband spectra from deep-ultraviolet, visible, near-infrared, mid-infrared up to the terahertz region.[32] Moreover, graphene possesses the ultra-high carrier mobility enabling it to convert photons or plasmons to electrical signal quickly.[33] Graphene enables tuning the absorption via chemical doping and wavelength-independent absorption.[34, 35] The ability to integrate into highly mature silicon-based platform for optoelectronics is compatible. Therefore, extensive effort has been devoted to developing graphene-based photodetectors to realize the next generation broadband photodetectors, especially in the infrared and terahertz regions. Several applications have been addressed and results of research were already competitive with existing technology. However, more intensive studies are necessary to obtain the high-performance graphene-based photodetectors comparable to commercial ones.

In the rest of this section, we review the basic optoelectronic properties of graphene including its band structure, transport properties and optical properties. Next, we discuss the advantages and disadvantages of graphene to realize its application in photodetection. After that, several strategies

emerge to improve the performance of graphene-based photodetectors. Finally, the key figures-of-merit for photodetectors needed to understand experimental results in Chapter 6 are discussed.

1.2.2 Relevant graphene properties

1.2.2.1 What is graphene?

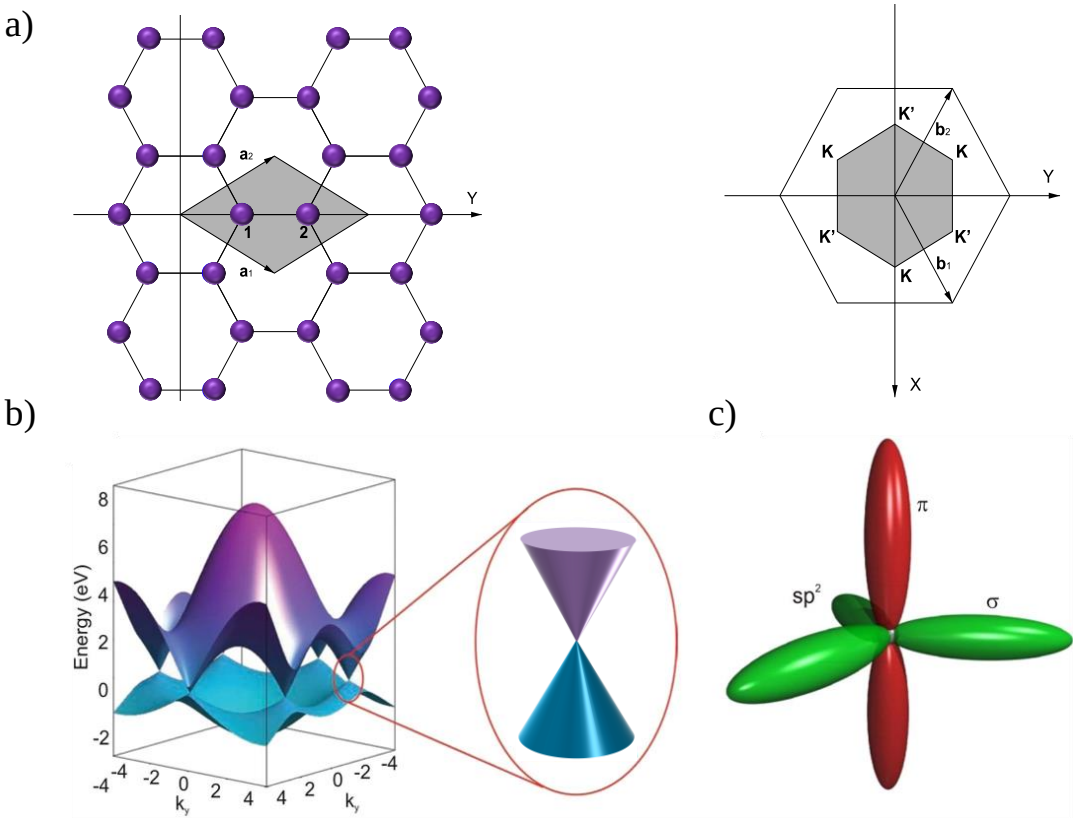

Figure 1.4: (a) Graphene and its reciprocal lattice. (b) the band structure of graphene and the energy band close to one of Dirac points (c) σ- and π-orbitals of one carbon atom in graphene [36, 37, 38]

Graphene is a single layer of carbon atoms arranging hexagonal lattice with the lattice constant a = 1.42 Å as Fig. 1.4a. The reciprocal lattice is shown in Fig. 1.4a. The full band structure of graphene is presented in Fig. 1.4b. [36, 37] This is first calculated by using the tight binding model by P. R. Wallace.[38] The valance band and conduction band touch only at the Brillouin zone corners. These points are known as Dirac points.[36] The Fermi level for undoped graphene is at the Dirac point. The Fermi level can be shifted by doping with impurities. Thus, graphene is called a zero-bandgap semiconductor, or a semi-metal with no band overlap. Carbon has four valance electrons in the outer shell. In graphene, each carbon atom uses three electrons for chemical bonding with

three neighbor atoms in the 2D plane. This bonding is referred as σ-bonding that extremely localized and does not contribute to the electronic conduction. The fourth electron which is called the π-electron is non-localized. These π-electrons of carbon atoms contribute to the electronic conduction properties and weak Van-der-Waals force between two layers of the graphene.

1.2.2.2 Electrical transport property: mobility

The electron dispersion near the Dirac points is linear rather than parabolic. The carriers act as relativistic massless particles with effective velocity of 10^6 m/s. Graphene possesses a mobility much higher than that of traditional semiconductors at room temperature because of high crystallinity and low scattering rate between electrons and intrinsic phonons. In theory, this value can reach 250,000 $cm^2v^{-1}s^{-1}$ at room-temperature.[36, 35]

However, the carrier mobility depends on the surface that graphene is transferred on to, and the fabrication process on graphene. Graphene capsulated by two layers of h-BN has the carrier mobility of about 140,000 $cm^2v^{-1}s^{-1}$.[39] The carrier mobility of exfoliated graphene on SiO_2 substrate in ultra-high vacuum reduces to between 40,000 to 60,000 $cm^2v^{-1}s^{-1}$,[40, 41] which compares favorably with the best InAs and InSb field-effect transistors.[42] The epitaxial graphene (or chemical vapor deposited (CVD) graphene) on SiC substrate is below 10,000 $cm^2v^{-1}s^{-1}$. However, air exposure and processing contaminations degrade the mobility of graphene. The carrier mobility of graphene on Si/SiO_2 under fabrication conditions was around few thousand $cm^2v^{-1}s^{-1}$.[43] Those values are still larger in comparison with electron mobility in Si ($\mu_{Si,\,e}$ = 1500 $cm^2v^{-1}s^{-1}$).

1.2.2.3 Optical properties

Monolayer graphene absorbs 2.3% of incident light in the visible and near infrared region. This value is significant for one layer of atoms.[34] The absorption of graphene is independent on any material parameters, depending only on the universal constants.[32, 34] For monolayer graphene, this value is πα, where α is the fine structure constant, h is Planck constant.

$$\alpha = \frac{\pi e^2}{2h} = \frac{1}{137}$$

The absorption of a few graphene layers increases linearly by adding a 2.3 % absorption for each monolayer. The resonance absorption peaks appear in a few layers of graphene instead of featureless spectrum of monolayer graphene. This originates from the change of 2D band structure

of few-layer graphene. Electrons in few-layer graphene have finite masses and are described by pairs of hyperbolic bands.[44]

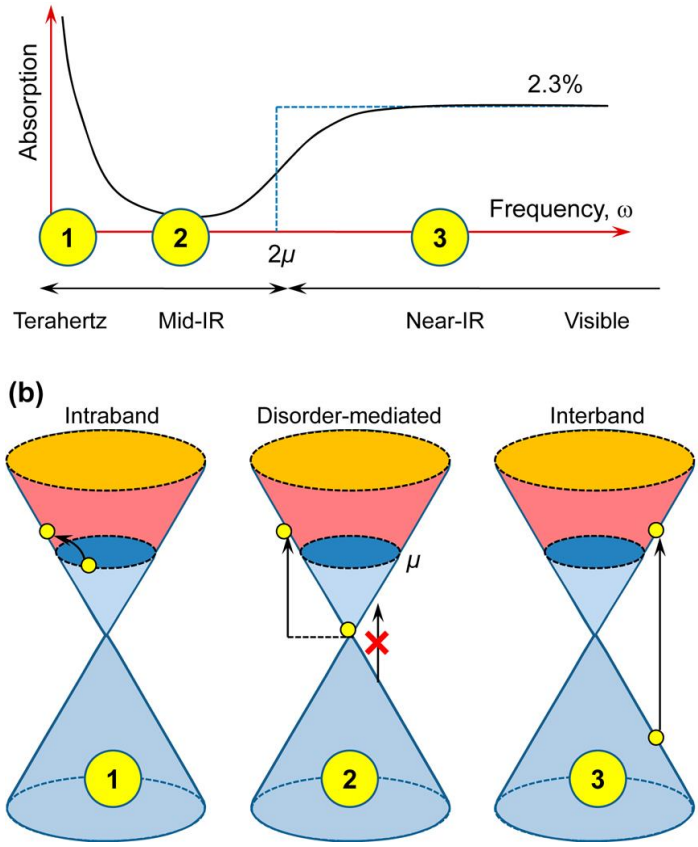

Figure 1.5: *(a) Absorption of n-type graphene, (b) optical transition of graphene from visible to Terahertz region. Reprinted with permission from T. Low and P. Avouris, ACS Nano 8 (2), 1086 (2014). Copyright (2014) American Chemical Society.*

The absorption of graphene with finite doping is presented in Fig. 1.5. There are two optical transition processes: inter-band and intra-band. The photons with energy smaller than $2E_F$ (Fermi energy) cannot be absorbed. Free carriers in such finite doped graphene is around 0.001 to 0.01 per atom, or doping concentration of 10^{12} to 10^{13} cm^{-2}. It can obtain 0.1 per atom for solid electrolyte gating. However, these values are smaller than that of 1 per atom for noble metal. The chemical potential of E_F smaller than 1 eV (or 1.238 μm) are calculated based on doping concentration.[45] Therefore, Pauli-blocking will occur at mid-infrared (Mid-IR) region, and so the absorption is minimal. This is the challenge in utilizing graphene for Mid-IR application. Absorption in the visible to near-infrared (near-IR) comes from inter-band process, about 2.3%,[34]

while the intra-band process is responsible for absorption in the Mid-IR and Terahertz (THz) frequency.[46]

1.2.3 Graphene-based Photodetectors

In this section, we will discuss the advantages and the disadvantages of graphene for broadband photodetection. We also give the overview of graphene-based photodetector research.

1.2.3.1 Graphene as a prospective candidate for broadband photodetection

a) Advantages

First, graphene with linear dispersion at near Dirac point and zero bandgap allows tuning of the photodetection range from **the visible to the terahertz**.

Second, the extremely high carrier mobility of graphene provides **high level of speed response** for detectors.[39, 47] So far, the highest reported speed operation for a graphene photodetector is 100 Gbit/s that corresponds to a bandwidth of 76 GHz.[48]

Third, graphene photodetectors can work at **room temperature** as well as being **compatible with CMOS photonics** technology.[49] The commercial photodetector in mid-infrared based on III-V InGaAs or HgCdTe can cover a detection range of up to 10 μm, but they require complicated integration and severe manufacturing costs. Graphene, however, is ultra-low-weight and flexible.[50, 51] It is suitable for seamless integration in various substrates via a transferring graphene process. Besides, graphene is now successfully grown on large sheet of copper foil using the physical vapor deposition (PVD) method, which enables fabricating devices of the **industrial scale with lost costs**.

b) Disadvantages

First, the **absorption of monolayer graphene is about 2.3%** of the incident light. Although high for only one layer of atoms for any materials, it is still very low for photodetection applications. [34]

Second, the **short lifetime of photocarriers**, about few picoseconds, allows ultra-fast response in light detection. However it leads to the rapid recombination of photocarriers.[52] The photoactive area of the detector will be small, typically about 2 μm from the metal contacts.

Third, **high dark current** of graphene photodetectors is due to the gapless nature of graphene, which leads directly to high shot noise and therefore produces high noise floor. In the other words, all of them result in low sensitivity of the graphene detector.

1.2.3.2 Progress on graphene photodetector research

Metal-graphene-metal photodetectors in which photocurrent is generated at the interface of metal and graphene were the first class of photodetectors. Their responsivity was below 1 mA/W.[53] There are significant efforts on developing graphene-based photodetectors to overcome the extremely low responsivity. Here, we discuss several prospective strategies.

1.2.3.2.1 Graphene detectors based on plasmons or field concentration

The integration of graphene and plasmonic nanostructures or micro cavities can enhance the absorption to more than 60% of incident light, thereby increasing the responsivity by up to tens of mA/W.[54] There are several approaches such as integration into optical microcavity, optical waveguide[55] and field enhancement by plasmonics. Here, field enhancement can come from metal nanostructures on graphene[56] or from graphene nanoribbons[46] where the intrinsic collective charge oscillations of electrons occur. The enhancement of responsivity has been achieved. By designing the geometry of nanostructures to resonate at certain wavelengths, the plasmonic enhanced graphene photodetectors are utilized for selective wavelength amplification that allows light filtering and detection. However, this also limits broadband detection range.

1.2.3.2.2 Hybrid graphene – semiconductor nanomaterials photodetectors

In this platform, photoconductive gain has been employed to enhance the responsivity through constructing hybrid graphene-colloidal quantum dots (CQD). Typically, the colloidal quantum dots (Si, PbS, PbSe, …) are integrated with a graphene phototransistor. The quantum dots (QDs) are light absorbers while graphene serves as a high-speed carrier transport channel. Under illumination, electron-hole pairs are generated at the interface of graphene and the QDs. One type of carrier, for example electrons, is trapped at interface of the graphene-QD with long lifetime ranging from the millisecond to the second scale. Under the applied bias between source and drain, holes are recirculated because of the fast transit time in the graphene channel. Thus, a single electron-hole pair generated in the QDs will create multiple holes in the graphene channel. This

phenomenon called photoconductive gain enhances the responsivity up to 10^9 A/W for Si-CQDs,[57] and 10^8 A/W for PbS QDs.[58]

However, this technique is characterized by three problems. First, the long lifetime of electrons in the trap centers causes a slow response time on the second scale. Second, the absorption happens in the quantum dots. This relates to the large bandgap of quantum dots, and results in a reduction of photodetection range. Third, the dark current is still high.

Therefore, the hybrid graphene-QDs holds potential for visible and short-wavelength infrared applications. It allows detection at very low illumination intensity. It also can be applied for single-photon detection that requires an ultra-high gain.

1.2.3.2.3 Integration of graphene and transitional metal dichalcogenides photodetectors

Transition metal dichalcogenides (TMDs) are mechanically flexible and permit easy processing. The optoelectronic properties of TMDs depend on the thickness, or the number of layers. The bandgap of TMDs can be tuned by changing the number of layers, which allows detection in different wavelength regions. The integration of TMDs and graphene in heterogeneous stacks and hybrid devices is a promising approach.

In the hybrid devices, the combination of TMDs, such as MoS_2 and graphene, was demonstrated in which TMDs provide visible light absorption and charge trapping.[59, 60] The detector response was up to 1 Hz, owing to the trap lifetime of 1 s. The responsivity in the visible region at room temperature is 10^8 A/W.[60]

In the heterogeneous-structure devices, the TMDs serve as photoactive materials, which are capsulated by two layers of graphene. Graphene is utilized as work-function tunable electrodes. Electron-hole pairs are generated in TMDs, and separated between two graphene layers, thus photocurrent is produced. TMDs are h-BN, MoS_2 and WS_2. The photo-responsivity increased to around 0.1 A/W.[61, 62] This heterogeneous structure also addressed the small photoactive area issue.

1.2.4 Key figures-of-merits for photodetectors

Various figures-of-merits used to characterize the performance of infrared detectors were written in numerous texts and journals such as The Infrared Handbook[63] by Wolfe and Zissis, Fundamentals of Infrared Detector Operation and Testing[64] by Vincent, and Fundamentals of

Photonics[65] by Saleh. We focus on these figures-of-merits used for testing our graphene-based photodetectors as follow.

1.2.4.1 Quantum efficiency

The quantum efficiency η of a photodetector is the probability that a single photon incident onto the detector will generate an electron-hole pair contributing to the photocurrent of detector. Not all incident photons produce photocarrier pairs to contribute to the photocurrent. This is because

- Some electron-hole pairs created near the surface of photodetectors recombine due to numerous recombination centers at the surface.
- Some photons are reflected at the surface of detectors
- Some fail to be absorbed in the active area due to depth of materials on the photodetector.

The quantum efficiency can be expressed as:

$$\eta = \delta(1 - r)\left(1 - e^{-\alpha d}\right)$$

where the first factor δ is the fraction of electron-hole pairs that avoid the recombination at the surface and contribute to the detector current. The second factor is the effect of reflection at the surface with r is the optical power reflectance. The third factor is the fraction of the photon flux absorbed in the materials of detector. The coefficient α is absorption coefficient of materials and the photodetector depth is d. The quantum efficiency defined above is called the external quantum efficiency (EQE).

Typically, there are two types of quantum efficiency. The second is internal quantum efficiency (IQE). IQE is the ratio of the number of charge carriers generated by the photodetector to the number of photons of a given energy that illuminate the photodetector from outside and are absorbed by the photodetector. Thus, IQE is equal to EQE divided by the absorption coefficient α.

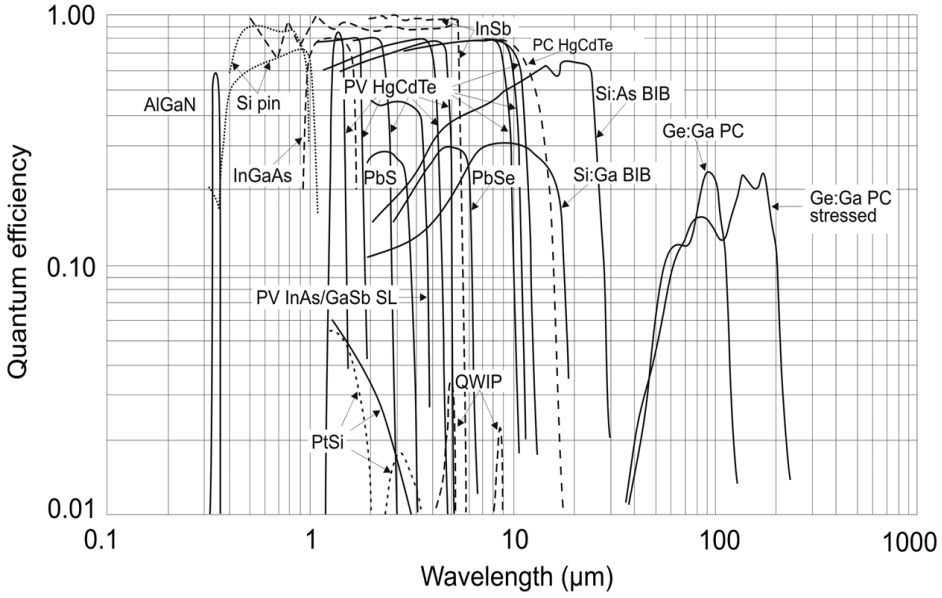

Figure 1.6: *Quantum efficiency of different detectors.*[66]

1.2.4.2 Responsivity

Responsivity R, one of most important parameters for photo-detecting devices, is defined as the ratio of generated photocurrent to the optical power incident to the detectors. Responsivity can be expressed by

$$R = \frac{I_{ph}}{P_{in}} = \frac{I_{light} - I_{dark}}{P_{in}}$$

Where, I_{light} and I_{dark} is the current from photodetectors with and without illumination. $P_{in} = \frac{hc}{\lambda}\phi$ is the irradiation optical power at the wavelength λ with ϕ photon flux (photons per second). I_{ph} is the photocurrent. If each photon can generate one electron-hole pair in photodetector, the photocurrent is $I_{ph} = q\phi$ with charge q. However, the external quantum efficiency of the detector is η, so the photocurrent is $I_{ph} = \eta q\phi$. The relation between responsivity and external quantum efficiency is

$$R = \frac{I_{ph}}{P_{in}} = \frac{\eta q}{hf} = \eta\frac{q\lambda}{hc}$$

1.2.4.3 Response time

The response time exhibits the response speed of the photodetector to the incident radiation signal. It includes the rise-time and the recovery time. The former is the time required to from 10% to 90% of the net photocurrent, and the latter is the time required to fall from 90% to 10% of the net photocurrent.

1.2.4.4 Photoconductive Gain

Photoconductive gain is the generation of multiple charge carriers per one incident photon, which is important to obtain a high responsivity photodetector. For graphene photodetectors, one photogenerated electron or hole can circulate many times in the graphene channel because of the long carrier lifetime (T_{life}) at the interface of graphene and absorber material, and the short drift transit time ($T_{transit}$) of carrier through the graphene channel. Transit time depends on applied bias voltage (V_{bias}), carrier mobility μ in the graphene channel of length L. Photoconductive gain can be expressed as

$$G = \frac{T_{life}}{T_{transit}} = \frac{T_{life}}{\frac{L^2}{\mu V_{bias}}} = \frac{\mu T_{life}}{L^2} V_{bias}$$

The gain can also define the average number of electrons or holes in a circuit per electron-hole pair. The photocurrent $I_{ph} = \eta q \phi G$. The relation between responsivity and gain is thus

$$R = \frac{I_{ph}}{P_{in}} = \frac{\eta q G}{hf} = \eta G \frac{q\lambda}{hc}$$

1.2.4.5 Noise equivalent power

Noise equivalent power (NEP) is defined as the signal power that gives a signal-to-noise ratio of one in a one hertz output electrical bandwidth. The unit of NEP is given in watts per square root of hertz (W/√Hz). The NEP expresses the sensitivity of the photodetector; in the other words, the weakest optical signal can be detected by photodetectors. NEP is given by

$$NEP = \frac{P_{in}}{\sqrt{B}} = \frac{i_{noise}}{R}$$

where P_{in} is the incident power when signal-to-noise ratio is 1, B is the electrical bandwidth of 1 Hz, and i_{noise} is the device noise current. NEP have been examined by considering the 1/f noise, shot noise and thermal noise.

The noise current density of $1/f$ noise is calculated by analyzing the noise in the dark current waveform for the photodetector. The dark current waveform was acquired by a current preamplifier with a sampling rate of 1 Hz. The noise current $S_I(1/f)$ of 1/f noise is given by

$$S_I(1/f) = \frac{1}{\sqrt{F_s N}} \sqrt{\langle |I(f)|^2 \rangle}$$

where $I(f)$ denotes the discrete Fourier transform of the dark current waveform $I(t)$, F_s is the sampling rate, and N is the number of data points.[67]

The shot noise is estimated as

$$S_I(\text{shot}) = \sqrt{2qI_{dark}}$$

where q is the elemental charge, and I_{dark} is the dark current of the device.[67]

The thermal noise is calculated by using Nyquist's equation,

$$S_I(\text{thermal}) = \sqrt{4k_B T/R}$$

where k_B is Boltzmann's constant, T is the temperature, and R is the differential resistance of the device in the dark. The units of S are A $Hz^{-1/2}$.

Therefore, the NEP value is achieved by formula

$$\text{NEP} = \frac{P_{in}}{\sqrt{B}} = \frac{i_{noise}}{R} = \frac{\sqrt{S_I(\text{shot})^2 + S_I(\text{thermal})^2 + S_I(1/f)^2}}{R}$$

1.2.4.6 Specific detectivity

Specific detectivity (D*) is equal to the reciprocal of noise-equivalent power (NEP), representing the sensitivity of capturing weak signal.

$$D^* = \frac{\sqrt{A}}{\text{NEP}}$$

where, A is the effective area of the photodetector. D* is commonly expressed in Jones units (cm √Hz / W). It is used to compare the same type photodetector having different effective areas. The specific detectivity curves for commercial photodetectors in the near IR up to THz regime are presented in Fig. 1.7.

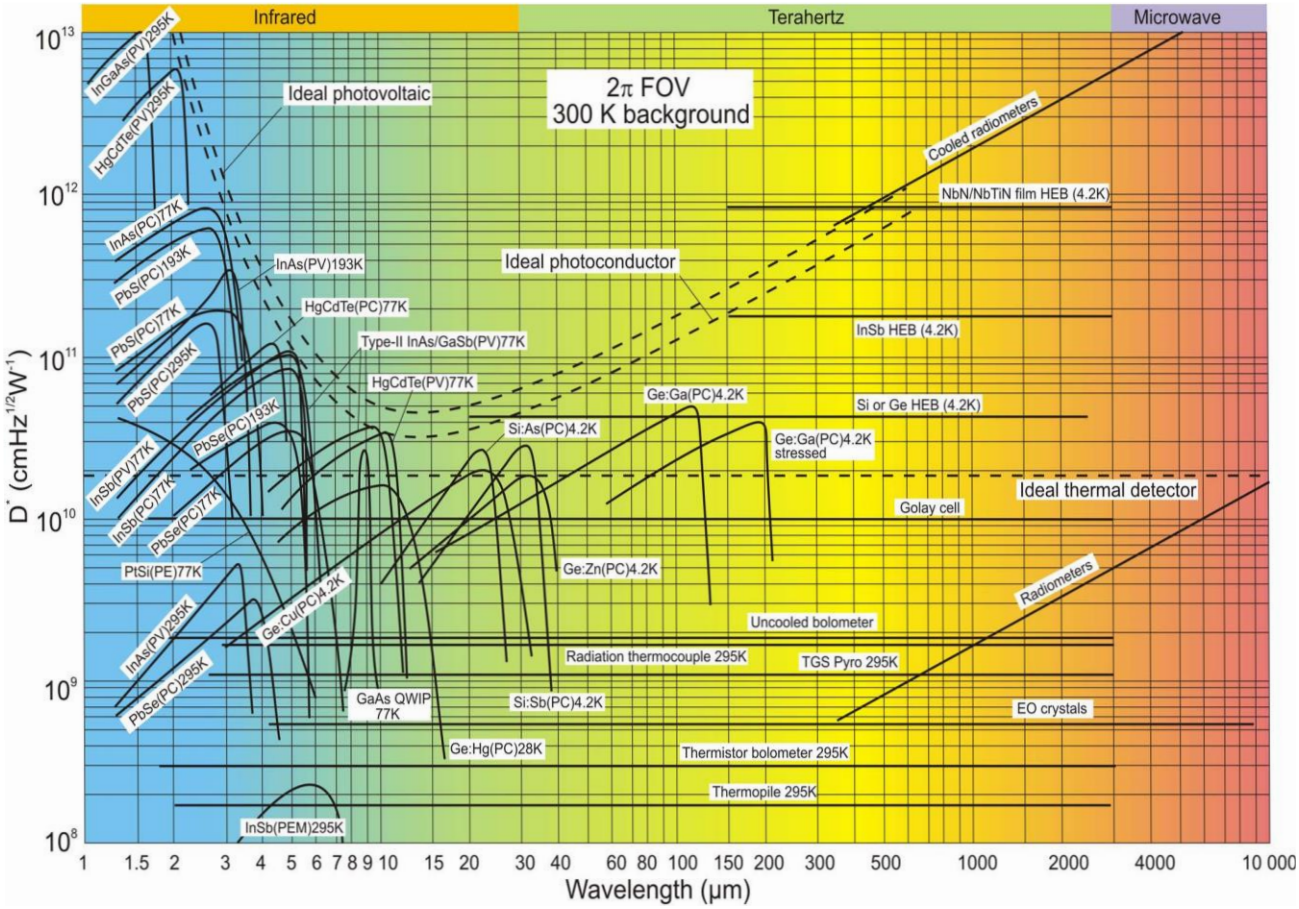

Figure 1.7: *Specific detectivity, D*, of commercial photodetectors in the near-IR to THz region. Reprinted from Prog. Quantum Electron. 36, Rogalski, "Progress in focal plane array technology", pp. 342-473, Copyright 2012, with permission from Elsevier.*

1.2.4.7 Linear dynamic range

The linear dynamics range is defined as $\mathrm{LDR} = 20\log\left(\frac{I_{ph}^{*}}{I_{dark}}\right)$, where I_{ph}^{*} is the photocurrent under illumination intensity of 1 mW cm^{-2} and I_{dark} is the dark current. In practice, it is desirable to have a large LDR for a photodetector capable of detecting both weak and strong light.

Chapter 2

Fabrication and Experiments

This chapter describes the sample preparation, the experimental methods and setups applied to realize the coherent light sources from Er-doped GaN epilayer and multiple quantum well structures. There are two main measurement techniques including photoluminescence and optical gain. This chapter also provides the main fabrication processes in the Virginia Tech cleanroom, and characterization tools for graphene-based photodetectors.

2.1 Sample preparation:

Our Er doped GaN epilayer and multiple quantum well samples were prepared by the group of professors H. X. Jiang and J. Y. Lin in the Texas Tech University. The fabrication process is described in detail as below.

2.1.1 MOCVD Growth of Er doped multiple GaN quantum wells

For the growth of Er doped GaN/AlN multiple quantum wells (MQWs:Er), the aluminum source was trimethylaluminum (TMA), the gallium source was trimethylgallium (TMGa), and the nitrogen source was ammonia (NH_3). Tris(isopropylcyclopentadienyl)erbium (TRIPEr) was used for the in-situ Er doping. The precursors for Ga and Er were held in stainless steel bubblers at 3 ^oC and 60 ^oC, respectively, and were carried into the reactor by H_2 gas. The growth started with a thin (30 nm) AlN buffer layer (buffer 1) grown at 950 ^oC and 30 mbar, followed by a second 100 nm AlN buffer layer (buffer 2) at 1100 ^oC grown at 30 mbar, and a 1.0 μm AlN template grown at 1325 ^oC and 30 mbar. It was then followed by the growth of the MQWs:Er structure of Er doped

GaN quantum wells and undoped AlN barrier layers. The growth temperature and pressure were 1000 ^{o}C and 30 mbar. Figure 2.1 shows the temperature profile of the complete growth process.

In order to evaluate the structural characteristics of the MQWs:Er, we have performed X-ray θ–2θ diffraction measurements for these samples. The measurements provide information about the interfaces between the wells and barriers. The measurements have been done for a set of MQWs:Er samples with a fixed barrier thickness, L_B = 10 nm, and varying quantum well width, L_{QW}, (0.6, 1.0, 1.5, 2.8, 4.0, 5.3, 6.6 nm).[68] Here we present the data with the same quantum well thickness of 1.5 nm, and different AlN barrier widths (1, 3, 6, 8 nm).

The peaks at 2θ = 36.02^{o} in Fig. 2.2 come from the (0002) plane of the underlying undoped AlN and the satellite peaks originate from the Er doped GaN/AlN MQWs. The diffraction peaks having many well-defined satellite peaks in the X-ray diffraction spectra of MQWs indicate that the interfaces between wells and barriers are abrupt.[69] As seen in Fig. 2.2, Er doped GaN/AlN MQWs with different barrier thicknesses exhibited several intense satellite peaks, confirming that the interfaces between quantum wells and barriers are smooth. The MQWs:Er samples with barrier widths thicker than 1 nm show large numbers of intense satellite peaks, indicating that these samples possess high interfacial qualities.[68, 69, 70]

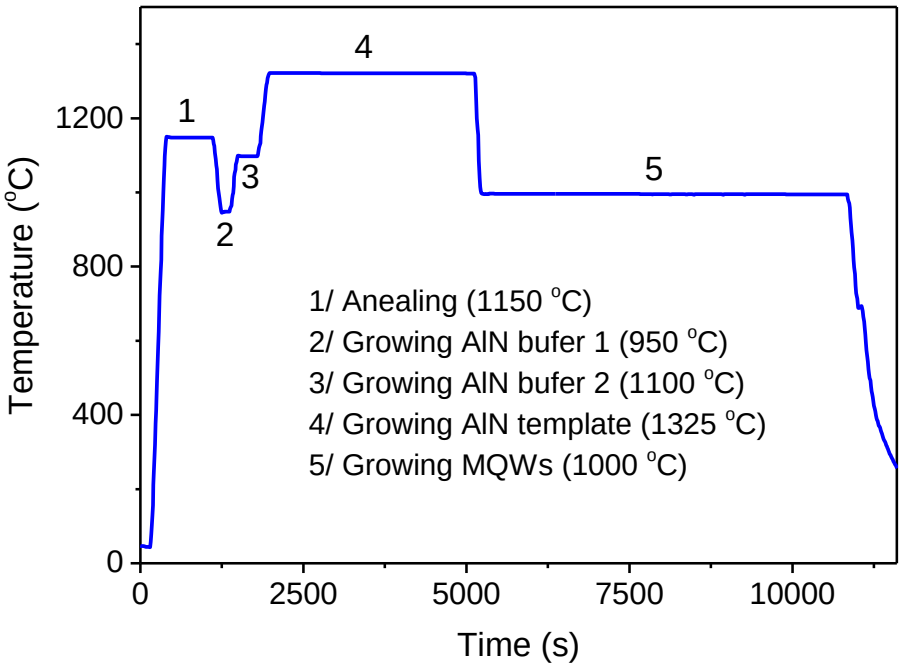

Figure 2.1: *The growth temperature sequence of MQWs:Er samples.*[20]

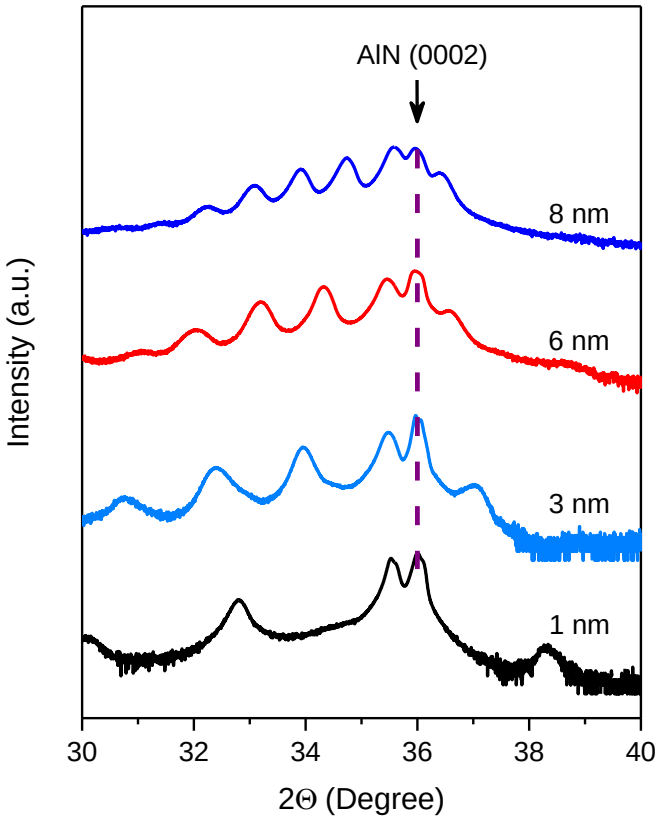

Figure 2.2: *X-ray θ-2θ diffraction measurement of Er doped GaN/AlN MQWs with different AlN barrier thicknesses (1, 3, 6 and 8 nm) and fixed GaN well width of 1.5 nm.*[20]

2.1.2 MOCVD Growth of Er doped GaN epilayer

The Er-doped GaN materials were grown on a (0001) c-plane sapphire substrate in a horizontal reactor MOCVD system.[18, 71, 72] Prior to the growth of the GaN:Er epilayer, a 20-nm low-temperature GaN layer as a buffer, and a 1.2-μm undoped GaN epilayer were first grown on the sapphire substrate. This was then followed by the growth of the GaN:Er epilayer of 0.5 μm thickness. The temperature for the growth process of Er-doped GaN epilayers was set at 1040 °C. An optimum Er concentration was about ~2 × 10^{20} cm^{-3} to ~ 10^{21} cm^{-3} to obtain the strongest photoluminescence (PL) intensity. A high degree of crystallinity without a second phase formation in the GaN:Er layers has been confirmed by X-ray diffraction measurements.[73] The band gap energy of GaN:Er epilayers is about 3.4 eV at room temperature. A detailed description of the growth process and epilayer structure has been reported previously[18, 71, 72, 74, 75].

2.2 Photoluminescence

Photoluminescence, referred to as PL, is the spontaneous emission of light from matter after the absorption of photons with sufficient energy. When such photons come onto the samples, the photo-excitation process can occur. In this process, photons excite the electrons from the ground state to the excited states. After that, these electrons will release energy or radiate photons to return to the lower energy levels. It is a non-contact, nondestructive method. The PL spectrum, the dependence of PL intensity as a function of excited power of light and of temperature on the samples, give important information to investigate impurity levels, transition energy, and radiative and non-radiative recombination mechanisms.

The PL spectra were conducted using a high-resolution Horiba iHR550 spectroscopy with a 900 grooves/mm grating blazed at 1500 nm and detected by the high sensitivity liquid nitrogen InGaAs DSS-IGA detector. The resolution of the PL spectrum is 0.1 nm. Power-dependent and temperature-dependent PL measurements were carried out in a closed-cycle optical Janis cryostat providing a temperature from 10 K to 300 K. The excitation modulation was achieved by a pinhole and chopping the laser beam at 41 Hz. The resonant excitation PL spectra were obtained using a tunable wavelength Ti:sapphire laser at 836 nm (1.483 eV) with a repetition rate of 80 MHz to excite the electrons from ground state $^4I_{9/2}$ to the excited state $^4F_{5/2}$. The band-to-band excitation PL spectra used an Argon laser operating at 351.1 nm (3.531 eV) for GaN:Er samples. The lifetime measurements were conducted using a Tektronix MD04104C mixed domain oscilloscope in combination with InGaAs detector.

2.3 Optical gain determination

A variable stripe length (VSL) technique was proposed by Kerry L. Shaklee and coworkers from Bell Telephone Laboratories in 1971. A specimen of semiconductor was excited by a laser beam focused, using a cylindrical lens, into a narrow stripe. The length of this pumped “line” is varied. Light-out is measured as a function of the stripe length l. This experimental technique, called the “variable stripe length (VSL) method”, rapidly became popular and contributed significantly to the development of a family of semiconductor lasing compounds. Shaklee et al. demonstrated high optical gain in GaN. The VSL method is a very popular tool to determine the optical gain in thin film active devices. The advantage of this method is that samples suitable for measurements can be transparent, opaque, solid or even liquid and need not have been prepared in

special shapes. There are two experiments including edge-emission measurement and gain measurement.

2.3.1 Edge-emission measurements

The pump laser was magnified and then focused onto the top surface of samples using a cylindrical lens with f = 7.5 cm. Only the central part of the laterally unfocused laser spot was used to excite the sample so that the pump fluence was uniform across the entire excited area, as shown Fig. 2.3. The excitation area was measured to be a long stripe of 8.0 ± 0.3 μm width exciting the entire sample length of 1000 ± 0.5 μm. We used a two-dimensional linear stage to scan our UV photodetector at the focal position of the laser to verify that within experimental conditions the laser pump fluence on the sample surface was constant and independent of the length. No influence of diffraction effects on the uniformity of the pump laser was detected. An aperture was used to ensure that none of the light which may have passed out of the excited volume before reaching the edge of the sample, was detected. The edge-emission was collected using a set of two lenses f = 10 cm and f = 24 cm with a diameter of 5 cm and focused onto the entrance slit of the high resolution spectrometer through a long-pass filter blocking all background light with wavelength shorter than 950 nm. All the edge-emission measurements were done at room-temperature. The photon fluence on the sample was varied from 0.05 to 500 mJ cm^{-2}.

2.3.2 Gain measurements

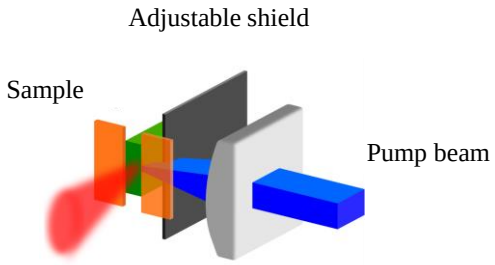

Figure 2.3: *Experiment set-up of a variable stripe length (VSL) technique.*

Net optical gain of the sample was measured using the variable excitation length method. In the same edge-emission measurement configuration, a mobile blade was mounted on an ultra-precise linear translation stage (relative accuracy of 80 nm). The edge-emission was collected and focused onto the entrance slit of the spectrometer as described. The measured gain coefficients

show a fluctuation of within 5% for different distances between the sample's top surface and the mobile blade, suggesting that diffraction effects can be safely disregarded.

2.4 Fabrication of the graphene photodetectors

The graphene-based photodetectors were fabricated in the Virginia Tech cleanroom. Fabrication processes are discussed below.

2.4.1 Making metal contacts

Metal contacts have been fabricated using the photolithography process. The negative photoresist, AZ nLOF 2020, was spin-coated on the Si/SiO_2 wafer at 500 rpm in 10 s, and then 3000 rpm in 30 s. The thickness of photoresist was 2 µm. The wafer was soft-baked on a hot-plate at 110 ^oC for 1.5 min. The wafer was exposed by using a Suss Mask Aligner MA6 combined with a photomask. Some photomasks are shown in Fig. 2.4. The parameters for photolithography were used for this step including mode of hard-contact, gap of 110 µm, wait time of 4 s, exposed time of 4 s, and g-line of 435 nm (CH2). The exposed does of 75 mJ/cm^2 was employed. Next, the wafer was hard-baked on the hot-plate at 110 ^oC for 2 min. The development process requires 1.5 min, after which the wafer was cleaned in deionized (DI) water immediately. The AZ 300 MIF developer is recommended for the AZ nLOF 2020 photoresist.

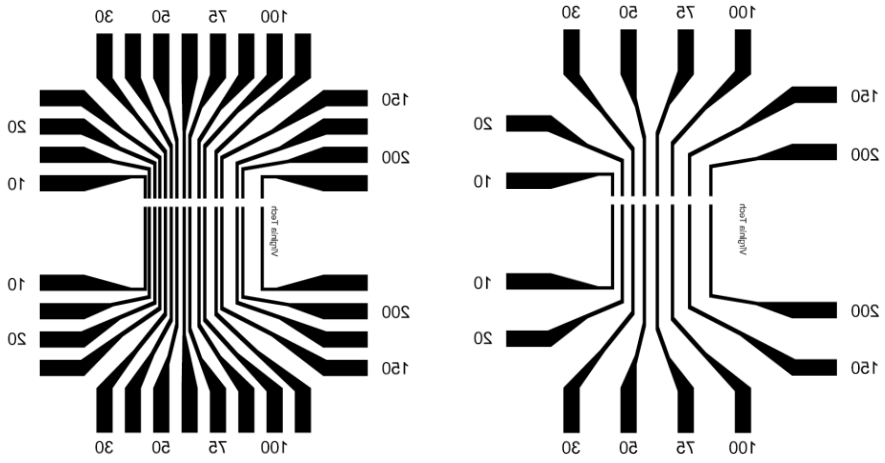

Figure 2.4: *Example of the photomasks of metal contacts for fabricating the graphene-based photodetectors.*

The metal contacts were deposited on the wafer after the development process. We used e-beam evaporation (Kurt J. Lesker PRO Line PVD 250). In comparison to the sputtering method, the side walls of the undercut resist profile are not coated during depositing the metal film, thereby facilitating lift-off. Metal films of 10-nm Cr and 80-nm Au were deposited. The deposition rate of the film was controlled to make sure that the temperature on the substrate was below 35 ^{o}C. Typically, the deposition speed of the Cr layer and the Au layer is 0.5 Å /s and 1 Å /s, respectively. The wafer was then dipped in acetone after 12 hours to lift-off the photoresist. The wafer was cleaned before transferring graphene as described in the next section. The steps of making metal contacts are presented in Fig. 2.5.

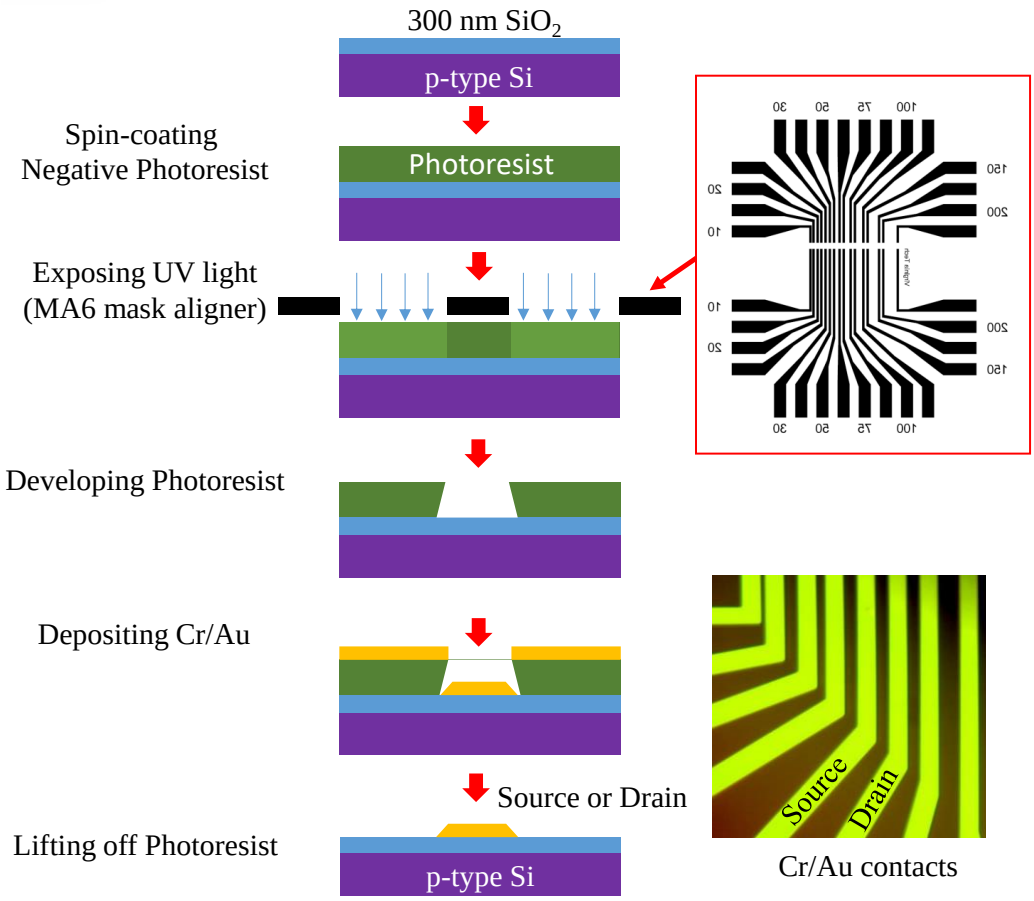

Figure 2.5: *Illustration of the steps of making metal contacts using negative photoresist*.

2.4.2 Cleaning the wafer

After fabricating the metal contacts on the 6-inch Si/SiO_2 wafer, the wafer was cut into chips with the size of 1x1 cm^2 with metal contacts. These chips needed to be cleaned. This is an important

step to eliminate the residual of photoresist on Si/SiO_2 chips. First, the chips were sonicated in acetone for 20 min, then in isopropyl alcohol (IPA) for 20 min. They were then immersed in deionized water for 5 min before drying with nitrogen gas. Finally, oxygen-plasma treatment was employed to etch the rest of photoresist residual using a Samco RIE-10 NR system, under the power of 30 W, a gas flow rate of 10 sccm oxygen, and a pressure of 30 mTorr.

2.4.3 Transferring graphene

Monolayer graphene on copper foil from Graphenea Inc. was transferred onto Si/SiO_2 chips with metal contacts. In order to transfer graphene, the Poly(methyl methacrylate) (PMMA, MicroChem 450 A4 – (4.5% in anisole) - 450,000 molecular weight) solution was used. PMMA was spin-coated on the graphene film at 500 rpm for 5 s, then at 2500 rpm for 45 s. PMMA/Graphene/Cu film was dried in the air for 30 min, and then in a vacuum chamber for 1 hour at the pressure of 30 mTorr. The sample was then annealed at 50 ^oC for 2 min. The graphene on the other side of Cu foil without PMMA covering was etched by oxygen plasma under the power of 30 W, a gas flow rate of 10 sccm oxygen gas follow and a pressure of 30 mTorr for 1 min.

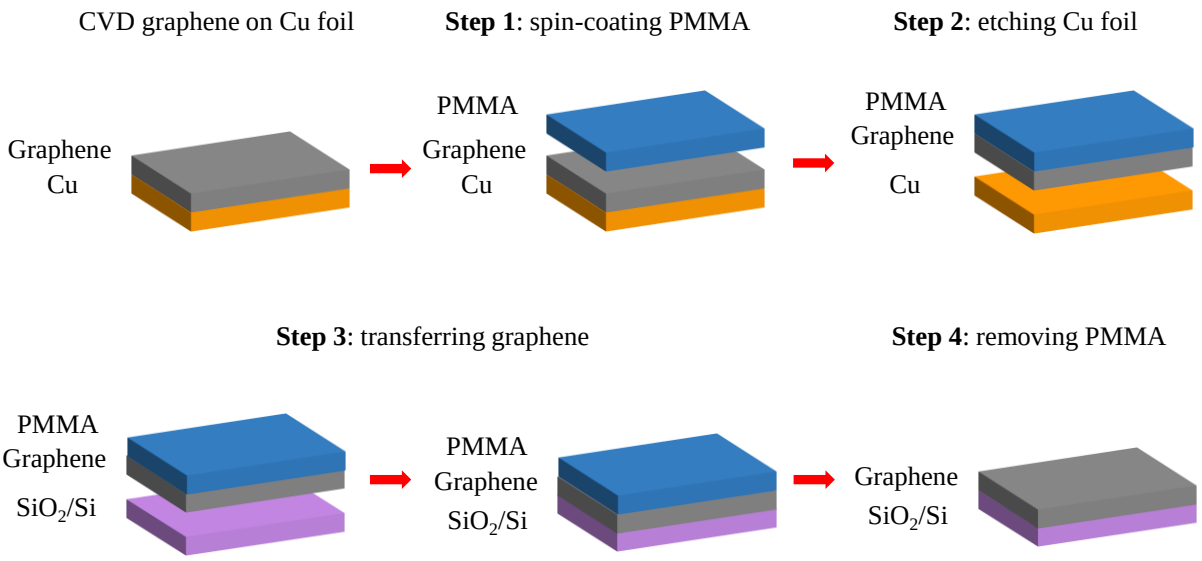

Figure 2.6: *Illustration of steps of transferring graphene on Si/SiO_2 chip.*

To remove the Cu foil, the sample was put in 0.1 M ammonium persulfate [$(NH_4)_2S_2O_8$, Sigma−Aldrich, ≥98%] aqueous solution for 1.5 h at 30 ^oC. The graphene/PMMA was rinsed two

times in DI water for 5 min. The cleaned Si/SiO_2 chip was scooped out of the graphene film. This sample was dried in air for about 4 h, then placed in vacuum for 12 h. Figure 2.6 presents the transferring of graphene from copper foil to Si/SiO_2 chip.

2.4.4 Removing PMMA

The PMMA/Graphene on the Si/SiO_2 chip was baked on a hot plate at 85 ^oC for 5 min, then 140 ^oC for 15 min to promote a good adhesion. Then, it was placed in warm acetone at 55 ^oC for 1 h, followed by cleaning with IPA for 30 min and drying.

2.4.5 Patterning the graphene

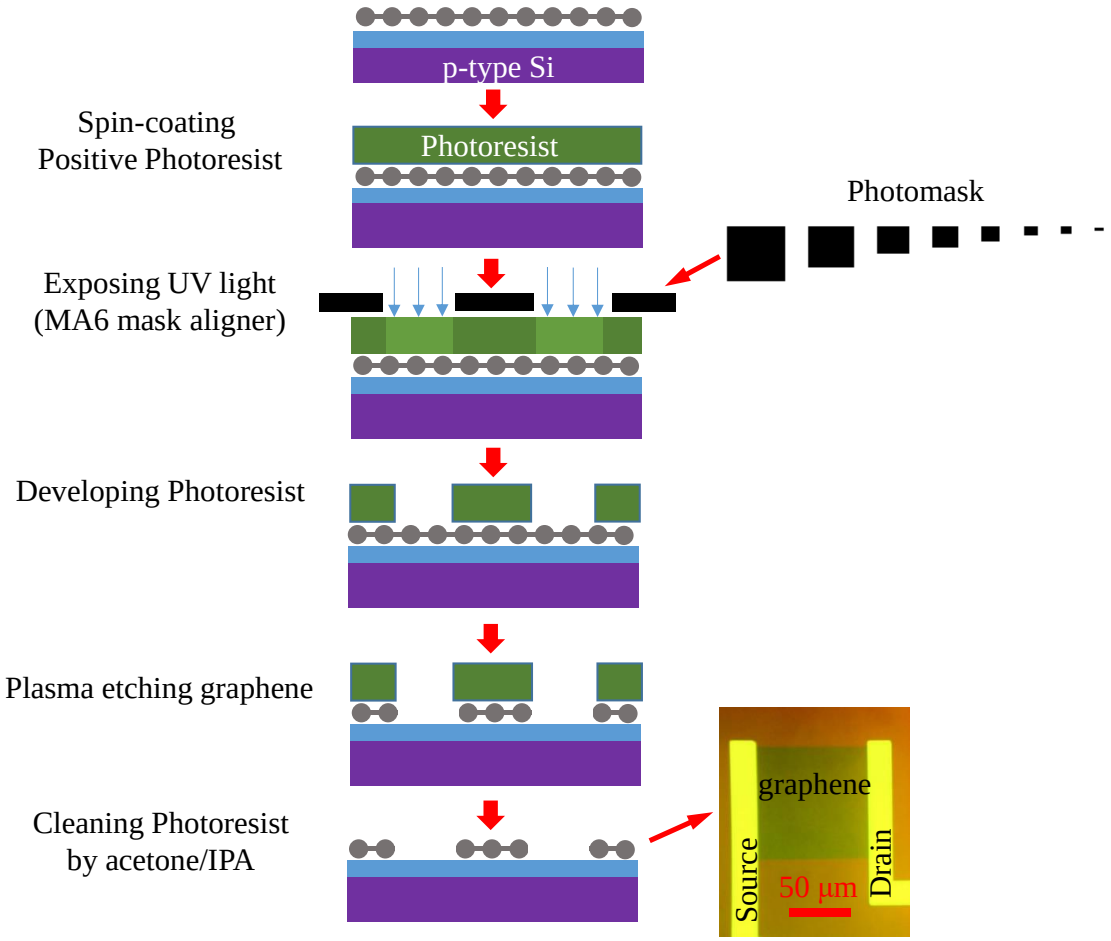

Figure 2.7: *Illustration of the steps of patterning graphene on the Si/SiO_2 chip using positive photoresist and oxygen plasma etching.*

Positive photoresist Shipley 1813 was spin-coated on the chip with graphene at 500 rpm for 5 seconds, then 3000 rpm for 30 s. It was then baked on a hotplate at 100 ^oC for 60 s. Graphene

patterns were fabricated by using the Suss Mask Aligner MA6. The parameters for this photolithography step were soft contact, gap of 30 μm, waiting time of 4 s for UV lamp to stablize, exposed time of 8 s and g-line of 435 nm (CH2). The exposure time is the important parameter. Shipley needs an exposure dose of 115 mJ/cm^2 for the photoresist film of 2-μm thickness. The exposed time can be calculated by dividing the exposed dose to power density of the Suss Mask Aligner MA6 lamp. Chips were developed in the MIF 319 developer to produce patterns of graphene on photoresist layer for 60 s, then immediately cleaned in DI water before drying by nitrogen gas. Oxygen plasma was employed to etch graphene by using the Samco RIE-10 NR system under the power of 30 W, the oxygen gas flow rate of 10 sccm and pressure of 30 mTorr. The etching time depends on the detail of each process. Typically, it could vary from 7 to 45 s. The graphene patterns will be obtained after cleaning in acetone for less than 10 minutes and IPA for 5 min, and then drying under nitrogen gas. The patterning process is demonstrated in Fig. 2.7.

2.4.6 Growing the absorber layers

To evaporate light absorbing layers on graphene, The PVD 250 has been used for several materials including Si, Ge, Ta_2O_5, Ti_2O_3 and Al_2O_3. The deposition rate is 0.1 Å s^{-1} under the pressure of 4×10^{-6} Torr. The thickness of absorber layer is typically 5 nm.

2.4.7 Characterization of graphene photodetectors

The electrical characteristics were examined by two Keithley 2400 source-meter units. The first unit, a Keithley 2400, is used to control the back-gate voltage, V_{BG}. The second unit, a Keithley 2450, is used to set a constant voltage between the source and the drain, V_{SD}, and to measure the drain current, I_{DS}. A schematic diagram is shown in Figure 2.8. Several light sources have been employed in the experiments. In the UV-to-NIR region, a diode-pumped laser operating at 532 nm (Coherent Verdi-V2), a UV-VIS broadband light source (Edmund, #87-300), and a fiber laser lasing at 1.53 μm have been used. For MIR experiments, a CO_2 laser operating at 10.6 μm and quantum cascade lasers at 4.55 μm have been used. A half-wave plate and a polarizing beam-splitter are used to control laser beam power. To control the power of incoherent light sources neutral density filters are employed. A diaphragm with a 5-mm diameter was used to form the light source, with a uniform intensity distribution. The light sources covered the entire graphene FET photodetector. By knowing the active size as well as illumination power, the power of the light

incident upon the photodetectors could be estimated. The optical set-up is presented as the figure 2.9.

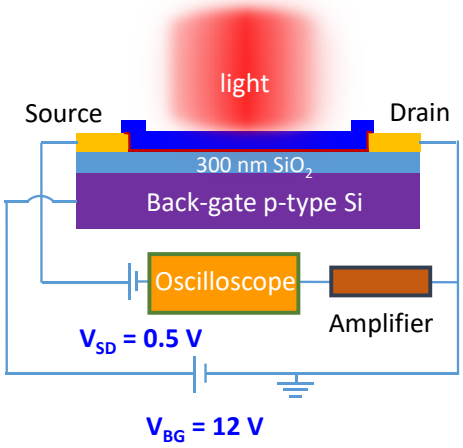

Figure 2.8: *A schematic for electrical measurements. A voltage of 0.5 V was applied between Source and Drain contacts (VSD). The back-gate voltage (VBG) was varied from -30 to 30 V. The photocurrent can be collected with a lock-in amplifier, an oscilloscope, or Keithley 2450.*

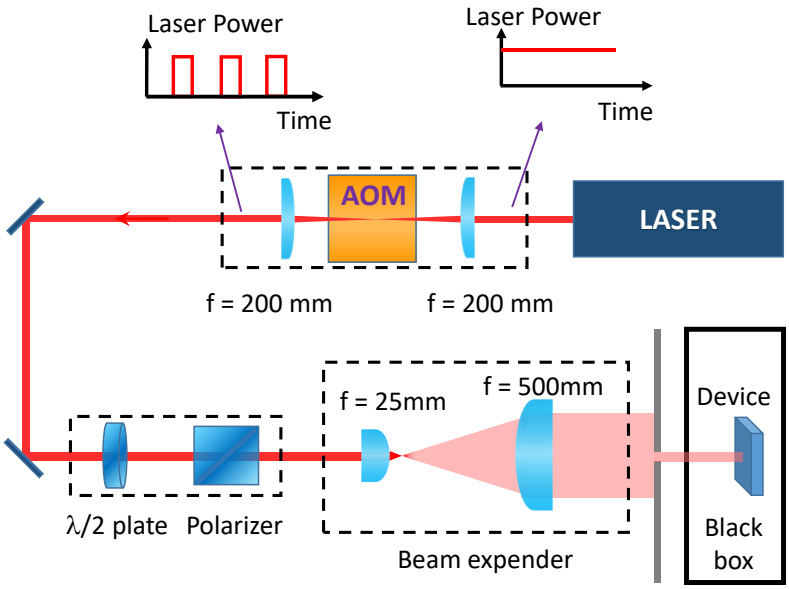

Figure 2.9: *Optical setup for ultra-fast photo-response measurements. The system consists of an Acousto-optic modulator (AOM), a half-wave plate, a polarizer beam splitter, and lenses. The sample is put in a black box to prevent random light from ambient.*

Chapter 3

Photoluminescence quantum efficiency of Er optical centers in GaN epilayers

This chapter was adapted with only minor changes from the manuscript:
V. X. Ho, et al. Photoluminescence quantum efficiency of Er optical centers in GaN epilayers. Scientific Reports, 7, 39997 (2017).

We report the quantum efficiency of photoluminescence processes of Er optical centers as well as the thermal quenching mechanism in GaN epilayers prepared by metal-organic chemical vapor deposition. High resolution infrared spectroscopy and temperature dependence measurements of photoluminescence intensity from Er ions in GaN under resonant excitation excitations were performed. Data provide a picture of the thermal quenching processes and activation energy levels. By comparing the photoluminescence from Er ions in the epilayer with a reference sample of Er-doped SiO_2, we find that the fraction of Er ions that emit photons at 1.54 μm upon a resonant optical excitation is approximately 68%. This result presents a significant step in the realization of GaN:Er epilayers as an optical gain medium at 1.54 μm.

3.1 Introduction

The incorporation of rare earth elements into wide bandgap semiconductors is of significant interest for optoelectronic device applications, because of their temperature independent, atomic-like and stable emission together with the possibility of optical or electrical excitation[76, 77]. Much of the research has focused on the element Er with the emission from the first excited state ($^4I_{13/2}$) to the ground state ($^4I_{15/2}$) at 1.54 μm, the minimum loss window of silica fibers for optical communications and lying in the eye-safe wavelength region.[5, 16, 78, 79, 80] GaN with the direct bandgap semiconductor appears to be an excellent host material for Er ions, not only due to their structural and thermal stability[72, 81, 82] but also to the recent advancements in growth techniques of high-quality crystals of both n- and p-type.[77] While light emitting diodes based on GaN:Er have been demonstrated[75], the realization of GaN:Er materials for optical amplification is still under investigation. For this reason, it is necessary to determine important factors which influence the optical performance of Er embedded in GaN. The information would provide us with the direction to optimize the optical properties of GaN:Er material.

Several important factors that determine the optical gain in GaN:Er need to be unraveled including the fraction of Er ions that contribute to light emission, and the number of optical centers as well as the energy transfer between the GaN host and Er ions. Previous work has revealed that a number of Er optical centers as well as a variety of energy transfer routes take place in GaN.[83, 84] The existence of various Er optical centers depends on preparation methods, such as ion implantation,[85, 86] metal-organic chemical vapor deposition (MOCVD)[18] and molecular beam epitaxy (MBE),[87] as well as growth and annealing conditions.[85] A single type of Er optical center was reported in GaN epilayers grown by MOCVD method.[88, 89] The absorption and emission studies together with the crystal field calculation provided an understanding of energy transfer mechanism to Er ions and the Er related luminescence process.[90] Non-radiative recombination channels were also investigated to understand photoluminescence (PL) quenching.[91] The Er-related trap centers with energy levels in the GaN bandgap act not only as active centers for bound excitons transferring their energy to 4f electrons of Er^{3+} ions, but also as PL quenching centers.[72, 92, 93] These previous studies provided important insights for the improvement of Er emission in material engineering towards optimizing the energy transfer between the GaN host and Er ions. In our previous report, isolated Er and defect-related Er optical centers have been identified through high-resolution infrared PL spectroscopy.[74] Understanding the optical excitation mechanisms,

optical activity of Er^{3+} infrared luminescence and quenching channels is essential to enhance the emission efficiency of GaN:Er.

We present in this work a careful analysis of Er luminescence in GaN epilayers by comparing the PL intensity from our GaN:Er epilayers to a well-characterized standard reference sample of SiO_2:Er. The SiO_2:Er system has been used as an optical gain medium for solid-state lasers at 1.54 μm.[16, 94] The Er ions embedded in the defect free, insulating host matrix, SiO_2 reference sample, has an internal quantum efficiency (IQE) over 98%. Since basically all the Er ions in the SiO_2 matrix participate in photon emission, the reference sample can be employed as a benchmark to determine the optical activity of Er in other matrices. A low thermal quenching of 20% from 10 K to room temperature from the isolated Er optical centers in GaN epilayer at the 1.54 μm emission has been demonstrated. Employing a high-resolution spectroscopy and temperature dependent measurements of PL intensity under resonant excitation provides an estimate of the quantum efficiency of PL process of Er optical centers as well as the thermal quenching mechanisms in GaN epilayers grown using the MOCVD technique.

3.2 Experimental details

The high-resolution PL spectra were conducted using a Horiba iHR550 spectrometer equipped with a 900 grooves/mm grating blazed at 1500 nm and detected by a high sensitivity liquid nitrogen InGaAs DSS-IGA detector. The resolution of PL spectrum is 0.05 nm. The PL experiments were carried out in a variable temperature closed-cycle optical cryostat (Janis) providing a temperature range from 10 K to 300 K. Both resonant excitation and the non-resonant excitation were employed to investigate the optical properties of Er in GaN epilayers.[74] The resonant excitation PL spectra from $^4I_{15/2} \rightarrow {}^4I_{9/2}$ of Er^{3+} in GaN were obtained using a tunable wavelength Ti:Sapphire laser around 809 nm (1.533 eV) with a repetition rate of 80 MHz.[74] A detail description of the growth process and Er-doped GaN epilayer structure has been reported previously[18, 71, 72, 74, 75] as well as in Chapter 2.

3.3 Results and discussion

We will discuss the emission mechanism of epilayer GaN:Er sample as well as estimate the quantum efficiency of PL process of Er-related optically active centers by using a high-resolution spectroscopy and temperature dependent measurements of PL intensity under resonant excitation .

3.3.1 Resonant and non-resonant excitation methods

The influence of Er^{3+} site on the PL emission can be determined from optical excitation mechanisms. We have reported direct evidence of two mechanisms responsible for the excitation of optically active Er^{3+} ions in GaN epilayers grown by MOCVD in our previous work.[74] Under resonance excitation via the higher-lying inner 4f shell transitions and non-resonant (band-to-band) excitation of the GaN host, the high resolution PL spectra at 10 K reveal an existence of two types of Er optical centers including the isolated and the defect-related Er optical centers in GaN epilayers.[74] For the first case, the isolated Er optical centers occupying Ga substitutional sites were observed under both the resonant ($^4I_{15/2} \rightarrow {}^4I_{9/2}$) excitation and the band-to-band excitation. Er ions in substitutional sites are considered as an isoelectronic impurity center.[95] The center, with no net charge in the local bonding region, can be excited by resonant and band-to-band excitation. Under the band-to-band excitation, a hole or an electron can be localized at the isolated center by a local core potential; subsequently, the secondary particle can be captured by the Coulomb field of the first particle. The recombination of the two particles will transfer their energy to the Er ion. For the second case, the defect-related Er optical center can only be observed through the band-to-band excitation of the host involving a trapped (bound) exciton. The observation has been confirmed with a photoluminescence excitation measurement.[74] The excitation mechanism for the defect-related Er centers is believed to be related to intrinsic defects, impurities or defect-impurity complexes near the Er optical center. These defects capture excitons and subsequently transfer non-radiatively their energy to nearby Er ions. The efficiency of this process is high, but the requirement of bound excitons for excitation opens up non-radiative recombination channels for the luminescence process. At room temperature, we do not observe PL emission from the defect-related Er optical centers. For optoelectronic applications of the GaN:Er epilayers, this work focuses on the optical characterization of the isolated Er optical centers under the resonant excitation.

3.3.2 Photoluminescence spectra

To determine the crystal field splitting of the first excited state ($^4I_{13/2}$) of the isolated Er optical centers, the high-resolution spectra as well as the temperature dependence of the PL spectra, have been investigated under resonant excitation (Fig. 1). At low temperatures, the spectrum of the isolated Er optical center consists of a set of narrow and intense PL lines (L center): L_1, L_2, L_3, L_4,

L_5, L_6 and L_7 at energies of 809.88, 809.28, 807.80, 806.85, 806.32, 803.62, 802.91 meV, respectively. At higher temperatures, other PL lines, labeled hotlines $L^h_{1,2}$, L^h_4, L^h_5, L^h_6, appear at ~ 821.5, 819.6, 819.2 and 816.5 meV, respectively (Fig. 1). The PL intensity of PL lines L_3, L_7, are weak at low temperature and we cannot resolve the PL of hotlines L^h_3, L^h_7 at higher temperature. These hotlines are displaced by about 12.6 meV. At high temperature, the intensities of the hotlines rapidly increase with increasing temperature while the intensities of the main PL lines decrease. We note that due to the temperature broadening at high temperature the PL from L_1, L_2 lines merge into one PL line, thus we cannot resolve the PL hotlines L^h_1, L^h_2.

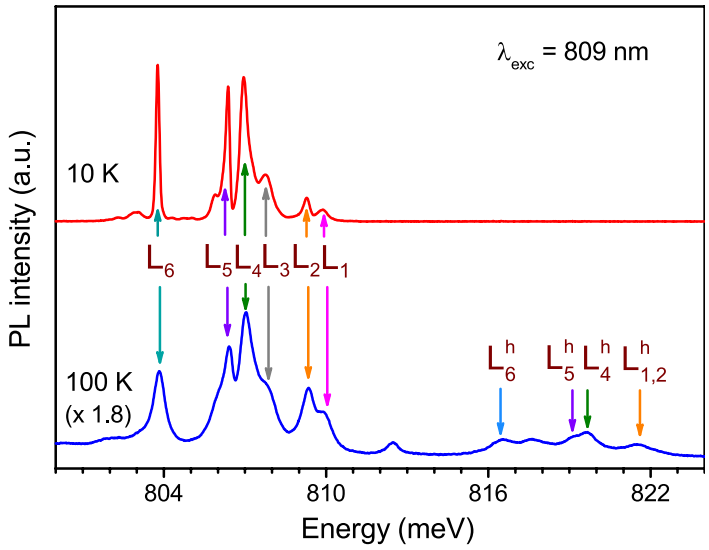

Figure 3.1: *The PL spectra at 10 K and 100 K of the GaN:Er epilayer at 1.54 µm within the* $^4I_{13/2} \rightarrow {}^4I_{15/2}$ *transition under the resonant excitation (*$^4I_{15/2} \rightarrow {}^4I_{9/2}$*) excitation using a Ti:sapphire laser (*λ_{exc} *= 809 nm). At low temperature, the spectrum of the isolated Er optical center consists of a set of narrow and intense PL lines (*L_1 *to* L_7*). At higher temperatures, hotlines,* $L^h_{1,2}$, L^h_4, L^h_5, L^h_6*, appear and are displaced by about 12.6 meV. The intensities of hotlines rapidly increase with increasing temperature while the intensities of the main PL lines decrease.*

3.3.3 Non-radiative transfer energy process

In order to determine the non-radiative transfer energy between Er^{3+} ions and GaN host, we have measured the integrated PL intensity at the 1.54 µm emission as a function of temperature (Fig. 3.2). The integrated PL intensity measurements for the whole 1.54 µm band under the

resonant excitation (λ = 809 nm) indicate a low thermal quenching of 20% from 10 K to room temperature from Er^{3+} ions in our GaN:Er epilayer (Fig. 3.2, inset).

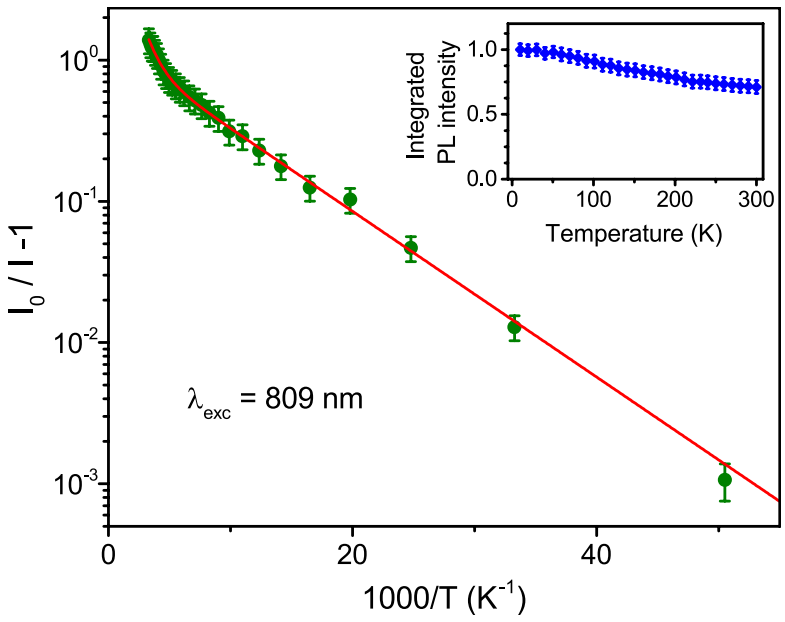

Figure 3.2: *The temperature dependence of PL intensity measured under the resonant excitation (λ_{exc} = 809 nm) indicates a low thermal quenching from Er^{3+} ions in our GaN:Er epilayer. The plot illustrates the (I_0/I-1) vs. T^{-1} behavior that was used to guide the Arrhenius fitting in which I is the integrated PL intensity at the temperature of T, I_0 is the integrated PL intensity at 10 K. Activation energies of 13 and 118 meV have been determined. (inset) The integrated PL intensity measurements at 1.54 µm band show a thermal quenching of 20% from 10 K to room temperature from isolated Er optical centers.*

These measurements determine the non-radiative recombination channels causing the thermal quenching of PL emission from isolated Er optical centers. In this model, the observed PL intensity for main PL lines of isolated centers should follow the Arrhenius equation:

$$I(T) = \frac{I_0}{1 + C_1 \exp\left(-\frac{E_{A1}}{k_B T}\right) + C_2 \exp\left(-\frac{E_{A2}}{k_B T}\right)} \qquad (1)$$

where I(T) is the integrated PL intensity at the temperature of T, I_0 is the integrated PL intensity at 10 K, E_{A1} and E_{A2} are the activation energies of the thermal quenching processes, C_1 and C_2 are fitting constants related to the density of non-radiative recombination centers in the sample, and k_B is Boltzmann's constant.

As shown in the Fig. 3.2, the solid line presents the best fit to the integrated PL intensity using Eq.1. The activation energy values derived from the fitting are E_{A1} = 13 and E_{A2} = 118 meV. Obviously, the replications of PL lines at higher temperature originate from the transition of the second-lying crystal field split level of the first ($^4I_{13/2}$) excited state to the sublevels of ($^4I_{15/2}$) ground state. When temperature increases, electrons from the lowest level of the first excited state gain energy and populate at the second-lying crystal field split level. Thus, the intensity of the main PL lines decreases, and the intensity of hotlines increases with temperature. These hot lines are displaced by 12.6 meV, which is nearly equal to the activation energy of 13 meV.

3.3.4 Physical mechanism of non-radiative transfer energy process

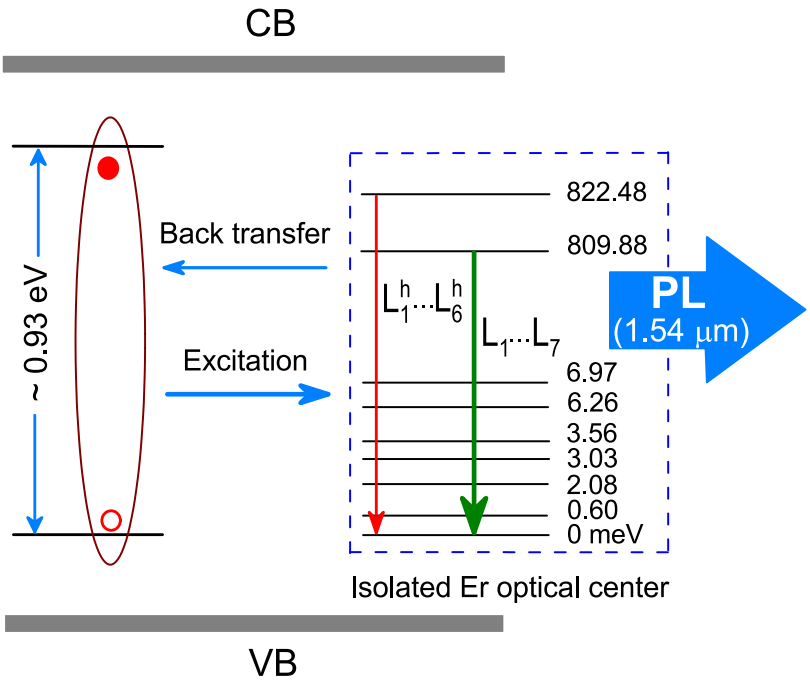

Figure 3.3: *The Stark sub-energy level diagram of the excited and ground states of the isolated Er optical center and a deep defect level which are responsible for the luminescence thermal quenching process of* Er^{3+} *ions.*

An energy level diagram for the luminescence of isolated Er optical centers is illustrated in Fig. 3.3. A local density functional study[93] of the Er doped GaN system showed that Er-related defect complexes with different local environments have different electronic properties for Er optical centers. For the 1.54 μm emission, deep defect levels associated with Er optical centers are expected to act as carrier traps. A hole or an electron can be localized at the deep level by a local

core potential; subsequently, the secondary particle can be captured by the Coulomb field of the first particle. The recombination of the two particles will transfer their energy to the Er ion. The reverse of this process, an energy ‘‘back transfer,’’ is believed to be responsible for the decrease of PL intensity in these systems at elevated temperatures. Following the proposed excitation model, the energy back-transfer process in the isolated Er optical centers involves the de-excitation of excited Er^{3+} by transferring their energy to the deep defect level of ~ 0.93 eV (Fig. 3.3). At the deep level, the energy deficit, in this particular case ~120 meV, is compensated by the annihilation of lattice phonons.[91, 96, 97, 98]. Such a deep defect level has recently been predicted using the first-principles hybrid density functional study for Er-related defect complexes in GaN[99]. By optimizing the synthesis conditions including Er concentration, growth temperature, Er precursor vapor pressure, V/III flux ratio, we have significantly reduced the concentration of defect centers during the MOCVD growth to obtain strong PL intensity at room temperature.

3.3.5 Determination of Er^{3+} optical active centers in GaN:Er epilayer

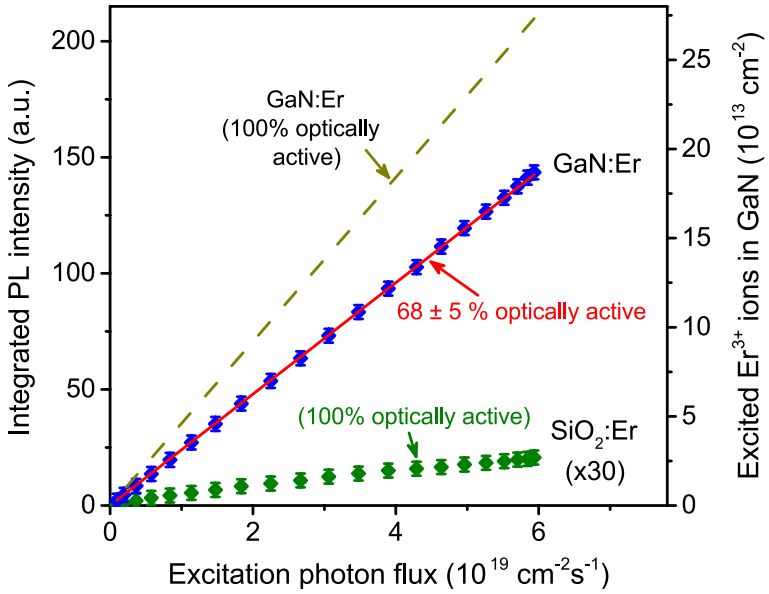

Figure 3.4: *Comparison of the integrated PL intensity of Er^{3+} ions in GaN epilayer with the reference SiO_2:Er sample under the resonant ($^4I_{15/2} \rightarrow {}^4I_{9/2}$) excitation indicates that a fraction of ~ 68% of Er^{3+} ions in GaN sample are optically active.*

The percentage of Er dopants that emit photons upon excitation is a crucially important parameter for the potential application of Er-doped semiconductors. In particular, it determines the PL emission efficiency at 1.54 μm of GaN:Er materials as well as the population inversion. An

estimate of the number of emitting Er optical centers can be made by comparing the PL intensity of the GaN:Er epilayer grown by MOCVD technique with that of the SiO_2:Er reference sample with a similar shape and under the same experimental conditions. The experiment at room temperature has been performed under the resonant excitation ${}^4I_{15/2} \rightarrow {}^4I_{9/2}$ transition using the Ti:sapphire laser at 809 nm. The time-integrated PL intensity of these samples has been collected as a function of applied photon fluxes (Fig. 3.4).

The instantaneous PL intensities of both samples were proportional to N^*_{Er}/τ_{rad}, where N^*_{Er} and τ_{rad} are the density of excited Er^{3+} ions and their radiative lifetimes, respectively. Since the PL signal is integrated over time, the result of the experiment will be proportional to $N^*_{Er} \times \tau/\tau_{rad}$, where τ is the effective PL lifetime. The ratio of effective and radiative lifetime is the internal quantum efficiency (IQE), $IQE = \tau/\tau_{rad}$, of the optical center. To obtain the number of photons coming out of the sample, the external quantum efficiency (EQE) is determined by the refractive index of the material for a specific wavelength, i.e., $EQE = \eta \times IQE$, where η is the extraction efficiency. In this calculation we ignore the photon reabsorption; therefore, the ratio of the number of photons emitted from the two investigated samples is given by

$$\frac{I_{GaN:Er}}{I_{SiO_2:Er}} = \frac{\eta_{GaN}}{\eta_{SiO_2}} \frac{N^*_{Er(GaN)}}{N^*_{Er(SiO_2)}} \frac{\left(\tau_{eff}^{Er(GaN)}/\tau_{rad}^{Er(GaN)}\right)}{\left(\tau_{eff}^{Er(SiO_2)}/\tau_{rad}^{Er(SiO_2)}\right)} \qquad (2)$$

The ratio of the extraction efficiencies can be calculated from the refractive indexes of GaN and SiO_2 materials.

$$\frac{\eta_{GaN}}{\eta_{SiO_2}} = \frac{n_{air}^2/(4n_{GaN}^2)}{n_{air}^2/(4n_{SiO_2}^2)} = 0.389 \qquad (3)$$

where n_{GaN} and n_{SiO2} are the refractive indexes of 2.318 and 1.445 at 1.54 μm for GaN and SiO_2, respectively.

Under the resonant excitation, the decay dynamics of all PL lines of the isolated Er optical centers appear as a single exponential with a decay time constant of 3.3 ± 0.3 ms.[74] The value is similar to those of previous reports on the Er in GaN.[83, 100, 101] The decay dynamics is effectively independent of temperature over the entire range from 10 K to room temperature. Thus, the radiative lifetime is 3.3 ms, and the internal quantum efficiency of the isolated Er optical center in GaN equals to 1, $IQE_{Er(GaN)} = \tau_{eff}^{Er(GaN)}/\tau_{rad}^{Er(GaN)} = 1$. For the SiO_2:Er standard sample, the Er embedded in the defect free, insulating host matrix, SiO_2, has an internal quantum efficiency (IQE) over 98%. Thus, we obtain $IQE_{Er(GaN)} = \tau_{eff}^{Er(SiO_2)}/\tau_{rad}^{Er(SiO_2)} = 1$.

The well-characterized SiO_2:Er sample can be used to attribute the measured PL intensity to a particular density of excited Er^{3+} ions. The number of excited Er^{3+} ions in the SiO_2 reference sample can be calculated through excitation photon flux when we assume that all Er^{3+} ions are equivalent, and they all contribute to the PL process. As has been discussed previously,[74, 79, 102] under steady-state conditions, the photon flux dependence of Er^{3+} PL intensity is well given by

$$I_{PL} \propto N^{*}_{Er(SiO_2)} = 100\% \times \frac{N^{ex}_{Er(SiO_2)} \sigma_{abs(SiO_2:Er)} \tau_{rad}^{Er(SiO_2)} \Phi}{1+\sigma_{abs(SiO_2:Er)} \tau_{rad}^{Er(SiO_2)} \Phi} \qquad (4)$$

where $\sigma_{abs(SiO_2:Er)} = 4.17 \times 10^{-22}$ cm^2 is the absorption cross-section of Er^{3+} for the ${}^4I_{15/2} \rightarrow {}^4I_{9/2}$ transition,[16] $\tau_{rad}^{Er(SiO_2)} = 14.5$ ms is the radiative lifetime in the excited state, ${}^4I_{13/2}$,[16] Φ is the excitation photon flux, and $N^{ex}_{Er(SiO_2)} = 9.9 \times 10^{14}$ cm^{-2} is the concentration of Er ions in the SiO_2 reference sample. As shown in Fig. 3.4, the photon flux dependence of PL intensity from SiO_2:Er sample shows a linear behavior for low excitation density. Under this condition, i.e. $\sigma_{abs}\tau_{rad}\Phi \ll 1$, this formula gives a linear dependence on the flux: $N^{*}_{Er(SiO_2)} = N^{ex}_{Er(SiO_2)} \sigma_{abs(SiO_2:Er)} \tau_{rad}^{Er(SiO_2)} \Phi$. Finally, since multiple reflections at the interfaces (air-GaN, GaN-air, air-SiO_2 and SiO_2-air) also might play a role, we have employed Fresnel's equations for calculations of the photon flux from the Ti:sapphire laser entering the active layer. By substituting this into Eq. 2, we can estimate the number of excited Er^{3+} ions in GaN sample (Fig. 3.4). We rescaled the right-hand side scale of Fig. 3.4 until the solid red line, the calculated density of excited Er^{3+} ions, overlaps with the PL intensity of GaN sample.

The PL from the GaN:Er sample also shows a linear dependence on the photon flux. As mentioned above, only the isolated Er optical centers are excited under resonant excitation at 809 nm. Thus, the excitation of the isolated Er optical centers in GaN can be calculated from the photon flux and the absorption coefficient under low excitation density,

$$N^{*}_{Er(GaN)} = A\% \times \left(N^{ex}_{Er(GaN)} \sigma_{abs(GaN:Er)} \tau_{rad}^{Er(GaN)} \Phi \right) \qquad (5)$$

where A is the percentage of Er ions that are isolated Er optical centers in GaN epilayer, $\sigma_{abs(GaN:Er)} = 3 \times 10^{-20}$ cm^2, $\tau_{rad}^{Er(GaN)} = 3.3$ ms,[74] $N^{ex}_{Er(GaN)} = 1 \times 10^{21}$ cm^{-3}, and the thickness of GaN:Er epilayer is 500 nm.[103] The dash line represents the case that if all Er ions in the epilayer were optically active, A = 100%. From this calculation we determine the percentage of the isolated Er optical centers in epilayer, which is ~ 68 ± 5 %. The uncertainty of the value is determined by the fluctuation in the photon flux and the measurement temperatures. The percentage of isolated

Er optical centers is high enough that we can expect optical amplification in these materials. This value is higher than that of Eu optically active centers in GaN materials emitting at about 620 nm that had been determined by a similar approach.[80]

3.4 Conclusions

In summary, we have investigated the optical activity, the PL quantum efficiency and non-radiative transfer energy pathways between Er ions and GaN host from GaN:Er epilayers prepared by MOCVD. The PL intensity measurements under the resonant excitation (λ = 809 nm) indicate a low thermal quenching of 20% from 10 K to room temperature from Er^{3+} ions in our GaN:Er epilayer. By comparing the PL intensity from the GaN epilayer with that of the SiO_2:Er reference sample under the same conditions, we estimate the percentage of isolated Er optical centers in the GaN epilayer is approximately of 68%. The high percentage of optically active centers in GaN epilayers indicates the high potential for realizing optical amplification in GaN:Er materials grown by MOCVD. Employing the temperature dependence measurements of the PL intensity, we also have identified non-radiative channels in this material. The findings provide useful insights for further improvement of the 1.54 μm emission in material engineering towards optimizing the energy transfer between GaN host and Er ions.

Chapter 4

Observation of Optical Gain in Er-Doped GaN Epilayers

This chapter was adapted with only minor changes from the manuscript:
V. X. Ho, et al., Observation of Optical Gain in Er-Doped GaN Epilayers, Journal of Luminescence 221, 117090 (2020).

Rare-earth based lasing action in GaN semiconductor at the telecommunication wavelength of 1.5 μm has been demonstrated at room temperature. We have reported the stimulated emission under the band-to-band excitation from Er doped GaN epilayers prepared by metal-organic chemical vapor deposition. Using the variable stripe technique, the observation of the stimulated emission has been demonstrated through characteristic features of threshold behavior of emission intensity as functions of pump intensity, excitation length, and spectral linewidth narrowing. Using the variable stripe setup, the optical gain up to 75 cm^{-1} has been obtained in the GaN:Er epilayers. The near infrared lasing from GaN semiconductor opens up new possibilities for extended functionalities and integration capabilities for optoelectronic devices.

4.1 Introduction

Near infrared semiconductor lasers are essential for optical telecommunication, industrial processing, military defense, medical applications, and spectroscopy and imaging.[8, 76, 104, 105] These semiconductor light sources can be readily integrated with the silicon microelectronics technology and/or optical fiber-based devices. In this context rare-earth (RE) doping of semiconductors is of particular importance for applications in optoelectronics.[5, 9, 76] Among various RE doped semiconductors for near-infrared lasers, erbium (Er) providing light emission at the 1.5 μm window via the $^4I_{13/2} \rightarrow {}^4I_{15/2}$ radiative transition becomes a prominent candidate for near infrared applications.[5, 104] This technologically important wavelength coincides with the minimum absorption band of optical fibers currently used in telecommunication, and in the eye-safe wavelength region.[5, 16] In the past, the goal of obtaining 1.5 μm Er-doped semiconductor lasers was unsuccessfully attempted using crystalline Si,[4, 5, 6, 7] latter of SiO_2:Er sensitized with Si nanocrystals,[10, 11, 12, 13] or GaAs and AlGaAs because of the strong thermal quenching effect occurring in narrow and/or indirect bandgap materials.[14, 15]

Solid-state lasers based on RE ions doped transparent solid materials including oxide, fluorides, ceramic, and glasses provide high power light sources, sharp, atomic-like, and temperature independent luminescence bands at room temperature (RT).[8, 9] With a large bandgap, a common way to excite Er ions in such host materials used optical pumping sources in which photon energies match higher-lying intra-4f transitions. This resonant pump method provides an excitation cross-section of about three to five orders of magnitude lower compared to those of the above bandgap excitation.[16] This limitation is a big obstruction to further progress towards RT 1.5-μm lasers based on Er in micro-optoelectronic applications.

GaN semiconductor is an attractive host material for RE doping because of the direct and wide (~3.3 eV) bandgap properties. Er-doped GaN material exhibits a significant low degree of thermal luminescent quenching, and strong emission at RT under either electrical or optical excitation.[14, 16, 20] We have successfully prepared Er-doped GaN epilayer on Si (001) and sapphire substrates by metal organic chemical vapor deposition (MOCVD) with good crystallinity and high percentage of Er^{3+} optical centers, resulting in predominant photoluminescence (PL) at RT.[17, 18, 19] These prior works have provided the necessary base to achieve near-infrared RT lasers based on Er-doped GaN (GaN:Er) semiconductor material. Recently, we have reported a lasing action in GaN/AlN

multiple quantum wells in the infrared 1.5 μm region.[20] The lasing in this structure is only obtained in a small volume.

In this chapter, we describe techniques and methods to obtain lasing from GaN:Er epilayers which can be grown in a large volume (bulk GaN material). GaN has a high thermal conductivity ($\kappa \approx 253$ W/m.K)[21], and a low thermal expansion coefficient ($\alpha \approx 3.2 \times 10^{-6}$ K^{-1})[22, 23, 24] compared with other semiconductors and ceramics including silicon ($\kappa \approx 130$ W/m.K, $\alpha \approx 2.6 \times 10^{-6}$ K^{-1}),[24, 25] GaAs ($\kappa \approx 50$ W/m.K, $\alpha \approx 6.5 \times 10^{-6}$ K^{-1})[25], and YAG ($\kappa \approx 12$ W/m.K, $\alpha \approx 6.4 \times 10^{-6}$ K^{-1})[26, 27]. Thus, we can obtain high energy and high power lasers in the GaN material. Here, we report the RT lasing in GaN:Er epilayers at 1.5 μm by the variable stripe length technique, and an optical gain up to 75 cm^{-1} under the above bandgap excitation.

4.2 Results and discussion

In this section, we used the variable stripe length techniquie to demonstrate the RT lasing in the GaN:Er epilayers at 1.5 μm and to estimate the optical gain up to 75 cm^{-1} under the band-to-band excitation. Two kinds of measurements in the variable stripe length techniquie are edge-emission measurements and gain measurements.

4.2.1 Edge-emission measurements

Details of growth conditions and epilayer structure were described in Chapter 2.[18, 73] The percentage of Er optical centers has been estimated by comparing the PL intensity at RT between the GaN:Er material and a SiO_2:Er reference sample under the resonant excitation, $^4I_{15/2} \rightarrow {}^4I_{9/2}$ transition, providing by a tunable Ti:sapphire laser at 809 nm. The estimated percentage of Er^{3+} ions emitting 1.5 μm photons is about 68% of the total Er ions that presented in Chapter 3.[19] The achievement of the high percentage of active Er ions indicates a high potential for realizing optical amplification in GaN:Er epilayers.

To determine the threshold and the net optical gain in the Er-doped GaN epilayer under the above bandgap excitation, we have performed edge-emission measurements using the well-established variable stripe length (VSL) technique.[106] The GaN:Er sample was optically excited by a UV Argon laser providing photons at 351 nm (or 3.531 eV) at RT. The laser beam was expanded by a beam expander and a center part selected with a 4x4-mm square slit in order to achieve a square homogeneous excitation. After that, the laser beam was focused onto the top

surface of the sample using a cylindrical lens with the focal length of 75 mm to obtain a stripe-shaped excitation beam of 8-μm width. The homogeneous stripe-laser beam was verified by scanning the beam profile using a UV photodetector mounted on a two-dimensional linear stage. An adjustable shield was placed on the top of the sample to control the excitation length up to 1000 μm.[20] To achieve lasing operation, an optical cavity has been created from both polished edges of the sample. Two converging lenses with focal lengths of 10 and 24 cm were used to collect the edge-emission. The emission was focused onto an entrance slit of a high-resolution spectrometer (Horiba iHR550). We obtain the resolution of PL spectra of 0.05 nm. The signal was detected by a sensitivity photodetector (InGaAs DSS-IGA).[74]

Light emitted from the sample surface has spontaneous emission features, whereas light collected from the edge of the sample contains both spontaneous and stimulated emission characteristics. In contrast to the spontaneous emission on the surface, spectral peaks of the PL intensity of the GaN:Er epilayer from the edge of the sample become narrower, and their intensity grows exponentially when pump fluence or excitation length increases (Fig. 4.1). As previously reported,[18, 72, 74] the surface emission exhibited a broad peak round 1.5 μm with the full-width at half maximum (FWHM) of ~45 nm (~22 meV) under the above bandgap excitation, and the PL intensity as a function of pump power at 1.5 μm showed a linear and saturated behavior. This is typical for spontaneous emission of GaN:Er epilayers at RT. The broadening of the PL spectrum at RT is due to the thermal population of higher-lying sublevels of the $^4I_{13/2}$ manifold and multiple optical centers in the GaN:Er material. However, the PL spectra of the edge-emission at high excitation pump fluence show several narrow PL lines (Fig. 4.1). Typically, the optical gain obtains a maximum around the peaks of the spontaneous emission spectrum, thus, the "gain narrowing" of PL lines appears in the spectra at high pump power.[107, 108] A deconvolution into several Gaussian components of the PL spectrum has been shown in the Fig. 4.1. The intensity of narrow PL lines at 797.71 and 806.89 meV exhibits an increasing from linear to exponential behavior.

We have investigated the PL intensity of the edge-emission from Er optical centers by varying the pump intensity of the UV laser from 0.5 to 500 mJ.cm^{-2} under a fixed excitation length of 0.2 mm. Fig. 4.2a shows PL intensity at 806.89 meV as a function of pump fluence. In the linear plot (Fig. 4.2, inset) the PL intensity shows a linear dependence at low pump fluence and a super-linear

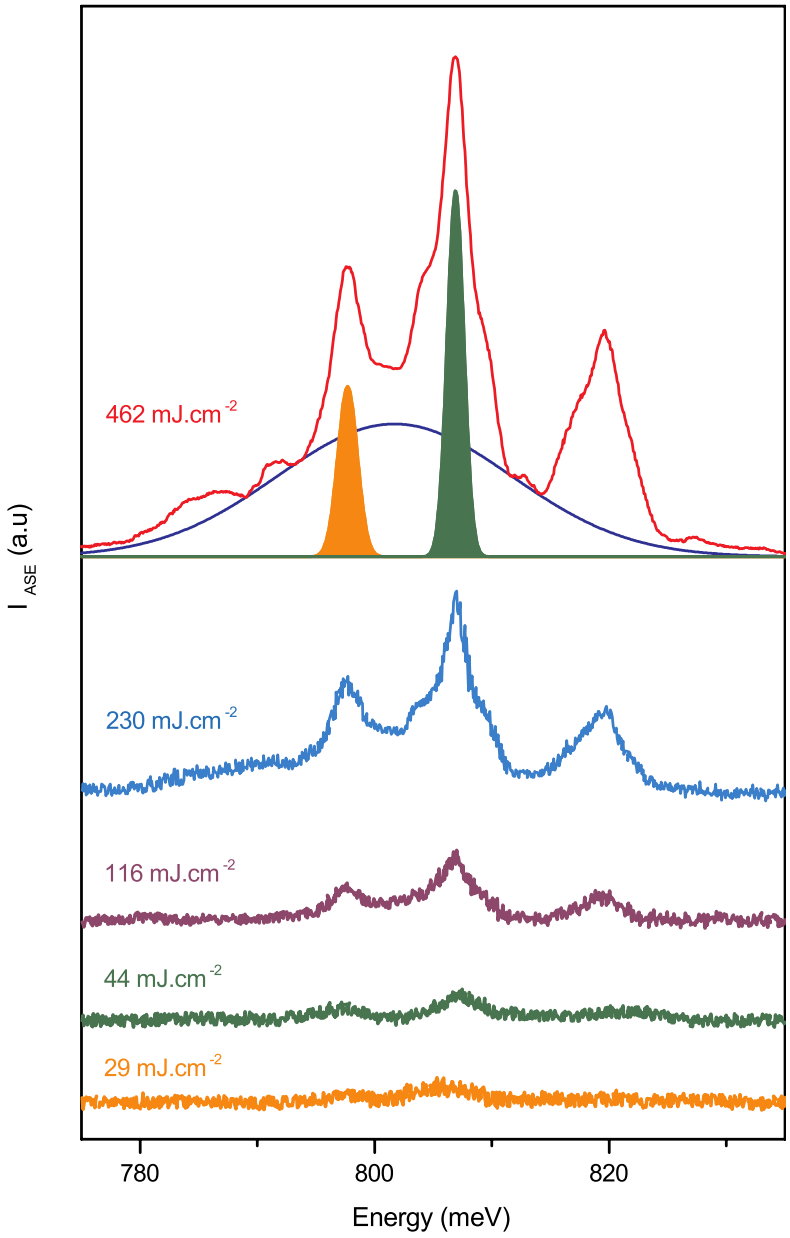

Figure 4.1: *The edge PL spectra from a GaN:Er epilayer using a UV Ar laser, λ_{exc} = 351 nm, for the above bandgap excitation. The excitation length was 0.2 mm and the pump fluence is varied from 0.5 to 500 mJ.cm^{-2}. The PL signal at low pump intensity shows a broad spectrum with a typical FWHM of ~22 meV. When the pump intensity from the UV laser is high enough to have a net gain in the optical layer, the spontaneous photons are exponentially amplified. Under this condition, spectral linewidths become narrower. The spectrum at high pump intensity was deconvolved into several Gaussian peaks. The most prominent PL lines at 797.71 and 806.89 meV show a FWHM of 1.60 ± 0.35 meV.*

behavior at high pump fluence, indicating a transition from the spontaneous emission to the amplified stimulated emission. Above a certain value of pump fluence, the PL lines become narrower. The observed spontaneous-to-simulated emission transition is a clear evidence of optical amplified spontaneous emission (ASE) in GaN:Er epilayers.

4.2.2 Rate equation

To estimate the gain threshold value, we have employed the coupled rate-equation analysis to explore the experimental results of the light-in-light-out (L-L) curve of Er-doped GaN epilayers with a simple cavity. Fig. 4.2a represents the logarithmic plot of the PL intensity at 806.89 meV as a function of the pump fluence with a fixed excitation length of 0.2 mm. Specifically, the rate-equations describe the evolution of the carrier density, N, in the active region, and the photon density, P, in the cavity mode under optical pumping:[109]

$$\frac{dN}{dt} = \frac{\eta_a R_p}{\hbar\omega V} - \frac{N}{\tau_{sp}} - \frac{N}{\tau_{nr}} - v_g g P \quad (1)$$

$$\frac{dP}{dt} = \Gamma v_g (g - g_{th}) P + \Gamma\beta \frac{N}{\tau_{sp}} \quad (2)$$

where R_p is the optical pumping rate; η_a is the fraction of the pump fluence absorbed by the active medium in a volume, V, of the GaN:Er epilayer; $\hbar\omega$ is the photon energy of the pump beam; $1/\tau_{sp}$ is the spontaneous emission rate with the decay time constant, τ_{sp}, of 3.3 ± 0.3 ms;[74] $1/\tau_{nr}$ is the non-radiative recombination rate; $v_g = c/n$ is the group velocity; n = 2.6 is the refractive index of the material; Γ is the optical confinement factor of the lasing mode; β describes the amount of spontaneous emission that couples into the laser cavity mode; g is the material gain; and g_{th} is the threshold gain. A linear relation between the material gain, g, and carrier density, N, is assumed in the active region, $g = a(N - N_{tr})$, where a is a material constant, and N_{tr} is the transparency carrier density. The transparency carrier number does not affect the fitting result, so we set this value to be zero. Non-radiative decay processes produce additional losses, which result in a large β factor, however the non-radiative recombination rate has no considerable impact on the fit.[110]

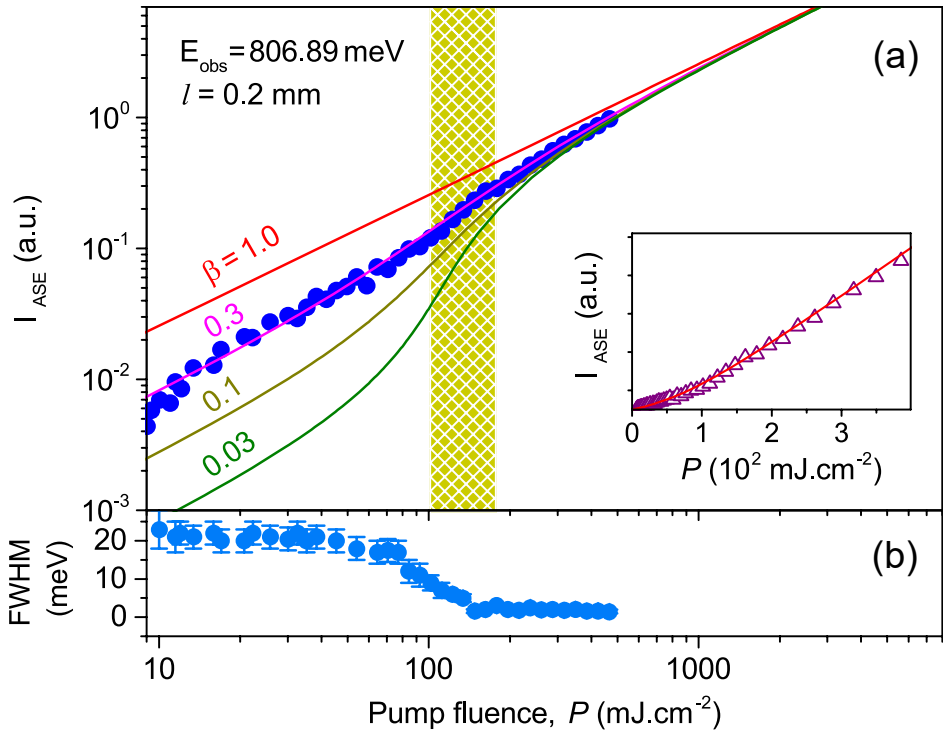

Figure 4.2: *Output intensity of the edge-emission for the PL line at 806.89 meV as a function of pump fluence with the excitation length of 0.2 mm. (a) The light-in-light-out data on the log-log scale shows a lasing threshold of 110 mJ.cm^{-2}. The result was fitted to the S-curve model. The best fitting curve has been obtained for the coupling factor, β = 0.3, for the experimental data. Inset: The edge-emission PL intensity showing a threshold for a transition from the spontaneous emission to the amplified stimulated emission. (b) The FWHM of the PL intensity from the edge of the sample becomes narrower.*

For the steady-state solution of the above rate equations, we set $dN/dt = 0$ and $dP/dt = 0$ to obtain.[109]

$$R_p = \frac{v_g g_{th} P}{\left(aP + \beta \frac{1}{\tau_{sp} v_g}\right)} \left(aP + \frac{1}{\tau_{sp} v_g}\right) \qquad (3)$$

We have fitted the experimental L-L curve to Equation 3 by first finding the material constant, a, that matches the measured threshold pump fluence at which a nonlinear jump of the output intensity was observed. Then the spontaneous emission factor, β, was varied until the best fit to the experimental data points was obtained. The lasing threshold for the excitation length of 0.20 mm was ~110 mJ.cm^{-2} of the pump fluence, which corresponds to the spontaneous emission

coupling factor, β = 0.3 (Fig. 4.2a). For comparison, L-L curves for several β values are included, clearly showing the condition of the lasing threshold. When the pump intensity is higher than the threshold for ASE, most of Er ions in the excited state are stimulated to generate photons into waveguide modes, resulting in a large amount of photons emitted from the edge of the waveguide.[107, 111, 112, 113] A net optical amplification has been achieved. Correspondingly, for the fixed optical excitation length of 0.20 mm, the FWHM of the peak at 806.89 meV becomes narrow and is about 1.65 ± 0.35 meV when the fluence of the optical pump is above 110 $mJ.cm^{-2}$ (Fig. 4.2b). Note that the lasing threshold in the GaN:Er epilayer is a few times higher than those from Er-doped GaN nanolayers in multiple quantum well GaN/AlN structures.[20, 68] In these structures, the multiple quantum wells provide an enhancement of the quantum efficiency for the infrared (1.5-μm) emission band through strain engineering, and carrier/exciton quantum confinement effect.[20, 68]

4.2.3 Gain measurements

To explore the gain coefficient from the peaks of PL emission, we have used the well-known VSL method. The active GaN:Er epilayer was excited optically in a stripe geometry by the UV laser providing the above bandgap excitation. In the VSL method, the spontaneous emission, I_{SPONT}, increase significantly when it passes the excitation volume of the sample within the waveguide. As a result of the increasing, the ASE signal, I_{ASE}, becomes visible and depends on the excitation length from the edge of the sample. Fig. 4.3 presents the ASE intensity as a function of the excitation length. Using a one-dimensional model for the amplification, the modal gain, g, can be obtained from the excitation length, l, and the intensity, I_{ASE}:[106]

$$I_{ASE}(l,\lambda) = \frac{A \cdot I_{SPONT}}{g}\left(e^{g \cdot l} - 1\right) \qquad (4)$$

where A is a constant related to the cross-section for the spontaneous emission, and the modal gain, g, is the net optical gain coefficient defined by the gain minus losses of the material.

The increase of the excitation length obviously corresponds to the increase of optical pump excitation. When the optical pump excitation is high enough to achieve an optical amplification, the spontaneous emission is amplified exponentially by stimulated emission as they travel through the active medium of the waveguide, resulting in an exponential increase in emission. Consequently, with the increase of the excitation length, we have observed an appearance of the

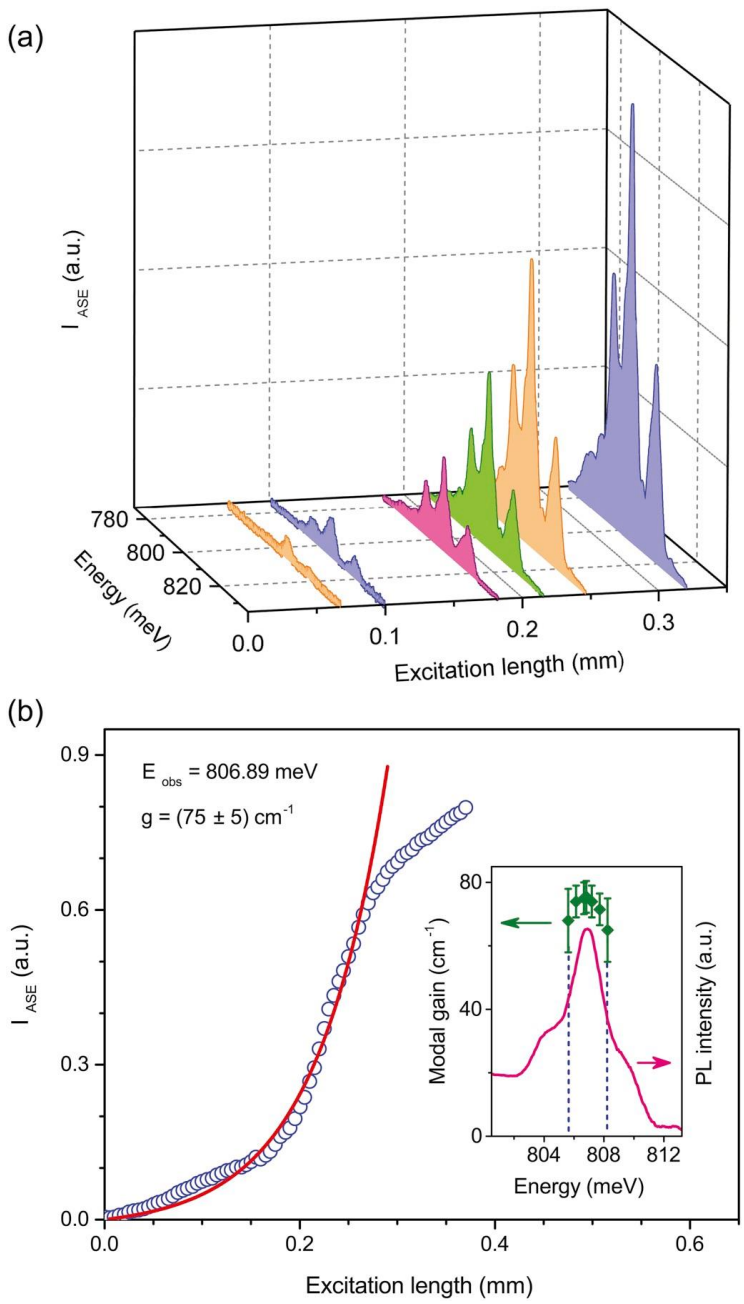

Figure 4.3: *Optical amplification observation through the variable stripe length setup. (a) Edge emission PL spectra from a GaN epilayer under the above bandgap excitation, λ_{exc} = 351 nm, with different excitation lengths, and the pump intensity of 240 mJ.cm^{-2}. (b) PL intensity of the edge-emission for the PL line at 806.89 meV as a function of excitation length. The open circles are experimental data, and the solid line is the fitted curve using the one-dimensional amplification model. Inset provides the spectral dependence of the modal gain for output intensity around 806.89 meV.*

dominant sharp peaks at 797.71 and 806.89 meV over the spontaneous emission, and the emission intensity behavior changes from linear to exponential at the sharp peaks (Fig. 4.3a). This is a direct signature of optical gain from Er optical centers in GaN epilayer around 1.5 μm at RT. We focus on analyzing the strongest PL line at 806.89 meV. Under the pump fluence of 240 $mJ.cm^{-2}$, the emission intensity as a function of the excitation length for the sharp spectral peak exhibits a clear super-linear behavior. The red solid curve in Fig. 4.3b represents the best fitting curve based on Eq. 4 with the net optical gain of ~75 ± 5 cm^{-1}. At a long excitation length (≥ 0.28 mm), the amplifier spontaneous emission shows a saturation behavior caused by the depletion of excited Er^{3+} centers as the intense light travels through the waveguide. We also have performed the spectral dependence of modal gain in this narrow-simulated emission bandwidth (Fig. 3b, inset), from which we have obtained the model gain at the PL line of 75 ± 10 cm^{-1}. The high modal gain provides us a possibility of the near infrared lasing under electrical pumping by incorporating GaN epilayers into GaN light emitting structures.

4.3 Conclusion

In summary, we have investigated the light amplification and stimulated emission of Er optical centers in GaN epilayers (bulk GaN crystal) prepared by MOCVD under the above bandgap excitation. Lasing action has been observed at 1.5 μm at RT. The observation is accompanied by the stimulated threshold, spectral linewidth narrowing, and strong modal gain in this material. The high modal gain indicates that it is feasible to realize electrically pumped lasing in the GaN:Er epilayers grown by the

2MOCVD technique for high energy and high power semiconductor laser. The realization of near infrared lasers based on GaN epilayers would provide new opportunities in optoelectronics integration with high power electronics, photonics applications

Chapter 5

Room-temperature lasing action in GaN quantum wells in the infrared 1.5 μm region

This chapter was adapted with only minor changes from the manuscript:
"Reprinted with permission from V. X. Ho, et al., Room-Temperature Lasing Action in GaN Quantum Wells in the Infrared 1.5 μm Region. ACS Photonics 2018 5 (4), 1303-1309. Copyright 2018 American Chemical Society."

Large-scale optoelectronics integration is strongly limited by the lack of efficient light sources, which could be integrated with the silicon complementary metal-oxide-semiconductor (CMOS) technology. Persistent efforts continue to achieve efficient light emission from silicon in extending the silicon technology into fully integrated optoelectronic circuits. Here, we report the realization of room-temperature stimulated emission in the technologically crucial 1.5 μm wavelength range from Er-doped GaN multiple-quantum wells on silicon and sapphire. Employing the widely acknowledged variable stripe technique, we have demonstrated an optical gain up to 170 cm^{-1} in the multiple-quantum well structures. The observation of the stimulated emission is accompanied by the characteristic threshold behavior of emission intensity as a function of pump fluence, spectral linewidth narrowing and excitation length. The demonstration of room-temperature lasing at the minimum loss window of optical fibers and in the eye-safe wavelength region of 1.5 μm is highly sought-after for use in many applications including defense, industrial processing, communication, medicine, spectroscopy and imaging. As the synthesis of Er-doped GaN epitaxial layers on silicon and sapphire has been successfully demonstrated, the results laid the foundation for achieving hybrid GaN-Si lasers providing a new pathway towards full photonic integration for silicon optoelectronics.

5.1 Introduction

Driven by the strong need for cheap and integrable Si-based optoelectronic devices for a wide range of applications, continuing endeavors have been made to develop structures for light emission, modulation, and detection in this material system. Recent breakthroughs including the demonstration of a high-speed optical modulator in Si,[114, 115] photodetectors[116], and waveguides[117] have brought the concept of transition from electrical to optical interconnects closer to realization. However, the base for silicon photonics, namely, a group IV laser source, still has to be developed. Due to the relatively small and indirect band gap, silicon is a poor light emitter. Nevertheless, lasing devices based on Si have been demonstrated including Si-based impurity lasers,[118] a Raman laser,[119] Si nanocrystals,[120] nanopatterned crystalline Si,[121] GeSn alloy on Si,[122] Ge dots in Si,[123, 124] and InGaAs/GaAs nano-lasers grown on Si.[125] However, these prototype devices essentially lack the advantages associated with the silicon system by requiring an external pump laser source or function only at low temperatures. While room-temperature luminescence has been realized,[120, 126] population inversion and optical gain have been under discussion and fundamental problems remain.

The incorporation of rare earth elements into semiconductor host gives rise to sharp, atomic-like and temperature independent emission lines under either optical or electrical excitation.[5, 77, 104, 127, 128] Er ions with intra-4f shell transitions from its first excited state ($^4I_{13/2}$) to the ground state ($^4I_{15/2}$) produce 1.5 μm emission which falls within the minimum loss window of optical fibers for optical communications and in the eye-safe wavelength region. Lasers operating around 1.5 μm are highly sought-after for use in defense, industrial processing, medicine, spectroscopy, imaging and various other applications where the laser beam is expected to travel long distances in free space. With a tremendous effort, 1.5 μm emission from Er doped narrow-bandgap semiconductors including Si and GaAs has a low efficiency at room-temperature due to the strong thermal quenching effect.[14, 104]

5.2 Results and discussion

In this section, we will discuss the enhancement of the 1.5-μm emission of the GaN:Er multiple quantum wells by using the quantum confinement effect under band-to-band excitation. We also estimated percentage of the Er optically active centers under resonant excitation. Then, we used

the variable stripe length techniquie to demonstrate the RT lasing in GaN:Er multiple quantums wells at 1.5 μm and to estimate the optical gain up to 170 cm^{-1} under the band to band excitation.

5.2.1 Photoluminescence of GaN:Er multiple quantum wells

Recently, we have successfully synthesized GaN:Er epilayers on Si (001)[17, 129] and c-plane sapphire[18] substrates by metal organic chemical vapor deposition (MOCVD) with excellent material qualities. The above host bandgap[17, 18, 74, 129] and electroluminescence[130] excitation of Er optical centers produced predominant light emission at 1.5 μm range. In order to overcome the challenges of growth of III-nitrides on Si (100) substrate due to the different crystalline structures between GaN and Si, we have employed selective area growth and epitaxial lateral overgrowth techniques to prepare GaN/AlN/Si (100) templates.[17] The X-ray diffraction and photoluminescence (PL) measurements indicated that GaN:Er epilayers grown on Si and sapphire have high crystallinity, without second phase formation,[17, 18, 129] and exhibit a strong room-temperature emission at 1.5 μm with a low degree of thermal quenching.[18, 74] In this work, a set of 200-period Er-doped GaN/AlN multiple quantum wells (MQWs:Er) produced a significant improvement of the quantum efficiency of the 1.5 μm emission via carrier quantum confinement and strain engineering[68] (see schematic in Fig. 5.1a). The growth process was started with AlN buffer and template layers and then followed by the growth of the MQWs:Er. The structure consists of alternating layers of Er doped GaN quantum wells and undoped AlN barriers (see in Chapter 2). A detail description of the growth process and epilayer structure has been reported previously.[68]

Typical room-temperature PL spectra from the MQWs:Er samples and a single GaN:Er epilayer show a broad spectral feature[68] around 1.5 μm under the band-to-band excitation using an Ar laser at 351 nm (Fig. 5.1b, inset). The PL spectrum was collected from the surface of the sample, which is the spontaneous emission of light from Er optical centers in MQWs. As previously reported, the full-width at half-maximum (FWHM) of the 1.5 μm emission at room temperature is 50 nm for a single GaN:Er epilayer[18, 74] and 60 nm for MQWs:Er materials.[68] The broadening of the emission in MQWs is due to the fluctuation of the GaN quantum well width and the local atomic structures around Er optical centers. This is especially a factor for Er optical centers located close to the quantum well/barrier interfaces. The emission intensity from the MQWs:Er structure is an order of magnitude higher than that of a single GaN:Er epilayer with the same Er doping active layer thickness and concentration under the over bandgap excitation, λ_{exc} = 351 nm.

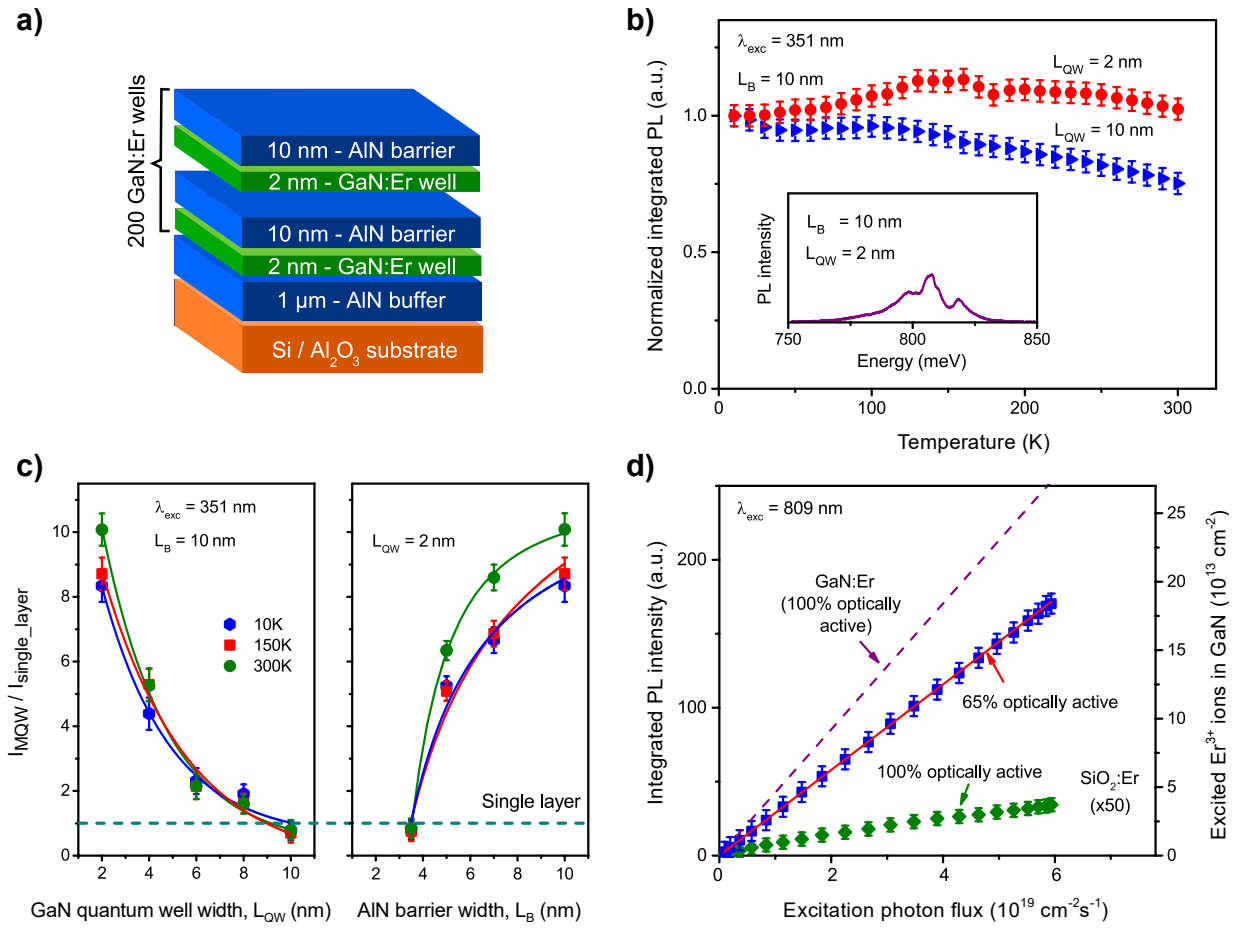

Figure 5.1: *Schematic of Er doped GaN/AlN MQWs and PL intensity data at 1.5 μm.* ***a****, A 200-period MQWs:Er sample with the GaN quantum well width, L_{QW}, of 2 nm and the AlN barrier thickness, L_B, of 10 nm.* ***b****, The temperature dependence of PL intensity for two samples with the same the barrier thickness, L_B = 10 nm, but two different quantum well widths, L_{QW} = 2 nm and 10 nm, under the band-to-band excitation, λ_{exc} = 351 nm. Inset: a typical PL spectrum from MQWs:Er materials and a single GaN:Er epilayer collected from the surface showing the spontaneous emission process.* ***c,*** *Integrated PL intensity ratio of MQWs:Er samples to a single GaN:Er epilayer at 1.5 μm as a function of the quantum well width, L_{QW} (left) and the barrier thickness, L_B (right), measured at different temperatures from 10 K to room-temperature under the over bandgap excitation. The maximum PL intensity was obtained with a MQWs:Er sample having L_{QW} = 2 nm and L_B = 10 nm.* ***d****, Comparison of the integrated PL intensity of Er^{3+} ions in MQWs with the reference SiO_2:Er sample under the resonant ($^4I_{15/2} \rightarrow {}^4I_{9/2}$) excitation, λ_{exc} = 809 nm. Measurements indicated that ~ 65% of Er^{3+} ions are optically active centers in the MQWs:Er sample with L_{QW} = 2 nm and L_B = 10 nm.*

The strong quantum confinement effects on the Er emission have been studied for different values of quantum wells and barriers. In Fig. 5.1c, the integrated PL intensity ratio of MQWs:Er samples, I_{MQW}, to a single GaN:Er epilayer, I_{single_layer}, at 1.5 μm is shown as a function of the GaN quantum well width, L_{QW}, (left) and the AlN barrier thickness, L_B, (right), measured at temperatures from 10 K to room-temperature. As shown in Fig. 5.1c (left) for MQWs:Er samples with L_B = 10 mm the integrated PL intensity, I_{MQW}, increases significantly when L_{QW} was reduced from 10 nm to 2 nmIn these measurements, I_{MQW} is normalized to the integrated PL intensity of the single GaN:Er epilayer, I_{single_layer}, with the same total Er doping active layer thickness and concentration. When the quantum well width, L_{QW}, is larger than 10 nm, I_{MQW} is approximately equal to I_{single_layer} (the horizontal dashed lines in Fig. 5.1c). A decreasing of the quantum well width provides a strong quantum confinement effect of carriers around Er ions, thus improving the quantum efficiency of the 1.5-μm emission from Er ions in GaN. When the quantum well width is smaller than the free exciton Bohr radius of 2.8 nm in GaN,[131] the built-in electrical fields due to the lattice mismatch between GaN/AlN produce further the strong quantum confinement effect for excitons, resulting in an efficient energy transfer from excitons to Er optical centers. The highest integrated PL intensity has been obtained for L_{QW} = 2 nm (Fig. 5.1c, left). For MQWs:Er samples with L_{QW} = 2 nm, the integrated PL intensity, I_{MQW}, is enhanced by more than one order of magnitude over that of the single GaN:Er epilayer via the variation of the AlN barrier thickness, L_B, (Fig. 5.1c, right). When the L_B is larger than the exciton Bohr radius in GaN, electron wavefunctions are localized at the quantum well. A large AlN barrier thickness provides an increased probability of capturing excitons by Er optical centers, leading to a higher excitation efficiency of Er^{3+} ions. We have obtained the maximum I_{MQW} at 1.5 μm when the AlN L_B is above 10 nm.

In order to evaluate the thermal quenching effect of the 1.5 μm emission, we have performed the temperature dependence of the integrated PL intensity of MQWs:Er samples under the band-to-band excitation, λ_{exc} = 351 nm. The PL experiments were carried out in a variable temperature closed-cycle optical cryostat (Janis) providing a temperature range from 10 K to 300 K. The integrated PL intensity of Er in the single GaN:Er epilayer, I_{single_layer}, is reduced by about 20% from 10 K to room-temperature (Fig. 5.2a).[74] The integrated PL intensity of Er in MQWs:Er samples, I_{MQW}, with quantum well width larger than the exciton Bohr radius in GaN and the AlN barrier thickness thinner than 10 nm follow the same temperature dependence behaviors as the single GaN:Er epilayer, I_{single_layer}, (Fig. 5.1b). However, when the thicknesses of the quantum

wells and barriers are close to the optimal parameters (L_{QW} = 2 nm, L_B = 10 nm), the temperature dependence of PL intensity is quite different. The highest value of I_{MQW} occurs at 150 K and the values of I_{MQW} at 10 K and room-temperature are comparable (Fig. 5.1b). When the temperature increases, the mobility of carriers in GaN increases significantly and reaches a maximum around 130 K.[132, 133] The increasing of the carrier mobility provides higher efficiency for the energy transfer from GaN quantum wells to Er ions, resulting in the stronger PL emission intensity. The contamination of Al in MQW structures can also provide a factor that affects the thermal property of the PL intensity of Er ions.

5.2.2 Temperature dependence of Er-doped GaN epilayer and MQWs samples

In order to investigate the thermal quenching effect of the 1.5 μm emission, we have measured the integrated photoluminescence (PL) intensity of our Er-doped GaN single layer and multiple quantum wells samples as a function of temperature.

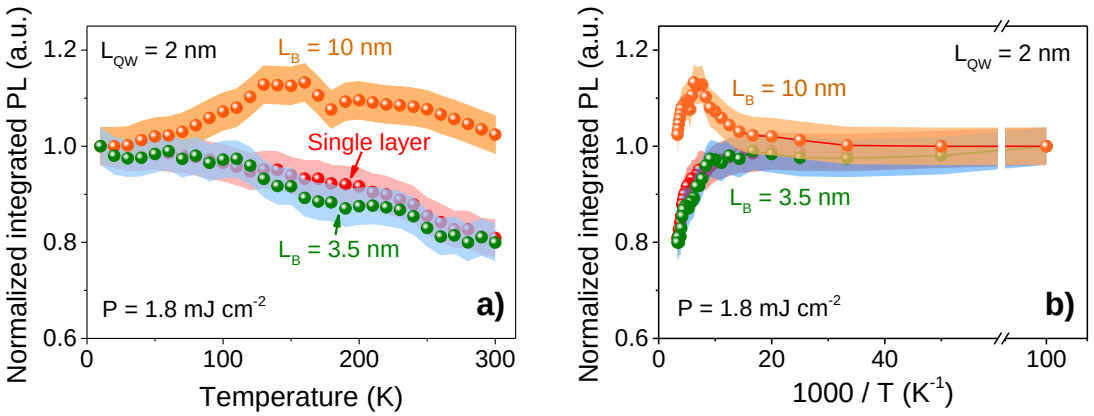

Figure 5.2: *The temperature dependence of normalized integrated PL intensity for two MQWs:Er samples with the same quantum well width of L_{QW} = 2 nm, but different barrier thicknesses of 3.5 nm (green color) and 10 nm (orange color), and a GaN single epilayer (red color). The measurements provide optimum parameters for the PL from MQWs:Er materials.*

The PL intensity reaches the maximum at 150 K for the optimum sample with the quantum well thickness of 2 nm and the barrier width of 10 nm. For MQWs with the optimal parameters with the quantum well thickness, L_{QW} = 2 nm and barrier width, L_B = 10 nm, we have obtained the highest PL intensity at 150 K, whereas the PL intensity at low and room-temperature are similar (Fig. 5.2a). Here we present the temperature dependence of the integrated PL intensity for two

MQWs:Er samples with the same the GaN quantum well thickness, L_{QW} = 2 nm, but different AlN barrier widths of 3.5 nm (Fig. 5.2a, green curve) and 10 nm (Fig. 5.2a, orange curve), and a GaN:Er single epilayer (Fig. 5.2a, red curve). In addition, we have plotted the integrated PL intensity from these samples as a function of 1000/T (Fig. 5.2b). As we mentioned, when the AlN barrier thickness is larger than the exciton Bohr radius in GaN, electron wavefunctions are localized at the quantum well, leading to a high excitation quantum efficiency of Er^{3+} ions. Specifically, when the width of AlN barriers is larger than 10 nm, the probability of capturing excitons by Er optical centers is maximum. We have obtained an order of magnitude higher in the 1.5 μm emission intensity when compared with that from the GaN:Er single epilayer[19, 134] with a comparable Er doped active layer thickness. In MQW samples with AlN barrier width of 3.5 nm, carriers are not strongly delocalized in the GaN quantum well. At elevated temperature, the mobility of carriers in GaN increases, carriers can easily escape from the GaN quantum wells, resulting in the lower intensity at high temperature. The behavior for this sample is similar with the GaN:Er single epilayer.

5.2.3 Optical activity determination

The percentage of Er dopants that emit photons upon excitation is a crucially important parameter for the potential application of Er-doped semiconductors. In particular, for emission at 1.5 μm from GaN:Er materials, it determines the PL efficiency as well as population inversion. An estimate of the number of emitting Er optical centers can be made by comparing the PL intensity of the 200-period MQWs:Er grown by the MOCVD technique with that of the SiO_2:Er reference sample under the same excitation conditions. Typically, to excite Er ions in SiO_2 we use resonant excitation. Thus, we should use the same excitation mechanism to compare the optical activity between two samples. In order to avoid the quantum confinement effect for excitons and carriers, the energy back-transfer and cascade transitions from higher energy levels of Er ion to the $^4I_{13/2}$, the experiment was performed at room-temperature under the resonant excitation for the $^4I_{15/2} \rightarrow {}^4I_{9/2}$ transition using the Ti:sapphire laser at 809 nm.

The time-integrated PL intensity of these samples was collected as a function of applied photon fluxes (Fig. 5.1d). The instantaneous PL intensities of both samples were proportional to N_{Er}^*/τ_{rad}, where N_{Er}^* and τ_{rad} are the density of excited Er^{3+} ions and their radiative lifetimes, respectively. Since the PL signal is integrated over time, the result of the experiment will be proportional to

$N^*_{Er} \times \tau/\tau_{rad}$, where τ is the effective PL lifetime. To obtain the number of photons coming out of the sample, the quantum efficiency can be determined by the refractive index of the material for a specific wavelength. We ignore in this calculation photon reabsorption, therefore, the ratio of the number of photons emitted from the two investigated samples is given by:

$$\frac{I_{GaN:Er}}{I_{SiO_2:Er}} = \frac{\eta_{GaN}}{\eta_{SiO_2}} \frac{N^*_{Er(GaN)}}{N^*_{Er(SiO_2)}} \frac{\left(\tau_{eff}^{Er(GaN)}/\tau_{rad}^{Er(GaN)}\right)}{\left(\tau_{eff}^{Er(SiO_2)}/\tau_{rad}^{Er(SiO_2)}\right)} \quad (1)$$

Where, η is the extraction efficiency. The ratio of the extraction efficiencies can be calculated from the refractive indexes of GaN and SiO_2 materials:

$$\frac{\eta_{GaN}}{\eta_{SiO_2}} = \frac{n_{air}^2/(4n_{GaN}^2)}{n_{air}^2/(4n_{SiO_2}^2)} = 0.389 \quad (2)$$

where n_{GaN} and n_{SiO2} are the refractive indexes of 2.318 and 1.445 at 1.5 μm for GaN and SiO_2, respectively.

Under resonant excitation, the decay dynamics of PL from Er optical centers appears as a single exponential with a decay time constant of 3.3 ± 0.3 ms.[74] The value is similar to previous reports on Er in GaN.[83, 100, 101] The decay dynamics is effectively independent of temperature over the entire range from 10 K to room-temperature.[74] Thus, the decay time constant of 3.3 ms is the radiative lifetime, and the $\tau_{eff}^{Er(GaN)}/\tau_{rad}^{Er(GaN)} = 1$. For the SiO_2:Er standard sample, Er embedded in the insulating host matrix and defect free material, we obtain $\tau_{eff}^{Er(SiO_2)}/\tau_{rad}^{Er(SiO_2)} = 1$.

The well-characterized SiO_2:Er sample is used to relate the measured PL intensity to a particular density of excited Er^{3+} ions. The number of excited Er^{3+} ions in the SiO_2 reference sample can be calculated through excitation photon flux when we assume that all Er^{3+} ions are equivalent, and they all contribute to the PL process. As has been discussed previously,[74, 79, 102, 128] under steady state conditions, the photon flux dependence of Er PL intensity is well described with the formula:

$$I_{PL} \propto N^*_{Er(SiO_2)} = 100\% \times \frac{N_{Er(SiO_2)}\sigma_{abs(SiO_2:Er)}\tau_{rad}^{Er(SiO_2)}\Phi}{1+\sigma_{abs(SiO_2:Er)}\tau_{rad}^{Er(SiO_2)}\Phi} \quad (3)$$

where $\sigma_{abs(SiO_2:Er)} = 4.17 \times 10^{-22}$ cm^2 is the absorption cross-section of Er^{3+} for the $^4I_{15/2} \rightarrow {}^4I_{9/2}$ transition,[16] $\tau_{rad}^{Er(SiO_2)} = 14.5$ ms is the radiative lifetime in the excited state, $^4I_{13/2}$,[16] Φ is the excitation photon flux, and $N_{Er(SiO_2)} = 9.9 \times 10^{14}$ cm^{-2} is the area concentration of Er ions in the SiO_2 reference sample. As shown in the Fig. 5.1d, the photon flux dependence of PL intensity from

SiO_2:Er sample shows a linear behavior for low excitation density. Under this condition, i.e. $\sigma_{abs}\tau_{rad}\Phi \ll 1$, this formula gives a linear dependence on flux: $N^*_{Er(SiO_2)} = N_{Er(SiO_2)}\sigma_{abs(SiO_2:Er)}\tau_{rad}^{Er(SiO_2)}\Phi$. Finally, multiple reflections at the interfaces of air-GaN, GaN-air, air-SiO_2 and SiO_2-air might play a role, we have employed Fresnel's equations for our calculations of photon flux from the Ti:sapphire laser entering the active layer. By substituting this into Eq. 2, we can estimate the number of excited Er^{3+} ions in GaN sample (Fig. 5.1d). In this way we rescale the right-hand side scale of Fig. 5.1d until the solid red line, the calculated density of excited Er^{3+} ions, overlaps with the PL intensity of MQWs:Er sample.

The PL from the MQWs:Er sample also shows a linear dependence with photon flux. As we mentioned before, under resonant excitation at 809 nm, only the Er optical centers are excited. Thus, the excitation of the Er optical centers in GaN can be calculated from the photon flux and the absorption coefficient under low excitation density

$$N^*_{Er(GaN)} = A\% \times \left(N_{Er(GaN)}\sigma_{abs(GaN:Er)}\tau_{rad}^{Er(GaN)}\Phi\right) \qquad (4)$$

where A is the percentage of Er ions that are Er optical centers in MQWs, $\sigma_{abs(GaN:Er)} = 3 \times 10^{-20}$ cm^2, $\tau_{rad}^{Er(GaN)} = 3.3$ ms,[74] $N_{Er(GaN)} = 1 \times 10^{21}$ cm^{-3}, and the total thickness of GaN:Er in the MQW structure of 500 nm. The dash line in Fig. 5.1d represents all Er ions in the MQWs being optically active, i.e., or A = 100. From this calculation we have determined the percentage of Er optical centers in MQWs to be 65 ± 5 %, which is high enough to expect optical amplification in these materials. Using the same method, we found that a fraction of ~ 68% of Er ions in the single GaN:Er layer are optically active.[19] This value is higher than that of Eu optically active centers, emitting at 621 nm, in GaN:Eu material that had been determined by a similar approach.[80]

5.2.4 Optical gain measurements

In this section, we demonstrated the lasing in GaN:Er multiple quantum wells at 1.5 μm and estimated the optical gain up to 170 cm^{-1} under the above-bandgap excitation by using the variable stripe length techniquie. This tecnique includes two kinds of measurements: edge-emission measurements and gain measurements.

5.2.4.1 Edge-emission measurements

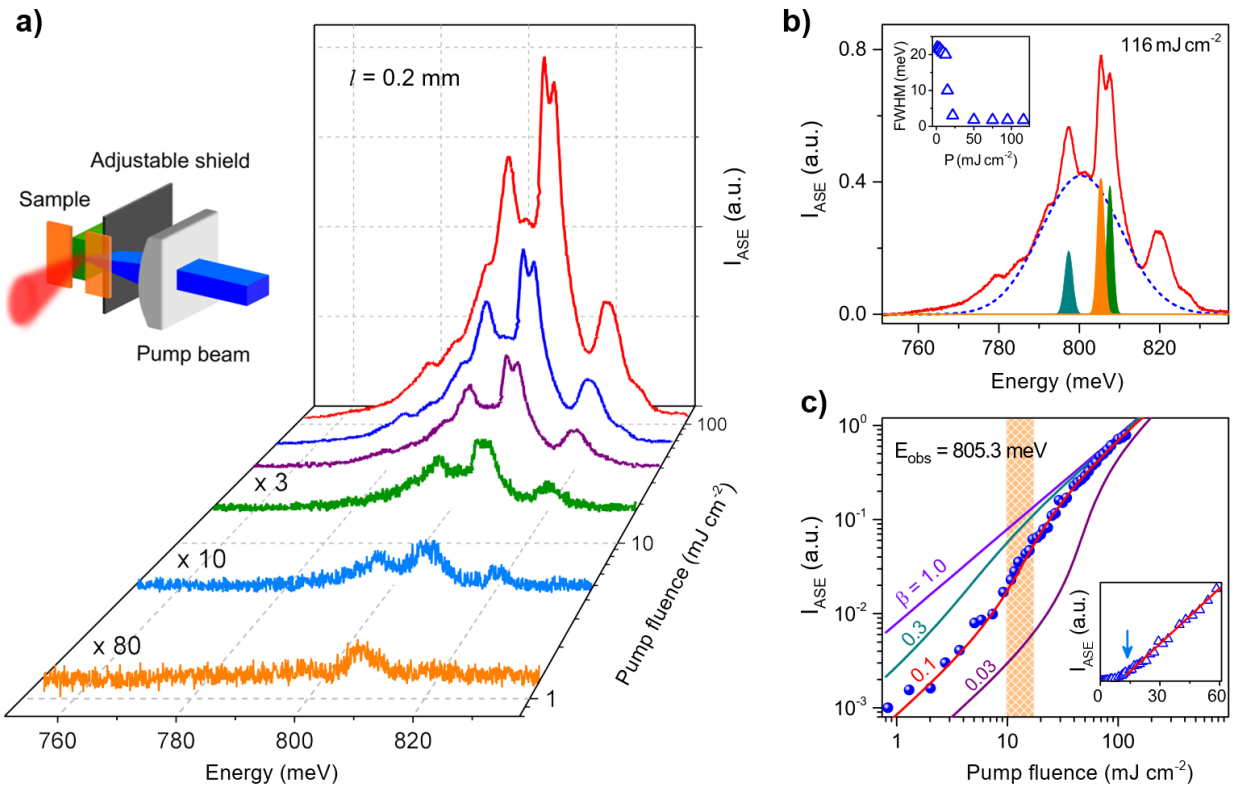

Figure 5.3: *Amplified spontaneous emission, at room-temperature, from the MQWs:Er sample with L_{QW} = 2 nm and L_B = 10 nm using an Ar laser, λ_{exc} = 351 nm, for the band-to-band excitation. a, Pump-fluence dependent PL spectra obtained with a 8 μm wide and 0.2 mm long pump excitation. At low excitation pump fluence, the emission is broad with the FWHM of 30 meV. When the pump fluence is high enough for the optical layer to have net gain, the spontaneously emitted photons are exponentially amplified by stimulated emission and the spectral peaks become narrower. Inset: Schematic of experimental configuration for edge-emission and variable excitation length measurements.* ***b,*** *PL spectrum at room-temperature with a pump fluence of 116 mJ cm^{-2} and an excitation length of 0.2 mm. The spectrum was deconvolved into 6 Gaussian peaks. The most prominent modes show a FWHM of 1.60 ± 0.25 meV. Inset: The FWHM of the Gaussian peaks decreases with increasing the pump fluence.* ***c,*** *L-L data on a log-log scale showing the dependence of the edge-emission intensity for PL peak at 805.3 meV on the pump fluence. The excitation length was 0.2 mm and the data were fitted using the S-curve model. Inset: The edge-emission intensity showing linear behavior below threshold and superlinear increase at higher pump fluence.*

The edge-emission from optically pumped MQWs:Er sample under the band-to-band excitation provides evidence of room-temperature lasing from Er optical centers in the MQW structure (Fig. 5.3a, inset). In order to achieve lasing from the MQWs:Er sample, both edges of the sample were polished to obtain a resonant cavity. The edge-emission spectra from Er optical centers are different at different pump fluence near threshold (Fig. 5.3a). In the measurements we have employed a long excitation area with 8.0 ± 0.3 μm width and 200 ± 0.5 μm length (Fig. 5.3a, inset and Methods). The photon fluence of the Ar laser was varied from 0.05 to 120 mJ cm^{-2}. At low excitation pump fluence (P < 15 mJ cm^{-2}), the emission at 1.5 μm shows a broad spectrum with the FWHM of 60 nm (~30 meV) which corresponds to the spontaneous emission[68]. The broad PL spectrum is similar to those of Er ions incorporated in insulators including SiO_2 at room-temperature. When the pump fluence is high enough (P > 15 mJ cm^{-2}) for the MQWs:Er sample to obtain a net optical gain, the spontaneously emitted photons are exponentially amplified by stimulated emission as they travel through the waveguide in the active medium, leading to a superlinear increase in emission. Since the gain is maximum near the peak of the spontaneous emission spectrum, the spectrum exhibits "gain narrowing".[107, 135] Consequently, an intense beam with spectral narrowing is emitted from the edge of the sample. The amplified spontaneous emission occurs at the wavelength where the spontaneous emission spectrum is strongest. The PL spectra at high excitation pump fluence indicate a number of strong and narrow PL lines. This is the signature of optical amplification of the spontaneous emission from Er optical centers around 1.5 μm in the MQW structure (Fig. 5.3b). We focus to analyze the strongest PL lines at 797.31, 805.30 and 807.55 meV. A deconvolution of the PL spectrum into different Gaussian components is also shown. When the pump fluencies were above 15 mJ cm^{-2}, the FWHM of the spectrum dropped to 1.60 ± 0.25 meV (Fig. 5.3b, inset). The PL intensity evolution of narrow peaks indicates a clear threshold transition from sub-threshold to linear evolution and ultimately reaches saturation at high pump-fluence (Fig. 5.3b).

A closer examination of this threshold behavior of the PL intensity emitted from the edge of the sample shows the typical superlinear (exponential) to linear transition, indicating the classical spontaneous-to-stimulated emission transition widely observed in semiconductor lasers.[112] Figure 5.3c shows the light-in-light-out (L-L) data which is the dependence of the amplified spontaneous emission on the pump fluence for the PL peak at 805.3 meV (1539.61 nm) with the excitation length of 0.2 mm. Below the threshold, the PL dependence is linear and a superlinear increase in

emission intensity with pump fluence has been observed. Subsequently, stimulated emission dominates, and the PL intensity evolution becomes linear (Fig. 5.3c, inset). Fitting the L-L data in the log-log plot to the S-curve model,[112, 136] a lasing threshold of P_{th} ~ 15 mJ cm^{-2} has been determined (Fig. 5.3c), with the spontaneous emission coupling factor, β, of 0.1. The L-L curves for different β values are also plotted for comparison, clearly showing the distinct position of the lasing threshold. Additional representative L-L plots of MQWs:Er lasing under optical pumping with different excitation lengths can be found in Fig. 5.4. Above the threshold for amplified spontaneous emission, most of the excitation were stimulated to emit light into waveguide modes, leading to a large fraction of the light emerged from the edge.[107, 111]

5.2.4.2 Rate equation analysis

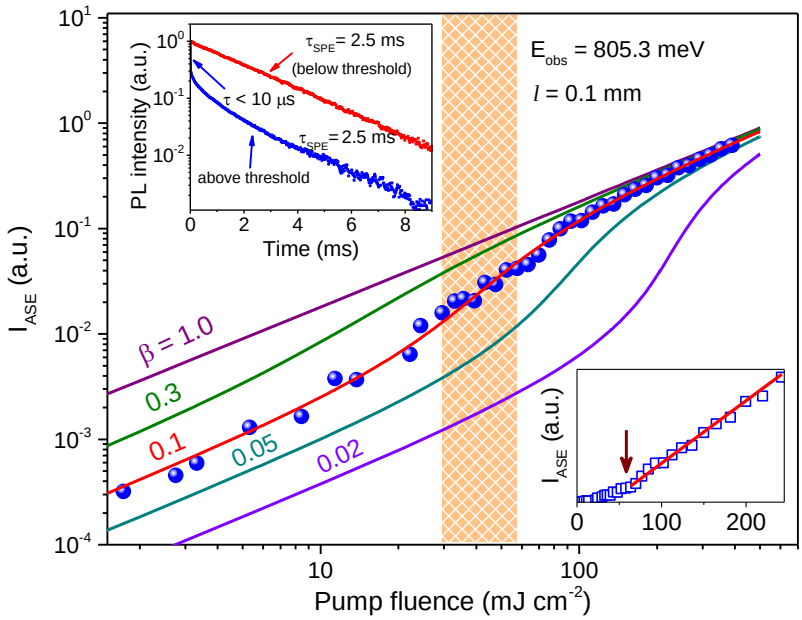

Figure 5.4: *L-L data on a log-log scale showing the dependence of the amplified spontaneous emission, I_{ASE}, on the pump fluence for the PL peak at 805.2 meV with the excitation length of 0.1 mm. The data were fitted using the S-curve model. Upper inset: Decay dynamics of PL intensity with fluence below ($P \sim 0.8P_{Th}$, red) and above ($P \sim 1.5P_{Th}$, blue) the threshold. Lower inset: Linear plot of the amplified spontaneous emission showing linear behavior below threshold and superlinear increase at higher pump fluence.*

We have employed rate equation analysis to fit the experimental light-in-light-out (L-L) curves, in order to estimate the threshold gain of the MQWs:Er sample with a simple cavity. Figure 5.4

shows the amplified spontaneous emission, I_{ASE}, as a function of the pump fluence for the PL peak at 805.2 meV (1539.80 nm) with the excitation length of 0.1 mm. The linear plot of the amplified spontaneous emission shows linear behavior below threshold and superlinear increase at higher pump fluence (Fig. 5.4, inset).[107, 135, 137]

The rate equations describe the evolution of the carrier density, N, in the active region and the photon density, P, in the cavity mode under optical pumping:[112, 113, 136, 138]

$$\frac{dN}{dt} = R_p - \frac{N}{\tau_{sp}} - \frac{N}{\tau_{nr}} - v_g g P \quad (5)$$

$$\frac{dP}{dt} = \Gamma v_g (g - g_{th}) P + \Gamma \beta \frac{N}{\tau_{sp}} \quad (6)$$

where R_p is the optical pumping rate; Γ is the confinement factor of the lasing mode; β is the spontaneous emission coupling factor; $1/\tau_{sp}$ is the total spontaneous emission rate; $1/\tau_{nr}$ is the non-radiative recombination rate; $v_g = c/n$ is the group velocity; n is the refractive index of the material; g is the material gain; and g_{th} is the threshold gain. A linear relation between the material gain, g, and carrier density, N, is assumed in the active region, $g = \alpha(N - N_{tr})$, where α is a material constant, and N_{tr} is the transparency carrier density. The transparent carrier number can be set to be zero, since it does not affect the fitting result significantly. The rate of non-radiative recombination in the MQWs is currently not known. Any non-radiative decay process would induce additional loss, which would result in a large β factor.[110] Our measurements are taken under optical pumping by a 351 nm CW Argon laser at room-temperature. For the steady state solution of the above rate equations, we set $dN/dt = 0$ and $dP/dt = 0$ to obtain.[112, 136, 138]

$$R_p = \frac{v_g g_{th} P}{\left(aP + \beta \frac{1}{\tau_{sp} v_g}\right)} \left(aP + \frac{1}{\tau_{sp} v_g}\right) \quad (7)$$

We have fitted the experimental L-L curves with Eq. 7 by first finding the material constants that match the measured threshold pump intensity where a nonlinear jump of the output intensity was observed. Then, the spontaneous emission factor, β, was varied until the best fit with the experimental data points was obtained. The lasing threshold for the excitation length of 0.1 mm was 55 mJ cm^{-2} of the pump fluence, which corresponds to the best fit for spontaneous emission coupling factor, $\beta = 0.1$ (Fig. 5.4). L-L curves for different β values are also plotted for comparison, clearly showing the distinct position of the lasing threshold.

5.2.4.3 Lifetime of photocarriers

Together with the threshold behavior, we have observed the shortening of the lifetime of Er emission in the MQW structure. A typical lifetime of Er spontaneous emission in the MQW structures with the pump fluence below the threshold is around 2.5 ms (red curve, Figure 5.4). Under a high pump fluence (above the threshold), the lifetime of Er emission shows a shortening with a dynamics < 10 μs (blue curve, Figure 5.4). The value is limited by the time-constant of our time-resolved photoluminescence setup. We have integrated the PL intensity for the fast and slow components. The PL spectrum for the fast component shows narrowing features as indicated in the Figure 5.3a at high pump fluence. The PL spectrum for the slow component is similar with the spectrum at low pump fluence. The PL intensity of the slow component can be originated from surface emission of the sample.

5.2.4.4 Gain measurements

We have employed the well-known variable excitation length method to determine the gain coefficient from the evolution of the peak-emission intensity (Chapter 2).[106] The sample was optically excited by the Argon laser providing the band-to-band excitation in a stripe geometry. The amplified spontaneous emission signal, I_{ASE}, was collected as a function of the illuminated length or the excitation length, l, from the edge of the sample. As a result of stimulated emission, the spontaneous emitted light is amplified as it passes through the excited volume to the edge of the sample. Assuming a one-dimensional amplification model, the modal gain, g_{mod}, can be extracted from the amplified spontaneous emission intensity and the excitation length:[106]

$$I_{ASE}(l) = \frac{A \times I_{SPONT}}{g_{mod}}(e^{g_{mod} l} - 1) \qquad (1)$$

where I_{SPONT} is the spontaneous emission intensity per unit length and A is the cross-section area of the excited volume, and the modal gain is the gain minus the loss of the material.

When the excitation length was varied, the emission spectral peaks became narrower as the excitation length was increased, and the output intensity grew exponentially. Figure 5.5a presents the PL spectra with an optical excitation of 109 mJ cm^{-2} for different excitation lengths. The observation of an exponential increase in the intensity and a substantial decrease in spectral linewidth (Fig. 5.5a, inset) of light emitted as the excitation length is varied is a direct indication

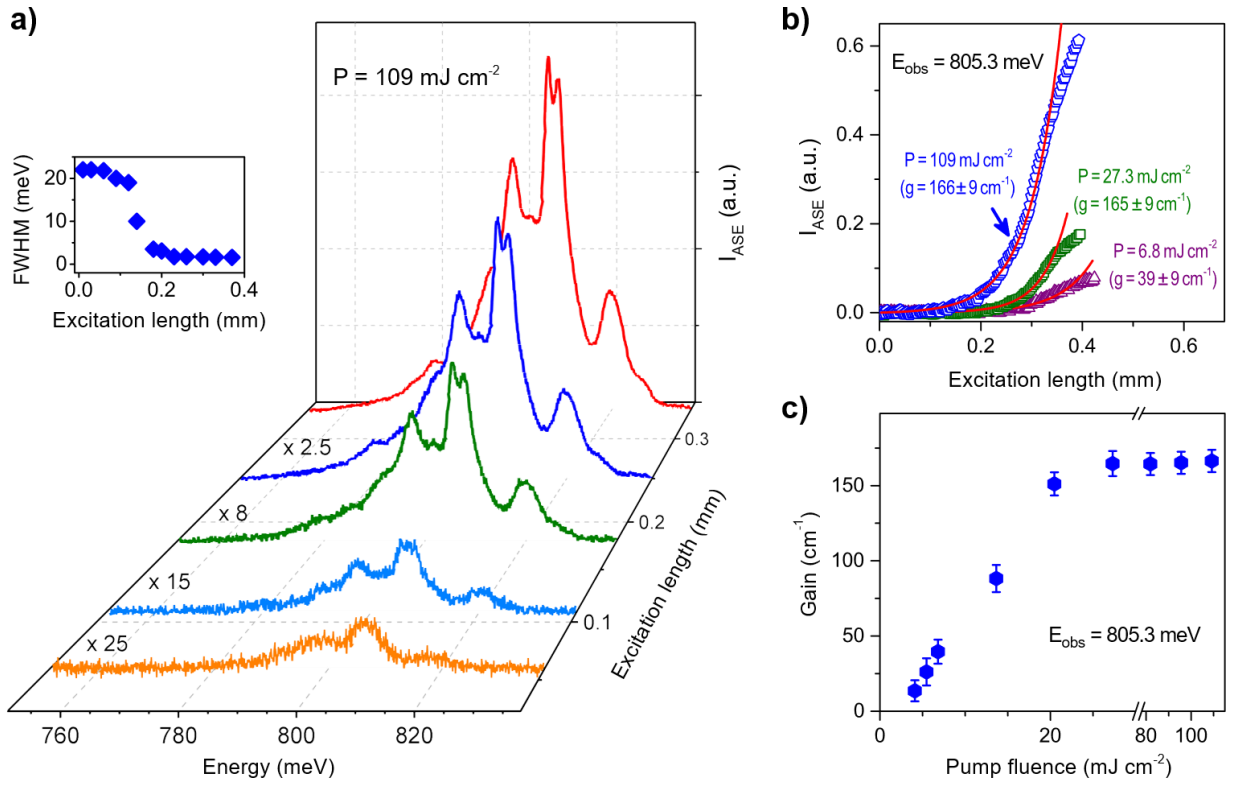

Figure 5.5: *Optical gain determination via the variable stripe length method.* ***a,*** *Edge-emission PL spectra from the MQWs:Er sample with* L_{QW} *= 2 nm and* L_B *= 10 nm as a function of the excitation length at a pump fluence of 109 mJ cm*$^{-2}$*. The PL spectra become sharper at higher pump fluence due to the amplified spontaneous emission. The narrowing of the edge-emission spectral peaks provides evidence of lasing in the MQWs:Er sample at room-temperature. Inset: The reduction of the FWHM of the deconvoluted Gaussian peaks with increasing the excitation lengths.* ***b,*** *Dependence of the amplified spontaneous emission intensity, for the PL peak at 805.3 meV, on excitation length. The modal gain of the MQWs:Er sample was determined by using Eq. 1 to the data.* ***c,*** *The net gain of the sample at 805.3 meV as a function of the pump fluence.*

of the optical gain. Fig. 5.5b shows the output intensity at the observation peak at 805.3 meV as a function of excitation length at three different pump fluence. In each case, the data can be fitted to Eq. 1. The net gain of the waveguide was measured as a function of the pump intensity (Fig. 5.5c). At higher pump fluence, the output intensity increased exponentially with excitation lengths less than 0.42 mm, and then leveled off at longer excitation lengths. This behavior can be attributed to

gain saturation, which occurs when the light traveling in the waveguide becomes so intense that it depletes a substantial fraction of the excited centers and reduces the gain coefficient. We limited the gain analysis to pump fluence <150 mJ cm^{-2} and excitation lengths <0.42 mm.

5.3 Conclusions

In conclusion, our investigations provide conclusive evidence of light amplification and stimulated emission in MQWs:Er samples. In the past, this formidable goal was unsuccessfully attempted by Er doping of crystalline Si, and later of SiO_2 sensitized with Si nanocrystals. Here we have demonstrated the realization of this long-sought goal of Si photonics in state-of-the-art GaN MQW structures grown on-Si and GaN, demonstrating for the first time the added value provided by merging of these two most important semiconductor materials – Si for standard electronics and photovoltaics and GaN for power electronics, photonics and automotive applications.

Chapter 6

Graphene-Ta_2O_5 heterostructure enabled high performance, deep-ultraviolet to mid-infrared photodetection

This chapter contains original results submitted for publication:
"Vinh X. Ho, Yifei Wang, Michael P. Cooney, and N. Q. Vinh. Graphene-Ta_2O_5 heterostructure enabled high performance, deep-ultraviolet to mid-infrared photodetection, Nature Communications (2020)"

Ultrafast, highly sensitive, low cost photodetectors operating at room temperature sensitive from deep-ultraviolet to the mid-infrared region remain a significant challenge in optoelectronics. Achievements in traditional semiconductors using cryogenic operation and complicated growth processes prevent the cost effective and practical application of broadband detectors. Alternative methods towards high-performance photodetectors, hybrid graphene-semiconductor colloidal quantum dots have been intensively explored. However, the operation of these photodetectors has been limited by the bandwidth and response time. Here, we have demonstrated hybrid photodetectors operating from the deep-ultraviolet to the mid-infrared region with high sensitivity and ultrafast response by coupling graphene with a p-type semiconductor photosensitizer, nitrogen-doped Ta_2O_5 thin film (5 nm) grown by e-beam evaporation. The photodetectors achieve a high photo-responsivity (up to 3.0×10^6 A/W), ultrafast response time (faster than 20 ns), and a specific detectivity (up to $\sim 6.5 \times 10^{14}$ Jones). The work provides a method for achieving high-performance optoelectronics operating in the deep-ultraviolet to mid-infrared region.

6.1 Introduction

The capability to convert light into electrical signals over a broad spectral range with high sensitivity and low cost is central to many technological applications including video imaging, night-vision, security, optical communication, sensing, and spectroscopy[139]. Graphene has been exhibited as a potential optoelectronic material for broadband photodetectors from the deep-ultraviolet (UV) to the terahertz (THz) region[139, 140, 141]. Unfortunately, due to the fast carrier recombination rate on the picosecond timescale[142], as well as the intrinsic low absorption[143, 144] of graphene, photodetectors based on graphene suffer from poor detectivity as well as low responsivity, preventing use in broadband applications. To enhance the light absorption, graphene is usually hybridized with other nanostructures for graphene-based photodetectors[145, 146]. Among these nanostructures, the ultrahigh photoconductive gain was obtained in hybrid colloidal quantum dots (CQDs) on graphene, where graphene acts as an ultrafast carrier transport channel and CQDs are used as an ultrahigh photon absorbing material. In these hybrid nanoscale structures, charge carriers are generated from light-absorbing CQDs. Electrons or holes are trapped in the CQDs, while the oppositely charged carriers transfer to graphene and rapidly recirculate in the graphene channel controlled by a source-drain bias voltage, leading to a photogating effect[147, 148]. Depending on CQDs, graphene hybrid photodetectors have shown a high sensitivity photodetection from the UV to near-infrared (NIR) region. However, graphene-CQD photodetectors face a limited spectral bandwidth due to the large energy of exciton peaks[145, 148], and a long response time in the millisecond to second time-scale[148].

The ultrahigh photoconductive gain of graphene-CQD photodetectors originates from the long lifetime of trapped-charge carriers that remain in CQDs and the high carrier mobility (μ = 60,000 $cm^2s^{-1}V^{-1}$)[41] of graphene at room temperature on a substrate. The gain can be determined based on a simple approximation of the trapped-charge carrier lifetime, $\tau_{\text{trapped carrier}}$, for electron or hole, and the transit time, τ_{transit}, for the opposite type carrier given by $G = \tau_{\text{trapped carrier}}/\tau_{\text{transit}}$[148]. For graphene-CQD photodetectors, the responsivity is up to ~1×10^9 A/W in the visible region[148, 149, 150] while the response time is very slow (in the order of ~10 ms or longer) due to the long lifetime of carriers trapped in the CQDs. The ultrahigh gain has been observed in many types of hybrid structures including graphene-PbS[145, 148, 151], graphene-TiO_2[149], graphene-ZnO[152], graphene-Si[150, 153], and graphene-chlorophyll (biological material)[154]. The long lifetime of trapped-charge carriers

provides an ultrahigh gain, but leading to a slow response time of the photodetector. Thus, to increase the operation speed in the graphene-CQD photodetectors, a reset voltage pulse applied to the back-gate has been used to purge charge carriers from CQDs[146, 148].

To obtain an ultrahigh photoconductive gain as well as a fast operation time, including response and recovery time of graphene based-photodetectors, we have employed a two-dimensional (2D) light-absorbing layer, a p-type semiconductor photosensitizer, nitrogen-doped tantalum oxide (N-Ta_2O_5). The N-Ta_2O_5 layer has a thickness of 5 nm grown by electron beam evaporation containing electron acceptor impurities atop graphene. Recently, this material has been used in a wide range of applications in solar energy conversion and microelectronics including photocatalytic materials[155], charge-trapping for nonvolatile resistive random access memories[156, 157], atomic switches[158], capacitors, insulators[159, 160], thin-film electroluminescent devices[161], and high-speed elements due to their high dielectric constant (κ = 25 – 40), good thermal and chemical stability, and high electrical strength. The N-Ta_2O_5 light-absorbing thin film contains defects, including acceptor impurities and trapped-charge centers at the interface, acting like negative charge centers. The long lifetime of charge centers provides an ultrahigh gain for the photodetectors, similar to the graphene-CQD photodetectors. Due to the nature of the quantum well (instead of quantum dots), ionized charges in defects of the 2D light-absorbing layer will be neutralized quickly when the light source is turned off. The devices exhibit a significantly high photo-responsivity of ~3.0×10^6 A/W in the UV-to-NIR region, and ~7.2 A/W in the mid-infrared (MIR) region. A fast response time of 20 ns or a high electrical bandwidth of ~50 MHz has been observed.

6.2 Fabrication and Characterization

In this section, we will briefly describe the fabrication process of the graphene-based photodetectors. We also characterize the morphology of N-Ta_2O_5 absorber using atomic force microscopy (AFM) and quality of graphene using Raman spectroscopy.

6.2.1 Photodetector fabrication process

The chemical vapor deposition (CVD) monolayer graphene on a copper foil from Graphenea Inc. was transferred onto a Si/SiO_2 substrate[141]. A p-doped (1 – 10 Ω.cm) Si wafer under a 300-nm-thick SiO_2 layer was used as the back gate. Metal source and drain contacts (Cr/Au with

10/100-nm thickness) for transport measurements were deposited directly onto the wafer by optical lithography to form field effect transistors (FET). The CVD graphene film on top of the wafer was transferred using the poly-(methyl-methacrylate) (PMMA) wet transfer method. The single-layer of graphene film was confirmed by the Raman spectroscopy. Using photolithography and oxygen plasma etching processes, graphene films were patterned into different shapes (L × W) on the silicon wafer. L is the gap between source and drain contacts, and W is the width of the graphene photodetector device (Fig. 6.1).

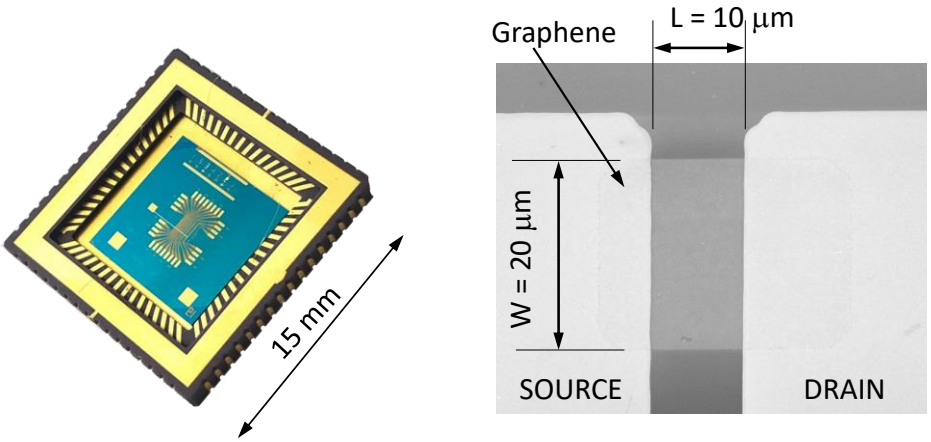

Figure 6.1: *Images of photodetectors: (left) a picture of photodetector devices including IC package, and (right) a SEM image of an individual photodetector showing the gap, L, between source and drain contacts, and the width, W, of the graphene.*

A 5-nm N-Ta_2O_5 layer was deposited on the CVD graphene by electron-beam thermal evaporation with a slow rate of 0.1 Å.s^{-1}. This layer acts as a photon absorption material and contains electron acceptor centers. Then the device was covered with a 30-nm Al_2O_3 dielectric layer using the thermal atomic layer deposition method (ALD) at 250 ^oC to protect the N-Ta_2O_5 layer from the ambient environment. Figure 6.1 shows an image of the graphene-Ta_2O_5 photodetector devices (left) and a scanning electron microscope (SEM) image (right) of an individual photodetector in the main chip.

To verify the quality of the graphene as well as the N-Ta_2O_5 films, atomic force microscope (AFM) experiments have been performed. Figure 6.2a shows an AFM image of the graphene surface with the size of 10 × 10 μm^2 after the PMMA cleaning process. The graphene surface is homogenous, and there are only a few white dots on the graphene surface in the AFM image. These

white dots were originated from PMMA residues, thus almost all PMMA residuals were removed in our photodetector devices. An AFM image in Fig. 6.2b in a short scanning range illustrates the homogeneity of the N-Ta_2O_5 layer with the thickness of 5 nm.

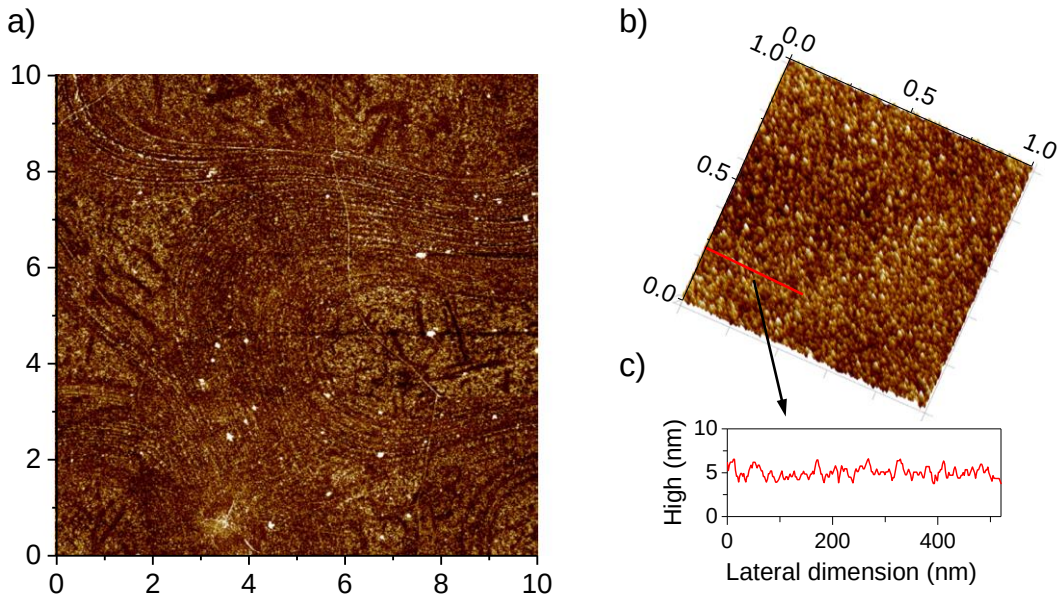

Figure 6.2: *AFM images of the graphene surface (left), and the N-Ta_2O_5 layer (right) on graphene of photodetector devices.*

6.2.2 Raman spectrum

To evaluate the quality of graphene after several fabrication steps, including the graphene transferring, the e-beam evaporation process of the N-Ta_2O_5 layer, and ALD method of the Al_2O_3 dielectric layer, the Raman spectroscopy has been employed. A Raman spectrum (Fig. 6.3) was obtained by using a WITec UHTS 300 micro-Raman spectrometer equipped with a CCD detector and a 100× objective lens (NA 0.90). The graphene sample was excited by a laser operating at 663.1-nm wavelength. Figure 6.3 shows the Raman spectrum of a CVD monolayer graphene on Si/SiO_2 covered by a 5-nm N-Ta_2O_5 film, and a 30-nm ALD Al_2O_3 dielectric layer. The Raman spectrum shows two main peaks at ~1592 cm^{-1} (G line) and ~2669 cm^{-1} (2D line). A lower peak (D line) can be observed at 1345 cm^{-1}, which indicates graphene defects. The intensity ratio of the 2D and G lines, I_{2D}/I_G, is 5.3. The high value confirms a high quality of graphene layer in the photodetector[162]. The intensity ratio of D to G lines, I_D/I_G, is correlated to the deposition process

and the oxidation of the ALD dielectric layer. This ratio value of 0.3 indicates a normal density of lattice defects in an oxide layer covered graphene[163].

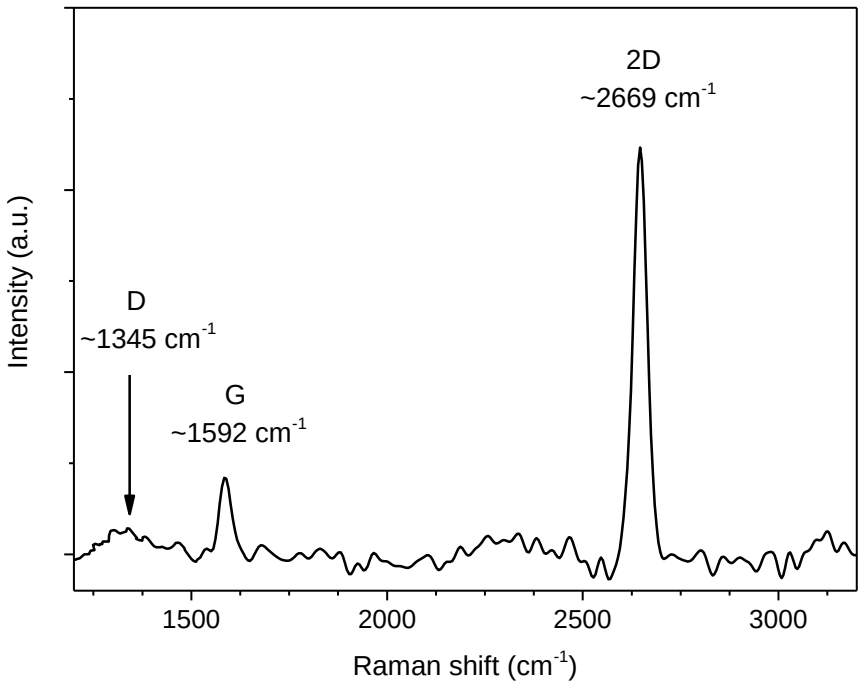

Figure 6.3: *Raman spectrum of the graphene-Ta_2O_5 photodetector device with a CVD monolayer graphene on Si/SiO_2 covered by a 5-nm N-Ta_2O_5 film, and a 30-nm ALD Al_2O_3 dielectric layer.*

6.3 Results and discussion

In this section, we characterized the figures-of-merit of the graphene-Ta_2O_5 photodetectors such as responsivity, response-time, noise equivalent power (NEP) and specific detectivity. We also proposed the model to explain the broadband detection of graphene-Ta_2O_5 photodetectors.

6.3.1 Physical mechanism: Photoconductive gain

The active area of the graphene-Ta_2O_5 photodetectors consists of a graphene sheet and a 5-nm N-Ta_2O_5 layer. Graphene acts as a carrier transport channel with the N-Ta_2O_5 thin film used as a strong photon absorbing material containing ionized acceptors. The active area is placed on top of a Si/SiO_2 wafer as illustrated in Fig. 6.4a. In contrast to earlier findings for graphene-based photodetectors, where the photocurrent occurs with the presence of charges in CQDs changing the graphene sheet resistance[148, 149, 150], in the vicinity of a p-n junction[164, 165], at the interface of graphene and metal contacts[143], a thin tunnel barrier[146], our structure shows the photo-response

over a large volume of the Ta_2O_5 thin film. The Ta_2O_5 layer is doped with nitrogen to form acceptor centers[166, 167, 168, 169, 170] during e-beam evaporation deposition, with an addition during the first few cycles of the atomic layer deposition Ta_2O_5 on top. The N-Ta_2O_5 layer contains acceptor centers with energy levels in the band gap of the material. Photons with energy higher than the energy of the acceptor centers release holes from neutral acceptors. The holes are transferred into the graphene channel, leaving behind ionized acceptors (negative charges). Due to the high mobility of graphene sheet, holes are circulated during the long lifetime of ionized acceptors. The graphene-Ta_2O_5 heterostructure offers a large spectral sensitivity from deep-UV to MIR region with very fast operation time.

The effect of light illumination on the graphene-Ta_2O_5 heterostructure photodetector with the gap between source and drain contacts, L, of 30 μm, and the width of the active area, W, of 30 μm (W/L = 1) is shown in the Fig. 6.4. Specifically, we have observed the source-drain current, I_{DS}, with and without illumination of a diode-pumped laser operating at 532 nm as a function of the back-gate voltage, V_{BG}. The power of the pump laser was varied from 300 fW to 7.5 nW. Figure 6.4b shows transfer characteristic (I-V) curves of our device for the source-drain bias voltage, V_{SD}, of 0.5 V. A shift of ~11 V of the charge neutrality point (CNP) voltage (V_{Dirac}) of the transfer characteristic curves toward positive of the back-gate voltage, V_{BG}, has been observed with increasing illumination power. The photocurrent increases for $V_{BG} < V_{Dirac}$ where the carrier transport is hole-dominated. In this case, photo-generated holes were transferred from the N-Ta_2O_5 thin film to graphene, leaving behind ionized acceptors. Thus, a high photocurrent has been observed. For $V_{BG} > V_{Dirac}$, where the carrier transport is electron-dominated, the illumination leads to a decrease in photocurrent due to the recombination taking place between holes transferred from the N-Ta_2O_5 layer to graphene and electrons induced by the back gate. As long as acceptors in the 5-nm N-Ta_2O_5 layer remain ionized (negative charge), holes in the graphene layer are recirculated, resulting in a photoconductive gain in the graphene-Ta_2O_5 heterostructure device.

By subtracting the dark-current from the illumination-current, we can determine the net photocurrent ($I_{ph} = I_{illumination} - I_{dark}$) of the device. The photocurrent curves under different illumination powers are plotted in Fig. 6.4c. A net photocurrent of ~100 μA has been observed at V_{BG} = 7 V and V_{SD} = 0.5 V. The photocurrent curves demonstrate that the magnitude of the photocurrent increases with illumination power.

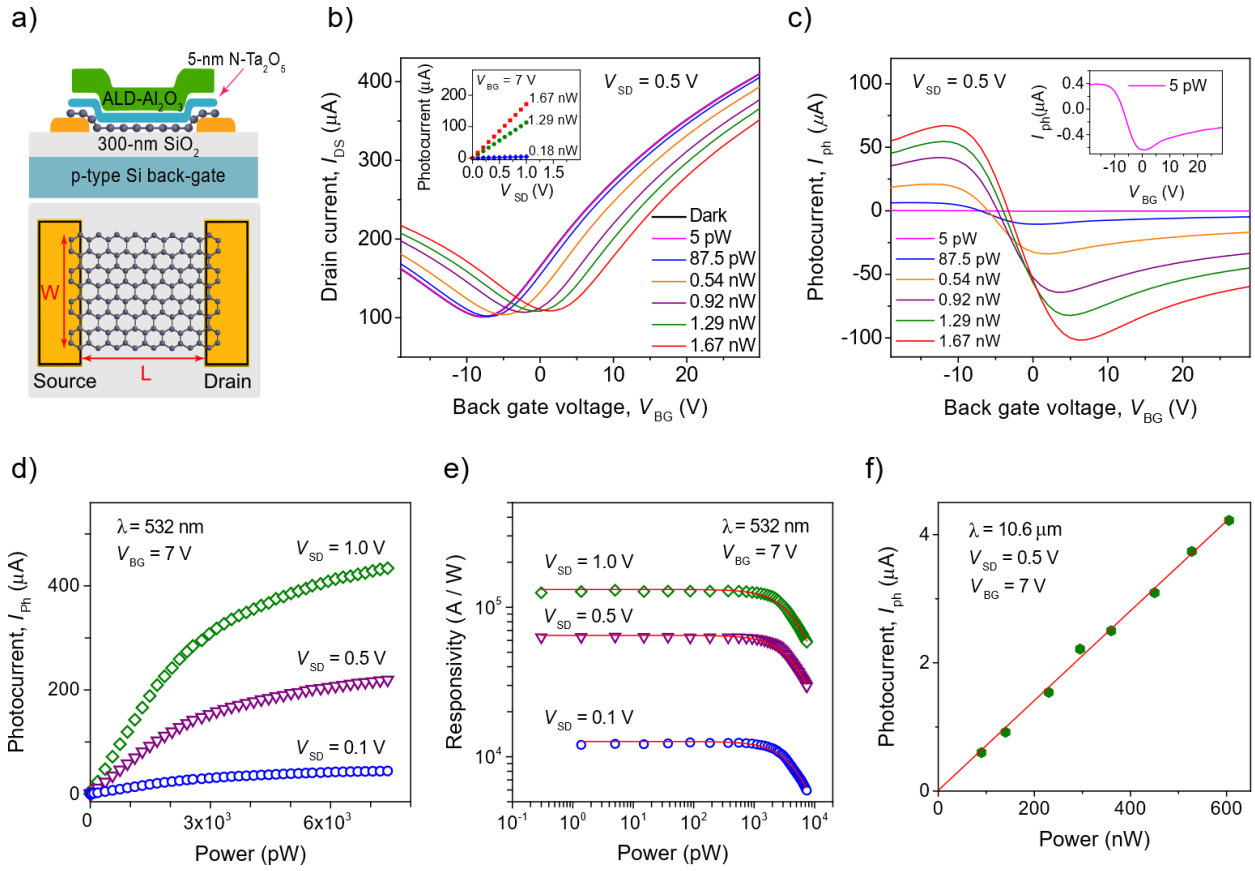

Figure 6.4: *Graphene– Ta_2O_5 hybrid thin film photodetector. (**a**) Schematic of the phototransistor showing source, drain, back gate contacts together with graphene, 5-nm N-Ta_2O_5, and 30-nm Al_2O_3 layers. (**b**) I–V_{BG} characteristics of the graphene – Ta_2O_5 photodetector under different illumination powers, and 0.5 V source–drain bias voltage. The wavelength is 532 nm with a spot size of 10 mm, covering the entire photodetector. Inset: the photocurrent increases linearly with the source–drain bias voltage. (**c**) Photocurrent curves under different illumination powers as a function of back gate voltage. The magnitude of photocurrent increases with illumination power. (**d**) Power dependence of photocurrent under different source–drain bias voltage using the lock-in technique at V_{BG} = 7.0 V for three values of the source-drain voltage, V_{SD}, of 0.1, 0.5 V, and 1 V. The photocurrent increases linearly with light intensity and grows slowly at high illumination power. (**e**) The photo-responsivity shows a constant value at low illumination power and reduces at high excitation power. (**f**) Power dependence of photocurrent using a CO_2 laser (λ = 10.6 μm) for excitation at V_{BG} = 7.0 V. A linear increase of photocurrent with illumination power has been observed.*

To gain insight into the characteristics of the graphene-Ta_2O_5 heterostructure, we carried out the power dependence of the photocurrent (Fig. 6.4d) as well as determined the photo-responsivity, $R_{ph} = I_{ph}/P$, of the photodetector for the 532-nm illumination, at V_{BG} = 7.0 V for three values of the source-drain voltage, V_{SD}, of 0.1, 0.5, and 1 V (Fig. 6.4e). Under low illumination power of 300 fW, the device shows a responsivity of 1.25×10^5 A/W, suggesting that the graphene as well as the Ta_2O_5 layers efficiently convert the photon energy into a large electrical current. The photocurrent increases linearly with illumination power from 300 fW to ~ 2 nW (almost four ordersof magnitude) and grows slowly at high illumination power. In an equivalent way, the responsivity shows a constant value at low illumination power and reduces after that (Fig. 6.4e). The photo-responsivity reduces from 1.25×10^5 to 5.85×10^4 A/W when the excitation power is higher than 2 nW. At low illumination power, ionized acceptors in the N-Ta_2O_5 layer are well separated from photon-generated electron-hole pairs, thus a high gain from the photogating effect has been obtained. As we increase the illumination power, a higher concentration of electron-hole pairs is introduced. When all acceptor centers are ionized, electrons and holes can recombine in the picosecond time-scale[142]. These holes will not take part in the charge transfer process, and thus, the photo-responsivity reduces as well as the average carrier lifetime is shortened at high illumination power.

To examine the MIR response, experiments were conducted with a CO_2 laser (λ = 10.6 μm, V_{SD} = 0.5 V, V_{BG} = 7 V). The photocurrent as a function of illumination power is shown in Fig. 1f. A linear behavior of the photocurrent with the illumination power has been observed. From the results, the photo-responsivity in the MIR region of 7.2 A/W has been obtained.

In addition, the photocurrent shows a linear dependence on the source-drain bias voltage, V_{SD},[171] (Fig. 6.4b, inset) suggesting that higher photo-responsivity can be readily obtained by applying a higher bias voltage. As can be seen from Figs 6.4d and 6.4e, with V_{BG} = 7.0 V, the photo-responsivity of the device at V_{SD} = 1.0 V is higher than those from a lower voltage between source and drain.

6.3.2 Optimum size of photodetector

The photo-responsivity depends strongly on physical parameters of the devices. Specifically, the photo-responsivity depends on the geometrical parameters, L, the distance between source and

drain contacts, and the width, *W*, of the active area. A simple electrical circuit has been developed for the graphene photodetectors[172]:

$$I_{\text{ph}} = I_{\text{illumination}} - I_{\text{dark}} = \frac{V_{\text{SD}}}{R_0 + R_{\text{illu}}} - \frac{V_{\text{SD}}}{R_0 + R_{\text{D}}} \qquad (1)$$

where R_0, R_{illu} and R_{D} are the contact resistance of the graphene-Ta_2O_5 heterostructure with electrodes, the total resistance of the active area with and without light illumination, respectively. The sheet resistance of the active area under the dark condition can be calculated as:

$$R_{\text{D}} = \frac{L/W}{nq\mu}, \qquad (2)$$

where *n* is the carrier concentration in the graphene-Ta_2O_5 area. Figure 6.5a inset shows the dark current at the CNP (the minimum current of the transfer characteristic curves) as a function of the gap, *L*, for *W*/*L* = 2. With V_{SD} = 0.5 V, the total resistance under dark conditions, R_{D}, is ~2.7 kΩ. The dark resistance value is close with other reports[145, 148, 152]. When the device is illuminated, a number of carriers are generated from the N-Ta_2O_5 light-absorbing layer and transferred to the electrodes. Δn is the carrier concentration variation in the active area of the device. The photocurrent for low illumination power is solved as[172]:

$$I_{\text{ph}} = \frac{V_{\text{SD}}}{R_0 + \frac{W/L}{(n+\Delta n)e\mu}} - \frac{V_{\text{SD}}}{R_0 + \frac{W/L}{ne\mu}} \approx \frac{V_{\text{SD}}\Delta ne\mu}{(R_0 ne\mu(W/L)+1)^2}(W/L) \qquad (3)$$

Fixing the ratio of the width and the gap (*W*/*L*), the photocurrent, I_{ph}, is proportional to the carrier concentration variation, Δ*n*. Thus, to increase the photo-responsivity of the detector, reducing the active area will enhance the carrier concentration variation, Δ*n*. Figure 6.5a shows that for a fixed *W*/*L* ratio, the photo-responsivity increases several orders of magnitude from *W*/*L* = 400 μm/ 200 μm to the *W*/*L* = 20 μm/ 10 μm. When the active area was reduced with a fixed *W*/*L* ratio, the length, *L*, also was reduced. With a shorter gap between source and drain, the dark current increases significantly (Fig. 6.5a, inset), reducing the performance of the device. The smaller active area provides a high photo-responsivity, however, the dark-current, I_{D}, as well as the photo-current, I_{ph}, vary with the width, *W*, of the active area[172]. For a fixed gap between source and drain, *L*, the dark current (inset of Fig. 6.5b) as well as the photocurrent increase when the width, *W*, increases. To optimize the performance, characterization of the photo-responsivity was performed with different *W*/*L* ratio for L = 10 μm, i.e., *W*/*L* = 10 μm/ 10 μm, *W*/*L* = 20 μm/ 10 μm, *W*/*L* = 30 μm/ 10 μm, *W*/*L* = 40 μm/ 10 μm (Fig. 6.5b).

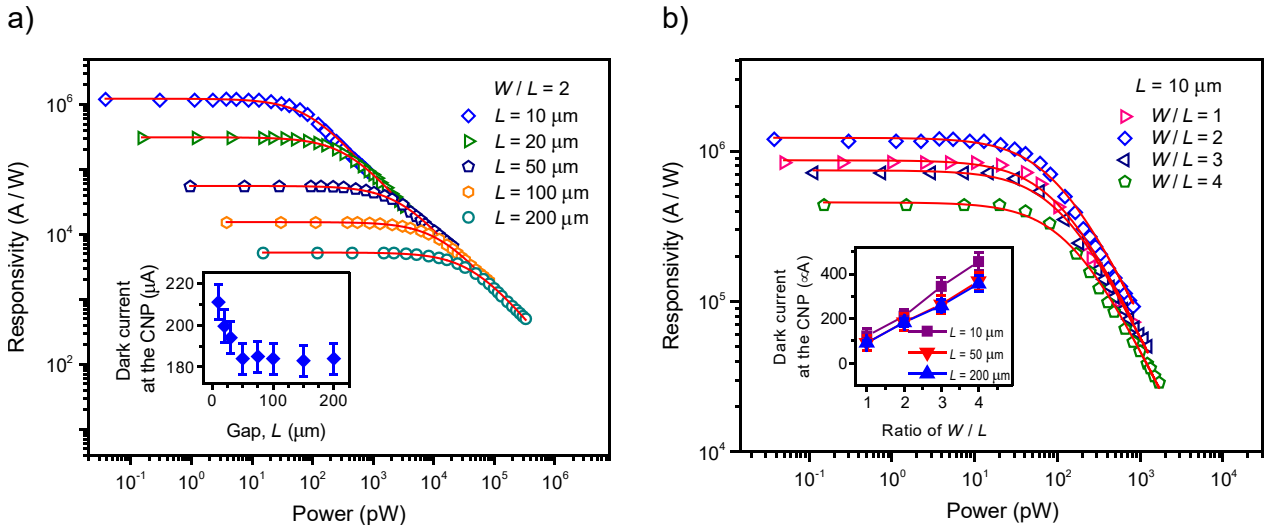

Figure 6.5: *The measured photo-responsivity for graphene-Ta_2O_5 photodetectors with different graphene sheet dimensions.* ***(a)*** *The measured photo-responsivity of photodetectors for the ratio W/L = 2 with different gaps, L, between source and drain as a function of illumination power. The solid curves are the best fit to the data using the function in Eq. 1. Inset: the dark current at the charge neutrality point as a function of gap, L, between source and drain. The dark current increases significantly when the gap becomes narrower.* ***(b)*** *The measured photo-responsivity for L = 10 μm with different ratios W/L as a function of illumination power. Inset: the dark current at the charge neutrality point as a function of the ratio of W/L.*

The highest photo-responsivity was obtained for the *W/L* = 20 μm/ 10 μm device. With increasing the width, a higher photo-responsivity is obtained. However, increasing the width beyond 20 μm decreases the photo-responsivity. The decreasing photo-responsivity with a width larger than 20 μm is a result of the recombination of carriers at defects on the monolayer graphene. The monolayer graphene was grown on copper foil by the CVD method and the monolayer graphene consists of single-crystalline grains with sizes from 10 to 20 μm[173]. Carriers produced by photon absorption strongly recombine at defects or grain boundaries. Thus, when the width increases, the photocurrent and the photo-responsivity were slowly increased. For the best performance, the optimal parameters are *L* = 10 um and *W* = 20 um. With this structure, the photodetector can detect the light intensity as low as 27 fW (0.135 mW/m^2) in the visible region.

6.3.3 Ultra-fast response time

To define the impact of a photodetector on the performance and speed, the response time has been characterized. Response time was measured using a low noise current amplifier (DLPCA-200, FEMTO) and an oscilloscope to monitor the temporal dynamics of the photocurrent under different illumination power. To obtain the ultra-fast response, an Acousto-Optic Modulators (AOM) using a TeO_2 crystal produced ultrafast laser pulses from a continuous-wave laser. Using this system, laser pulses were generated with the rise time of 20 ns.

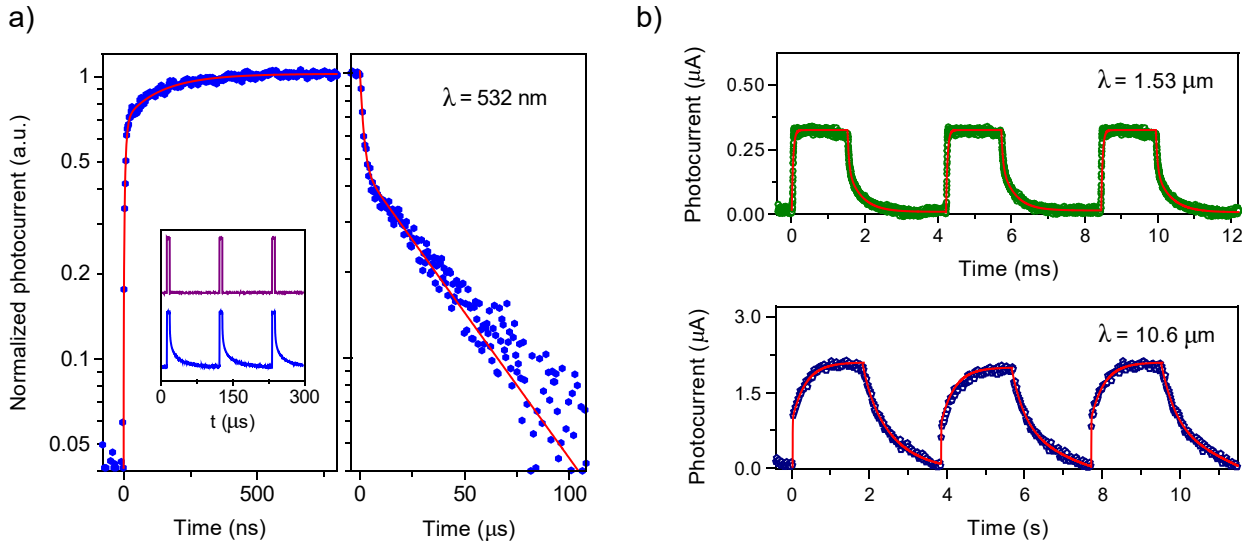

Figure 6.6: *Photocurrent response of a graphene-Ta_2O_5 photodetector to on/off illumination. (**a**) The transient photo-response of the device for an illumination at wavelength of 532 nm with V_{SD} = 0.5 V; V_{BG} = -7 V. The photocurrent response shows fast response and recovery time. The red curves are the best fitting for the data with a bi-exponential function (left panel), and bi-exponential decay function (right panel). (**b**) The photocurrent response of the device for different illumination at wavelength of 1.53 μm (top panel), and at wavelength of 10.6 μm (bottom panel).*

The photocurrent appears periodically (Fig. 6.6a, inset) with the pulse duration of 6.3 μs under the 532-nm laser illumination, V_{SD} = 0.5 V, and V_{BG} = -7 V at room temperature. For the device with an active area of 20 × 10 μm, the response time is estimated to be ~125 ns (from 10 to 90% of the peak photocurrent), while the recovery time is 41 μs (from 90 to 10% of the peak photocurrent). The signal in Fig. 6.6b shows an ultrafast response time. The increasing of photocurrent with the illumination time can be fitted to an exponential function with two time constants: $I_{ph} = I_1(1 - \exp(-t/\tau_1)) + I_2(1 - \exp(-t/\tau_2))$, in which τ_1 is ~20 ns (the rise time

of the AOM system), and τ_2 is 325 ns. The short rise time, τ_1, represents the hole transfer time to electrodes, whereas the longer time constant, τ_2, corresponds to the hole transfer time from an accepter center to graphene. Similarly, the decreasing of photocurrent with time when the light is turned off can be fitted to an exponential function: $I_{ph} = I_1(\exp(-t/\tau_3)) + I_2(\exp(-t/\tau_4))$ with two decay time constants, τ_3 = 500 ns, and τ_4 = 45 μs. The short decay time constant, τ_3, can be attributed to the charge transfer between accepter centers in the N-Ta_2O_5 layer because it is similar to τ_2. The slowest time τ_4 may represent the lifetime of ionized acceptor centers. Using the e-beam evaporation to make the nanometer N-Ta_2O_5 light-absorbing layer, fast dynamics, including the response and the recovery time of the photocurrent has been obtained. These values are orders of magnitude faster than those from previous reports[146, 148, 150, 151, 152, 154, 172]. Thus, extra reset gate-voltage pulses are not required for fast switching performance of these devices.

6.3.4 Ultra-broadband Photodetection from deep-UV upto Mid-IR region

To characterize the broadband photo-response of the devices, photo-responsivity as a function of illuminated photon energy was measured. The photo-responsivity shows a broadband spectrum from the MIR to deep-UV region (Fig. 6.7a). Specifically, the photo-responsivity at the MIR region (10.6 μm or 0.12 eV) is 7.2 A/W, and is significantly sensitive in the range from the near infrared (1.53 μm or 0.81 eV) to the deep-UV (200 nm or 6.2 eV) region on the order of 10^6 A/W. The light sources used include a CO_2 laser operating at 10.6 μm, a quantum cascade laser lasing at 4.55 μm, a fiber laser lasing at 1.53 μm, a diode-pumped laser operating at 532 nm, and monochromatic light extracted from a broadband light source. The light source is expanded to a large beam and a pinhole has been used to calibrate the photon flux. The spectral photo-responsivity of the device containing 5-nm N-Ta_2O_5 layer shows an onset at ~ 1 eV.

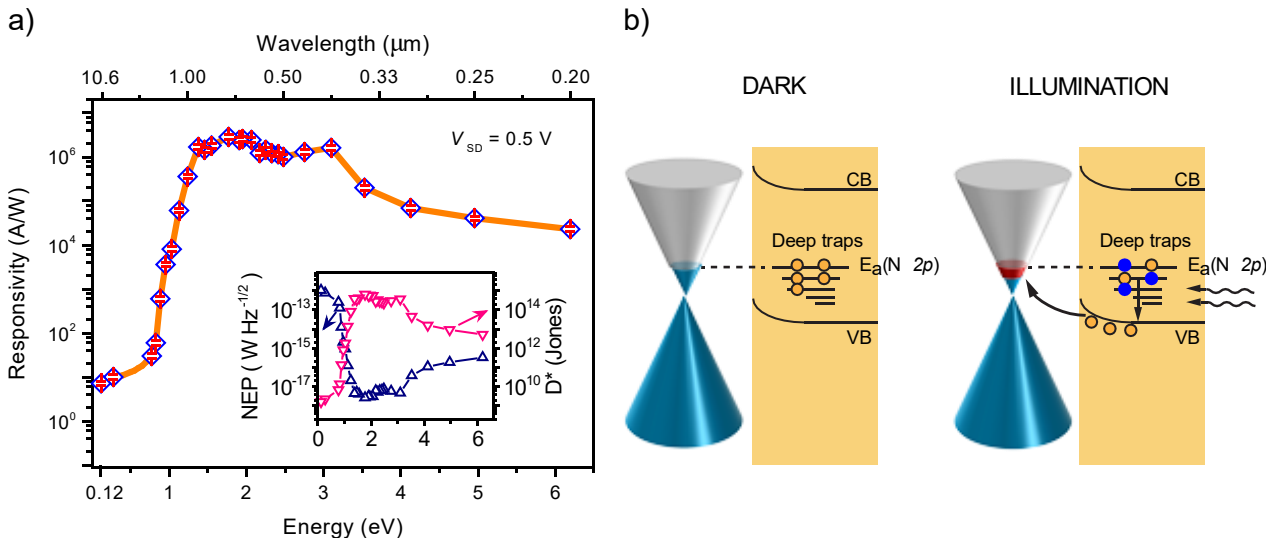

Figure 6.7: *Spectral sensitivity and detectivity of the graphene-Ta_2O_5 heterostructure device ($W \times L$ = 20×10 μm). (**a**) Photo-responsivity of the device as a function of excitation photo-wavelength from 200 nm to 10.6 μm (or from 0.12 to 6.2 eV). The blue diamonds are experimental data, and the orange line is a guide to eyes. Inset: Spectral dependence of the NEP and specific detectivity (D*) of the photodetector device at room temperature, V_{BG} = 0 V, and V_{SD} = 0.5 V. (**b**) Schematic diagram of energy band structures of graphene and the 5-nm N-Ta_2O_5 layers together with the tendency of charge transfer between layers. The blue dots present for the ionized acceptor centers, while hollow dots stand for holes.*

6.3.5 Photoconductive gain induced by N-doped Ta_2O_5

Nitrogen incorporation into oxides is widely reported in the literature, and N-doped Ta_2O_5 exhibited a dual functional modulation including band gap narrowing and p-type conduction[167, 168, 169, 170]. A number of studies including absorption experiments and X-ray photoelectron spectroscopy[167, 170, 174], ultraviolet photoelectron spectroscopy and electrochemical techniques[175], time-resolved spectroscopic studies[169], and density-functional theory calculations[168] have shown that Ta_2O_5 phase changes to p-type in the nitrogen doped Ta_2O_5 material. Nitrogen doping in Ta_2O_5 increases the number of defect states and produces multiple levels above the valence band (VB) of ~1.25 eV from the N 2p orbital, and the oxygen sites were substituted by nitrogen[169, 176]. The N 2p states form a band above the VB, resulting in band gap narrowing and p-type conduction. Photons with energy higher than the acceptor energy ionize the accepter centers, resulting in hole

generation. Holes transfer from the N-Ta_2O_5 to graphene, leaving behind negative charges (ionized acceptor centers). In addition, the N-Ta_2O_5 thin layer has the amorphous phase, the N 2p states create a broad band with the maximum of photon-ionization cross section at ~1 eV above the VB. The spectral photo-responsivity from the graphene-Ta_2O_5 heterostructure showed a maximum at ~1 eV and a long tail extending to the MIR (Fig. 6.7a). Figure 6.7b demonstrates a schematic diagram of the energy band structures of graphene and N-Ta_2O_5 layers and the tendency of charge transfer between layers. The blue dots present for the ionized acceptor centers, while hollow dots stand for holes.

The response time of the devices in the MIR is slower compared with those from the VIS to NIR region. The response time at 10.6 μm shows two components. The fast component is faster than 1 ms (limitation of the test system), and the longer component is 300 ms. The fast component originates from the transit time of holes in the graphene channel, while the longer comes from the lifetime of surface trapping center.

6.3.6 Detector figures-of-merit

6.3.6.1 Noise characterization

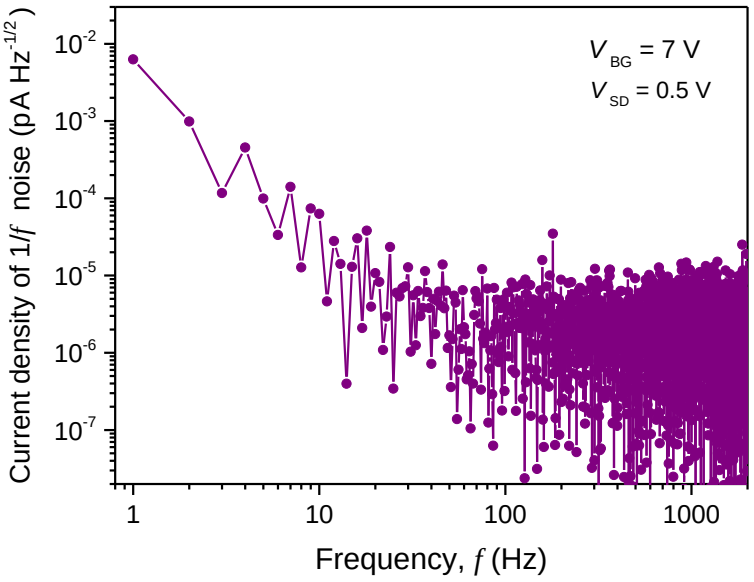

Figure 6.8: *The current density of* $1/f$ *noise for the graphene-Ta_2O_5 photodetector with W/L = 20 μm / 10 μm at V_{BG} = 0 V and V_{DS} = 0.5 V, at a modulation frequency of 1 Hz.*

For practical applications, the noise-equivalent-power (NEP) as well as the specific detectivity (D*) are important parameters of a photodetector, which are expressed as

$$D^* = \frac{\sqrt{A \times \Delta f}}{NEP} \quad (1)$$

where Δf is the bandwidth in hertz, and A is the area of the device in cm^2. The NEP can be evaluated by considering the spectral density of $1/f$ noise, shot noise, and thermal noise of graphene-Ta_2O_5 photodetectors.

The noise current density of $1/f$ noise is calculated by analyzing the noise in the dark current waveform for the graphene-Ta_2O_5 photodetector with W/L = 20 μm / 10 μm. The dark current waveform was acquired by a current preamplifier with a sampling rate of 1 Hz at V_{BG} = 7 V and V_{DS} = 0.5 V. The noise current density is given by

$$S_I(1/f) = \frac{1}{\sqrt{F_s N}} \sqrt{\langle |I(f)|^2 \rangle} \quad (2)$$

where $I(f)$ denotes the discrete Fourier transform of the dark current waveform $I(t)$, F_s is the sampling rate of 10,000 Hz, N is the number of data points of 10,000 points.[67] The spectral density of $1/f$ noise calculated from dark current waveform is plotted in Figure 6.8. The NEP value of the spectral density of $1/f$ noise is ~ 0.0063 pA/$\sqrt{Hz}$ with V_{SD} = 0.5 V and V_{BG} = 7 V, at a modulation frequency of 1 Hz.

The shot noise is estimated by using:

$$S_I(\text{shot}) = \sqrt{2qI_{dark}} \quad (3)$$

where q is the elemental charge, and I_{dark} is the dark current of the device.[67] Figure 6.9 shows the dark current, I_{dark}, at the charge neutrality point as a function of back gate voltage. The calculated spectral density of shot noise is ~ 7.64 (pA/$\sqrt{Hz}$).

The thermal noise is calculated by using Nyquist's equation:

$$S_I(\text{thermal}) = \sqrt{4k_B T/R} \quad (4)$$

where k_B is the Boltzmann's constant, T is the temperature, and R is the differential resistance of the device in the dark. The thermal noise at room temperature is estimated ~ 0.17 (pA/$\sqrt{Hz}$). The

spectral density of 1/f noise, shot noise and thermal noise limit of the graphene-Ta_2O_5 photodetector as a function of source-drain voltage have been presented in Figure 6.10.

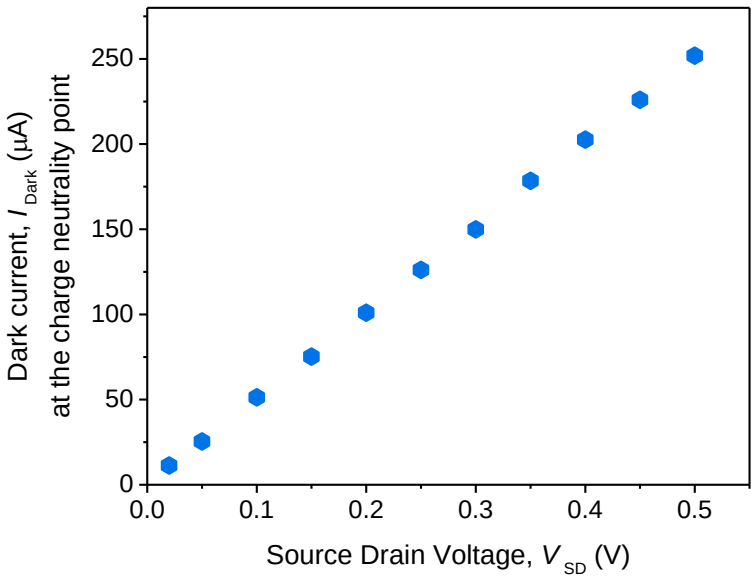

Figure 6.9: *Dark current, I_{dark}, at the charge neutrality point as a function of back gate voltage.*

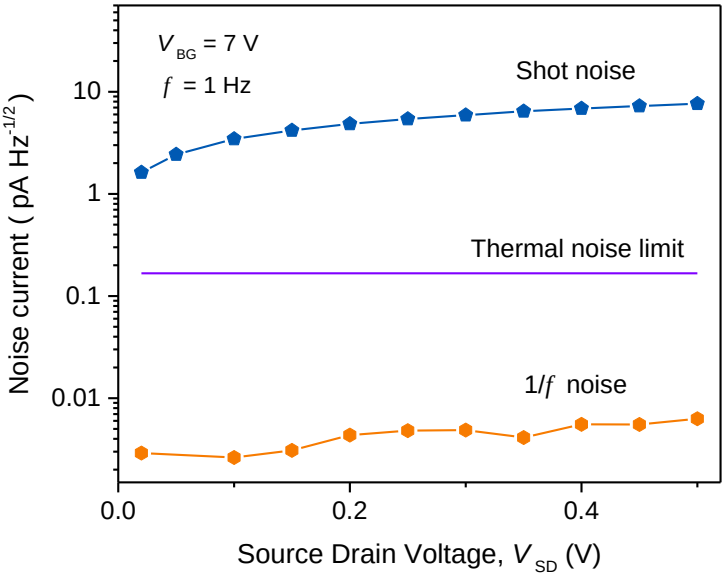

Figure 6.10: *Noise current densities of 1/f noise, shot noise, and thermal noise of graphene-Ta_2O_5 photodetectors as a function of source-drain voltage, V_{SD}.*

6.3.6.2 Detector figures-of-merit: NEP and Specific Detectivity

To evaluate the capability of weak light detection of a photodetector, two key metrics including the specific detectivity (D^*) and the noise equivalent power (NEP) have been examined by considering the shot noise, thermal noise and 1/f noise.

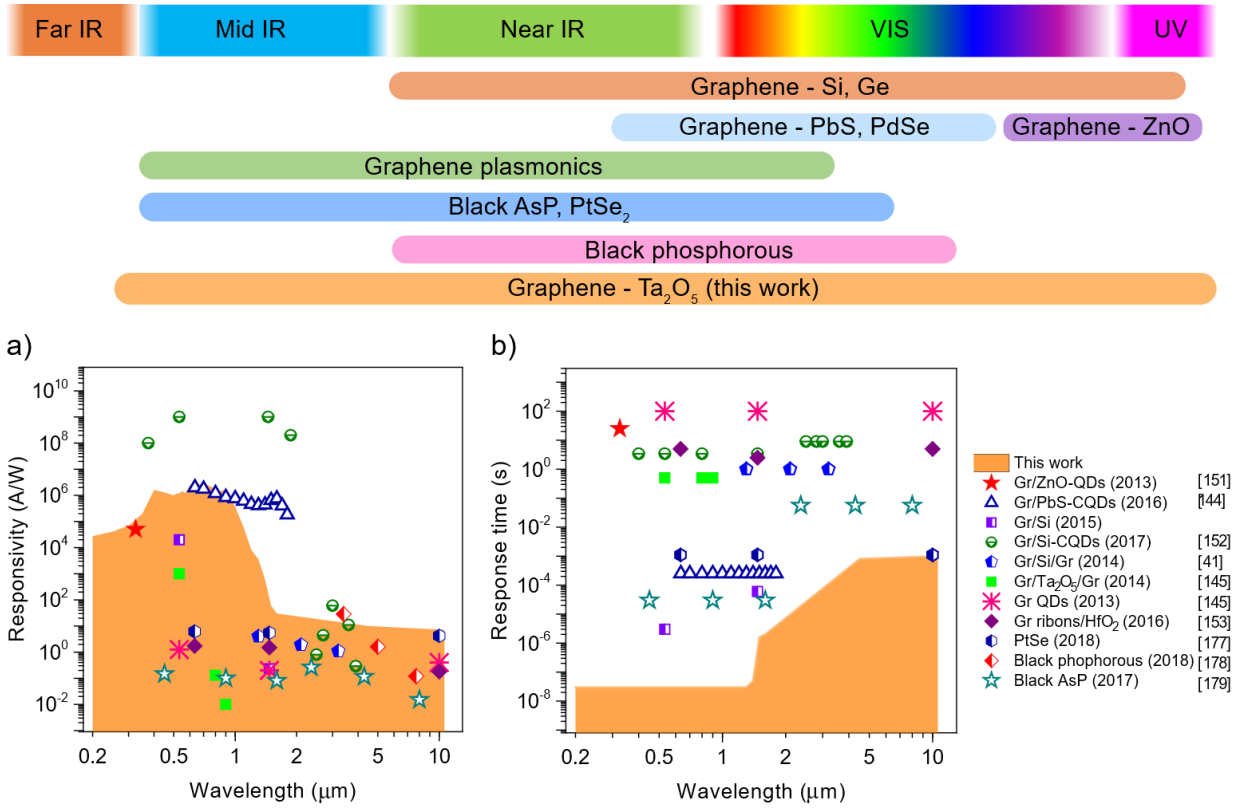

Figure 6.11: *Comparison photodetectors operated at different wavelength based on 2D materials including graphene, $PtSe_2$, black phosphorous. Comparison the current results with those reported in literature for the (a) photo-responsivity (b) response time.*

A detail of the calculations for these noises is presented in the Supporting Information. The frequency-dependence of the noise current for the photodetector at room temperature was measured under V_{SD} = 0.5 V and V_{BG} = 7 V at the modulation frequency of 1 Hz. The NEP values ($\text{NEP} = \sqrt{S_I(\text{shot})^2 + S_I(\text{thermal})^2 + S_I(1/f)^2}/R$) are achieved as low as 2.7×10^{-18} and 1.1×10^{-12} (W/Hz$^{-1/2}$) in the UV-to-NIR region and the MIR region, respectively (Fig. 6.7a, inset). This yields specific detectivity values, $D^* = \sqrt{A}/\text{NEP}$, ($A$ is the area of the detector) in the order of 6.5×10^{14} and 1.7×10^9 (Jones) for the UV-to-NIR and MIR regions, respectively (Fig. 6.7a, inset). The small values of NEP, or large values of D^* indicate that graphene-Ta_2O_5 heterostructure

photodetectors can be well used for weak light detection from deep-UV to MIR region. Photo-conductivity and response time for photodetectors based on 2D materials including graphene, graphene quantum dots[177], graphene nanoribbons[178], $PtSe_2$[179], black phosphorous[180], black arsenic phosphorus[181] are shown in Fig. 6.11. The photo-responsivity of the graphene-Ta_2O_5 heterostructure is similar with the graphene-CQD photodetectors, but the response time is orders of magnitude faster than other photodetectors based on 2D-materials. Thus, the graphene-Ta_2O_5 heterostructure photodetector can operate without any extra reset voltage pulse applied to the back-gate.

6.4 Conclusions

In summary, we have fabricated and demonstrated graphene-Ta_2O_5 heterostructure photodetectors with improved responsivity and ultrafast response speed. The structure extends the photo-detection of graphene hybrid phototransistors from UV-VIS region into the MIR region. The current work has established the development of high-performance optoelectronic devices based 2D materials, demonstrating for the first time the added value provided by merging of these two important materials – graphene for optoelectronic and Ta_2O_5 for microelectronics, photonics and solar energy applications.

Summary

To realize the coherent light sources integrable on the Si-CMOS technology, we investigated the optical properties and the amplified spontaneous emission of the Er-doped GaN epilayers and the Er-doped GaN multiple quantum wells (MQWs).

First, we have investigated the optical activity, the PL quantum efficiency and the non-radiative transfer energy pathways between the Er ions and the GaN host from the GaN:Er epilayers prepared by using the MOCVD method. The PL intensity measurements under the resonant excitation (λ = 809 nm) indicate the low thermal quenching of 20% from 10 K to room temperature from the Er^{3+} ions in our GaN:Er epilayer. We also have identified the non-radiative channels in this material using the temperature dependence measurements of the PL intensity. The findings provide useful insights for further improvement of the 1.54 μm emission in material engineering towards optimizing the energy transfer between the GaN host and the Er ions. By comparing the PL intensity from the GaN epilayers with that of the SiO_2:Er reference sample under the resonant excitation (λ = 809 nm), we estimated that the percentage of the isolated Er optical centers in the GaN epilayers is about 68%. The high percentage of the optically active centers in GaN epilayers indicates the high potential for realizing optical amplification.

Next, we have investigated the amplified spontaneous emission of the Er optical centers in the GaN epilayers prepared by the MOCVD method under the resonant excitation (λ = 809 nm). Using the variable stripe technique, the observation of the stimulated emission at 1.5 μm at room temperature is accompanied by characteristic features of threshold behavior of emission intensity as functions of pump intensity, excitation length, and spectral linewidth narrowing. The optical gain has been obtained in the GaN:Er epilayers, up to 75 cm^{-1}.

Furthermore, to enhance the simulated emission from Er^{3+}, we employed the quantum confinement effect in the Er-doped GaN MQWs. The emission intensity from the MQWs:Er structure with the optimum GaN well thickness of 2 nm and the barrier thickness of 10 nm is higher than that of the GaN:Er epilayer under the over-bandgap excitation, λ_{exc} = 351 nm, about an order

of magnitude. Besides, we estimated the percentage of the isolated Er^{3+} optically active centers in the GaN MQWs is approximately 65%. This is a crucially important parameter for realizing the stimulated emission in the GaN:Er MQWs samples.

We reported the realization of room-temperature stimulated emission in the technologically crucial 1.5 μm wavelength range from Er-doped GaN MQWs on silicon and sapphire. Employing the well-acknowledged variable stripe technique, we have demonstrated the optical gain up to 170 cm^{-1} in the multiple-quantum well structures. In the past, this formidable goal was unsuccessfully attempted by Er doping of crystalline Si, and later of SiO_2 sensitized with Si nanocrystals. The realization of this long-sought goal of Si photonics in state-of-the-art GaN multiple-quantum well structures grown on-Si and GaN is demonstrated for the first time the added value provided by merging of these two most important semiconductor materials – Si for standard electronics and photovoltaics and GaN for power electronics, photonics and automotive applications.

Finally, to address the infrared photodetection, we have fabricated and characterized the graphene-Ta_2O_5 heterostructure photodetectors with improved responsivity and ultrafast response speed. The structure extends the photo-detection of the graphene hybrid phototransistors from the UV-VIS region into the MIR region. Our hybrid photodetectors operated from the deep-ultraviolet to the mid-infrared region with high sensitivity and ultrafast response by coupling graphene with a p-type semiconductor photosensitizer, nitrogen-doped Ta_2O_5 thin film (5 nm) grown by e-beam evaporation. The high photo-responsivity (up to 3.0×10^6 A/W), the ultrafast response time (faster than 20 ns) and the specific detectivity (up to $\sim 6.5 \times 10^{14}$ Jones) were achieved at room temperature. The current work has established the development of high-performance optoelectronic devices based 2D materials, demonstrating for the first time the added value provided by merging of these two important materials – graphene for optoelectronic and Ta_2O_5 for microelectronics, photonics and solar energy applications.

Appendix A

Monte Carlo Ray-Trace Diffraction Based on the Huygens-Fresnel Principle

This chapter was adapted with only minor changes from the manuscript:
"Reprinted with permission from J. R. Mahan, N. Q. Vinh, V. X. Ho, and N. B. Munir, "Monte Carlo ray-trace diffraction based on the Huygens–Fresnel principle," Appl. Opt. 57, D56-D62 (2018).

The goal of this effort is to establish the conditions and limits under which the Huygens-Fresnel principle accurately describes diffraction in the Monte Carlo ray-trace environment. This goal is achieved by systematic intercomparing of dedicated experimental, theoretical, and numerical results. We evaluate the success of the Huygens-Fresnel principle by predicting and carefully measuring the diffraction fringes produced by both single slit and circular apertures. We then compare the results from the analytical and numerical approaches with each other and with dedicated experimental results. We conclude that use of the MCRT method to accurately describe diffraction requires that careful attention be paid to the interplay among the number of aperture points, the number of rays traced per aperture point, and the number of bins on the screen. This conclusion is supported by standard statistical analysis, including the adjusted coefficient of determination, R_{adj}^2 , the root-mean-square deviation, RMSD, and the reduced chi-square statistics, χ_v^2.

A.1 Introduction

The Monte Carlo ray-trace (MCRT) method has long been utilized to model the performance of optical systems in the absence of diffraction and polarization effects.[182, 183, 184, 185, 186, 187, 188, 189, 190, 191] Heinisch and Chou,[192] and later Likeness,[190] were among the early proponents of treating diffraction in the MCRT environment. However, their approach, which is based on a geometrical interpretation of the Heisenberg uncertainty principle, relies on empiricism to obtain adequate agreement with theory.[193, 194] More recently the Huygens-Fresnel principle[195] has been implemented to describe diffraction and refraction effects in the MCRT [196, 197, 198, 199] and wave-front tracing [191] environments. The goal of the current effort is to establish the conditions and limits under which the Huygens-Fresnel principle accurately describes diffraction in the MCRT environment. The method can be applied in the whole range of electromagnetic wave including the infrared region. This goal is achieved by systematic inter-comparison of dedicated experimental, theoretical, and numerical results supported by statistical analysis.

A.2 Approach

We evaluate the success of the Huygens-Fresnel principle in describing diffraction in the MCRT environment by comparing predicted diffraction fringes with experimentally observed fringes produced for various aperture-to-screen distances, for both single slits and circular apertures. Predictions are based on an analytical approach widely available in the literature, and on the MCRT method described here. We compare the results from the analytical and numerical approaches with each other and with the dedicated experimental results. Standard statistical analysis is used to characterize differences observed among the theoretical, numerical, and the experimental results.

A.3 Experimental apparatus and procedure

Figure A.1 is a schematic diagram of the apparatus used to obtain the experimental results reported here. A 351-nm laser beam produced by a Coherent Enterprise II 653 Argon Laser System is steered through mirrors to a chopper. The chopper is used to modulate the intensity of the laser beam. After that it passes through a beam expander and a 4-by-4 mm beam former before falling on the aperture. The beam expander consists of two convex lenses whose focal lengths are 3.5 and 15 cm. The relatively large dimensions of the beam former ensure that the center of the beam does

not contain a significant amount of diffracted light. The aperture consists of either a precision slit or a circular hole. The diffracted beam is incident to a 2.0-μm pinhole mounted on the entrance aperture of a Newport 918-UV photodetector. This pinhole determines the spatial resolution of the fringe measurements. Low-noise operation is assured by passing the detector output successively through a preamplifier and a lock-in amplifier. The lock-in amplifier is used to improve the signal-to-noise ratio of the setup. The shape and size of apertures and the aperture-to-pinhole spacing, z, are parameters of the study.

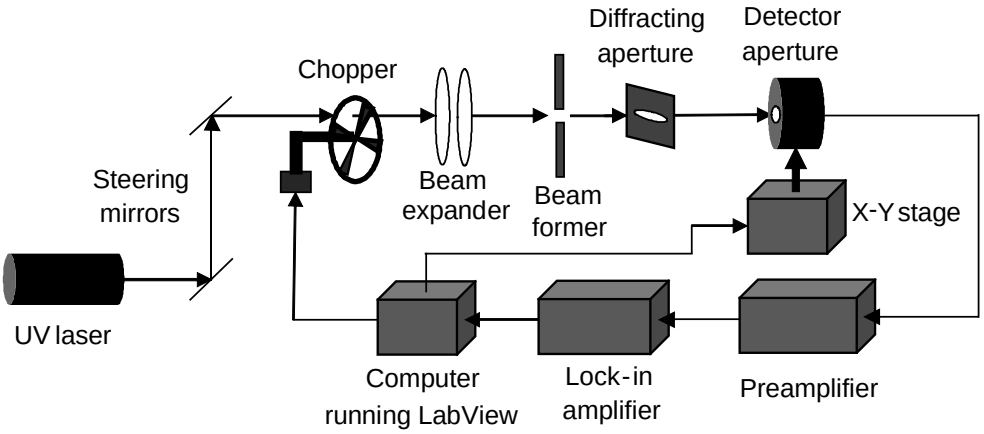

Figure A.1 *Schematic diagram of the experimental apparatus.*

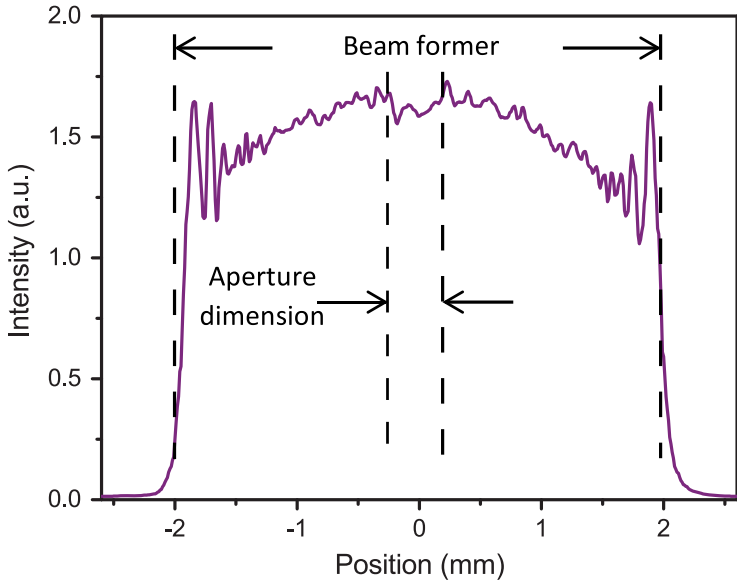

Figure A.2: *Scan across the expanded and formed laser beam cross-section between the beam former and the aperture.*

Figure A.2 shows an intensity profile, in arbitrary units, across the center of the expanded and formed laser beam cross-section immediately in front of the aperture. The vertical dashed lines indicate the maximum width of slits and apertures used. The intensity of the laser beam shows an accuracy of better than 2.5%. This image shows that the beam profile incident to the aperture is essentially flat to within the inherent noise level. The diffraction effects clearly visible at the edges of the beam former do not persist to the center of the beam.

A.4 Analytical description of diffraction

The diffraction irradiation pattern depends on the distance from an aperture to the observation screen. When the distance between the aperture and the observation is smaller than a wavelength, which is the near-field sub-wavelength region, the irradiation pattern has a shape similar to that of the aperture. When the irradiance pattern observed at a very great distance from the aperture ($z > a^2/\lambda$ where a is the size of the aperture and λ is the wavelength), we obtain the far-field pattern typical of Fraunhofer diffraction. The region in between the near-field sub-wavelength region and the far-field region is the Fresnel regime, or the near-field Fresnel region. We employ here an analytical description of diffraction for near-field Fresnel and the Fraunhofer diffraction.

Diffraction is considered to be in the Fresnel regime when either the light source or the observing screen, or both, are sufficiently near the aperture that the curvature of the wavefront becomes significant. Thus, we are not dealing with plane waves. Consider an aperture at z = 0 in the x', y'-plane illuminated with a monochromatic light of wavelength λ and producing a field distribution, $E_0(x', y')$, within the aperture, as illustrated in Fig. A.3. The field for the point P in the plane of observation (x, y), parallel to the x', y'-plane but at a distance z to the right, is given by adding together spherical waves emitted from each point in the aperture,[195, 200, 201]

$$E(P) = \frac{1}{i\lambda}\iint_{\Sigma} E_0(x', y')\frac{\exp(ikr)}{r}\cos\vartheta \; dx'dy' \qquad (1)$$

In Eq. (1), ϑ is an angle between a vector perpendicular to the x,y-plane and the vector $\vec{r}$ joining P and P'; thus $\cos\vartheta = z/r$. The distance between the points P and P' is given by

$$r = \sqrt{z^2 + (x - x')^2 + (y - y')^2}$$

$$\approx z\left(1 + \frac{1}{2}\left(\frac{x-x'}{z}\right)^2 + \frac{1}{2}\left(\frac{y-y'}{z}\right)^2\right) \qquad (2)$$

Thus, we obtain the Fresnel approximation (near field),

$$E(x,y) = \frac{1}{i\lambda z}\, e^{ikz} e^{i\frac{kz}{2z}(x^2+y^2)} \times \iint_{\Sigma} E_0(x',y') e^{i\frac{k}{2z}(x'^2+y'^2)} e^{-i\frac{k}{z}(xx'+yy')}\, dx'dy' \qquad (3)$$

When both the source and the observation point are situated sufficiently far from the aperture (i.e., $z \gg k(x'^2 + y'^2)/2$), the factor $e^{i\frac{k}{2z}(x'^2+y'^2)}$ can be dropped from Eq. (3), yielding the Fraunhofer approximation (far field),

$$E(x,y) = \frac{1}{i\lambda z} e^{ikz} e^{i\frac{kz}{2z}(x^2+y^2)} \times \iint_{\Sigma} E_0(x',y')\, e^{-i\frac{k}{z}(xx'+yy')}\, dx'dy'. \qquad (4)$$

We employ the Fourier transform to find the solution for both approximations.

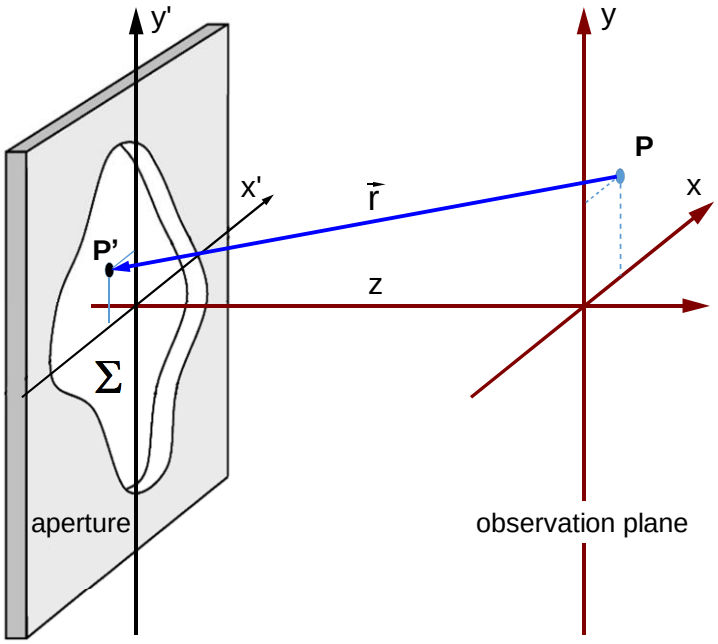

Figure A.3: *Transmission through an aperture*[195]

A.5 MCRT diffraction model

According to the Huygens-Fresnel principle, light propagates as a succession of self-replicating wavefronts. At its origin the wavefront for a plane wave is considered to consist of an array of equally spaced point disturbances, represented by the solid dots in Fig. A.4a. Each point disturbance produces an outward-propagating pattern of concentric spherical waves. Then, for a given order of each spherical wavefront (t + Δt), a tangent plane is passed parallel to the original plane wavefront, with each point of tangency now considered to be a new point disturbance. As pointed out by Volpe, Létourneau, and Zhao,[191], "the construction should be regarded as a mathematical abstraction that correctly reproduces the physics without necessarily being physically rigorous."

It is convenient to recognize the duality between rays and waves in which the former are defined such that they are mutually orthogonal with the latter at points of intersection. The ray view of the Huygens-Fresnel principle is illustrated in Fig. A.4b. In this view, each ray is considered to be an entity such as the one illustrated in Fig. A.5; that is, it originates at a specified point, travels in a specified direction, and carries an electric field whose value varies periodically with position along its length as determined by the wavelength of the light.

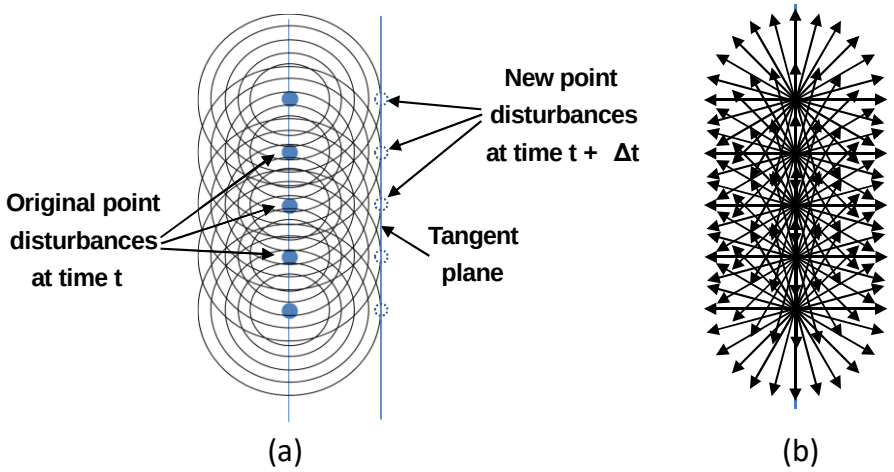

Figure A.4*(a) Wave and (b) ray views of the Huygens-Fresnel principle for a right-running wave*[195]

It is natural to identify the slit or circular aperture considered in this contribution as a plane source of rays of the type illustrated in Figs. A.4b and A.5. According to the Huygens-Fresnel principle, these rays will propagate from each source point in the slit or circular aperture with a directional distribution influenced by an obliquity factor. In the Monte Carlo ray-trace view of optics, source points randomly distributed in the plane of the slit or circular aperture emit rays with a directional distribution determined by an appropriate obliquity rule. Consistent with the assumption of a monochromatic plane wave incident on axis to the slit or aperture, all diffracted rays will be in phase.

Figure A.6 illustrates equally well the geometry for both the infinite slit and the circular aperture diffraction problems. We consider a source point P' in the plane of the slit or circular aperture and a field point P lying on the screen. Then, referring to Fig. A.6, the phase ,ϕ, of the ray when it arrives at screen point P will depend only on the wavelength λ of the light and the length of the line connecting source point P' with field point P; that is,

$$\phi = 2\pi \frac{z/\lambda}{\cos\vartheta} \qquad (5)$$

where z is the horizontal distance between the slit or aperture and the screen, and ϑ is the angle between the ray and the z-axis. The electric field strength of the ray at field point S' is then

$$E = E_0 e^{i\phi} \qquad (6)$$

Within an arbitrary constant the intensity distribution on the screen is given by

$$I(y') \propto E(y') \times E^*(y') \qquad (7)$$

where E(y') is the local electric field due to all of the rays incident to a given field point, and * denotes its complex conjugate. This calculation requires that the screen surface be divided into bins since it is unlikely that two rays will be incident at exactly the same point. Then the electric field strength in bin n is the algebraic sum of the contributions by the individual rays that are incident within the bin.

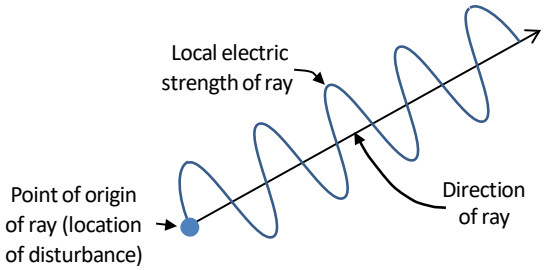

Figure A.5: *Anatomy of an individual ray*

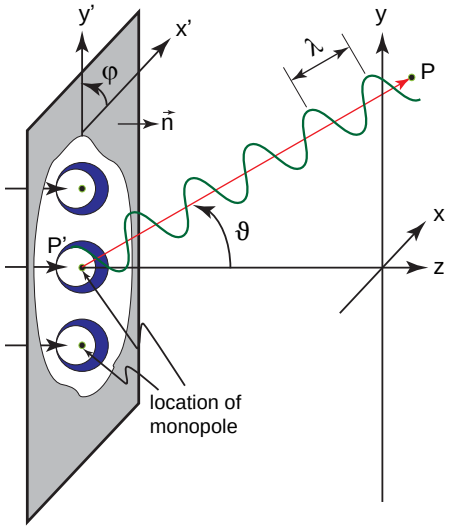

Figure A.6: *The MCRT diffraction model.*[195]

The validity of the Huygens principle illustrated in Fig. A.4 may be questioned because of the presumed monopole nature of the disturbances forming the wavefront at each time step. At any instant, every point on the primary wavefront is envisioned as a continuous emitter of spherical secondary wavelets. Each wavelet radiated uniformly in all directions, in addition to generating an ongoing wave, thus, there would be also a reverse wave traveling back toward the source. No such a wave is found experimentally. Attempts to address this inconsistency when using the Huygens principle as the basis for formulating diffraction by apertures have led to the concept of the obliquity factor. The obliquity factor attributed to Kirchhoff has the form $K(\vartheta) = (1 + \cos\vartheta)/2$ at a given angle ϑ with respect to the aperture normal **n**. Spherical secondary wavelets with weighted direction have been shown in the Figure A.6. [195] This has its maximum value, $K(0) = 1$, in the forward direction and disperses with the back wave, $K(\pi) = 0$. Obliquity factors have been used with varying degrees of success in analytical treatments of diffraction; however, their possible role in MCRT models has been largely ignored. The traditional role of the obliquity factor is to properly model the variation of amplitude with angle ϑ for each refracted wavelet.[194] Taking into account the Huygens-Fresnel principle and the obliquity factor contribution, the optical rays are randomly generated and uniformly distributed in the single slit or the circular apertures. An equivalent approach, arguably more convenient to use in the MCRT environment, is to assign the same power to all refracted wavelets but to adjust their angular density distribution to account for obliquity. The random points are uniformly distributed in the single slit. For circular apertures, random points are homogeneously distributed over a unit disk in the form

$$\vartheta = \sin^{-1}\left[\sqrt{R_\vartheta}\right] \qquad (8)$$

and

$$\varphi = 2\pi R_\varphi \qquad (9)$$

where ϑ is the zenith angle measured from the aperture surface normal, **n**, φ is the azimuth angle measured in the plane of the aperture from an arbitrary reference, and lies in the plane of the aperture surface (Fig. A.6), and R_ϑ and R_φ are random numbers whose values are uniformly distributed between zero and unity. In the MCRT view of refraction, illustrated in Figure A.6, the refraction event occurs when the rules of random points for single slit and circular apertures are applied, where the rays abruptly change directions. Following the Huygens-Fresnel principle, each ray is divided into a number of rays, called refractions per ray. The complex amplitude at the point

P in Figure A.6 is found by the superposition of waves or summing contributions from each point on the sphere of the primary wavelets.

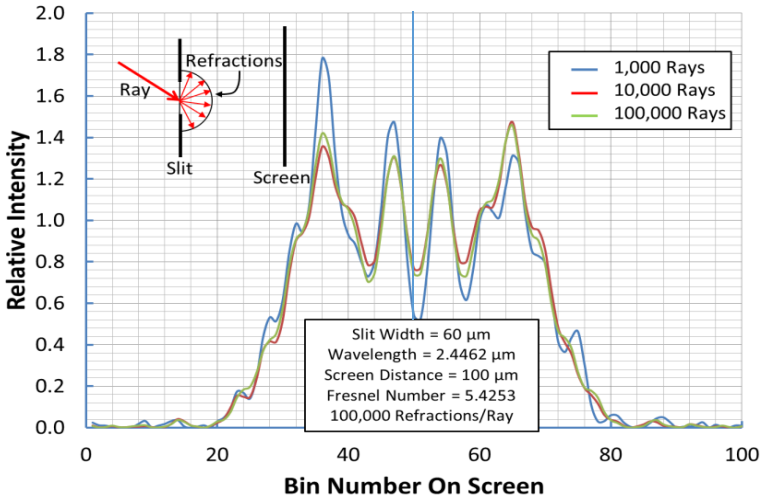

Figure A.7: *(Color online) Sensitivity of the MCRT-predicted fringe pattern to the number of rays traced.*

A.6 Results and discussion

We define the Fresnel number

$$F \equiv a\sqrt{2/\lambda z} \qquad (10)$$

where a is the slit width or aperture diameter and z is the distance from the aperture to the screen upon which fringes are formed. Two fringe patterns produced by an aperture at the same value of Fresnel number are known to be formally similar, regardless of the values of a, λ, and z. By convention, if F > 1.0, diffraction is considered to be in the Fresnel regime, and if F < 1.0 diffraction is considered to be in the Fraunhofer regime.

Figure A.7 illustrates the fringe pattern predicted using the MCRT method for the case of a 60-µm slit at a wavelength of 2.4462 µm and a screen distance of 100 µm, corresponding to a Fresnel number of 5.4253. Results are shown for three values of the number of rays traced from randomly located positions y in the slit: one thousand, ten thousand, and one hundred thousand. The results for this case, which can be considered typical, verify that convergence is assured when 100,000 refractions per ray are launched from 100,000 randomly located points in the slit. A measure of the accuracy of the results obtained can be assessed by observing the departure from symmetry of the results about the center plane located at bin number 50.

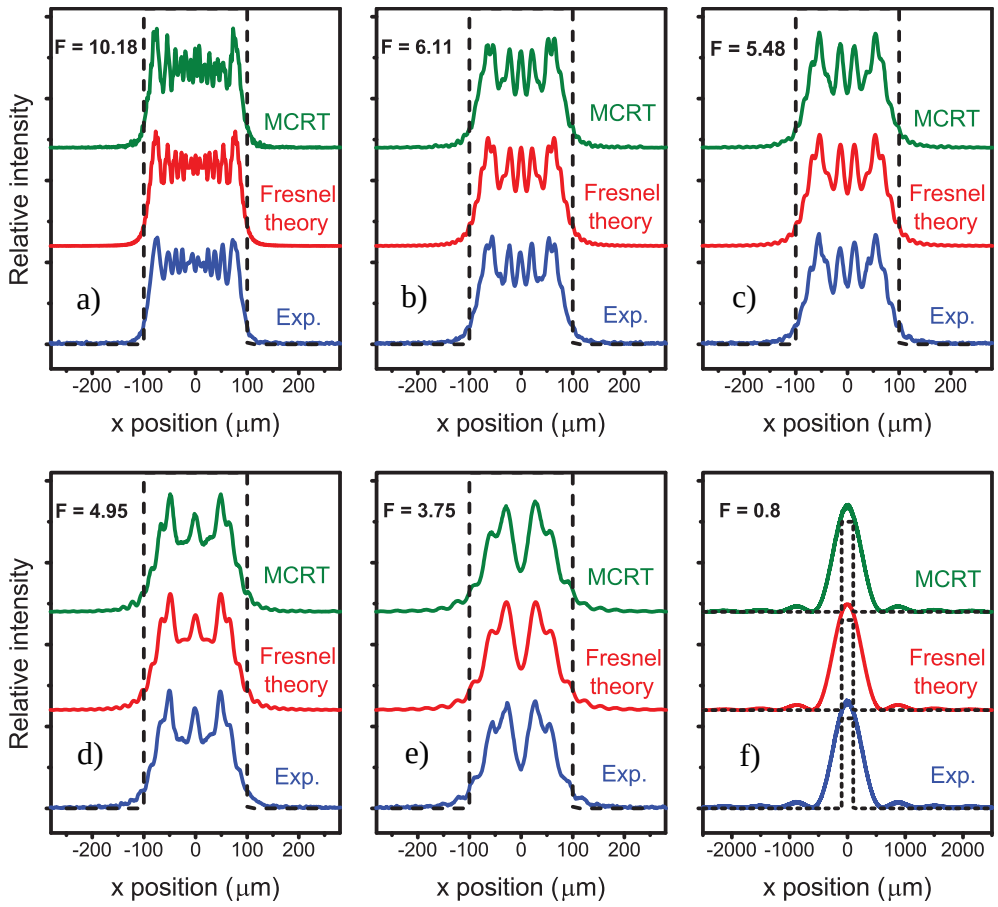

Figure A.8: *(Color online) Comparison of MCRT, theoretical, and measured diffraction fringes produced by a 200-μm slit illuminated by a 351-nm laser for a range of aperture-to-fringe distances.*

Experience has shown that the MCRT results are also sensitive to the number of bins into which the wavelets are bundled on the screen. The pinhole aperture of the detector in Fig. A.1 has a diameter of 2 μm, and the experimental results reported here are for slit widths and aperture diameters of 100 and 200 μm. Therefore, the MCRT bin size roughly corresponds to the measurement spatial resolution.

The diffraction fringe patterns vary strongly by varying the aperture-to-screen distance, z, from the near-field Fresnel region to the Fraunhofer regime. Figures A.8a through A.8f compare the diffraction fringe pattern profiles produced by a slit-type aperture for six values of Fresnel number ranging from 10.18 to 0.80. In this series of images, we vary the Fresnel number by varying the aperture-to-screen distance z for a value of slit width a = 200 μm and a fixed wavelength of λ = 351 nm. The profiles are taken at the half-length of a slit whose length is long compared to the slit

width. The blue curves (bottom) are experimental results collected from our optical setup. The red curves (middle) are calculation using the Fresnel approach for the near-field Fresnel regime and the Fraunhofer approximation for the far-field region. The green curves (top) are the MCRT results described in the previous section. For this simulation, we have used 20,000 refractions per ray that are launched from 20,000 randomly located points in the 200-μm single slit. The theoretically calculated curves from the Fresnel approach as well as the Fraunhofer approximation are remarkably similar to the observed diffraction patterns. The computation time for the MCRT method for the setup is about 3 minutes. The time for Fresnel calculation using Fourier transform is significant shorter around one minute with the same computer hardware.

The MCRT method is a numerical analysis. The advantage of the numerical method is that there is virtually no limit to solve complex problems including geometrical symmetry, but this method produces numerical errors. In the following part, we provide a comparison between the MCRT method and the analytical analysis based on Fresnel/Fraunhofer approach with experimental results. The phase, ϕ , electric field, E, as well as the intensity, I, of an optical ray at screen point P will depend on the wavelength, λ, of the light, and the length of the line connecting source point P' with field point P. Thus, we extract the phase information, electrical field and intensity of refracted optical rays that launched from randomly located points in the aperture slits using the MCRT method.

We have obtained the diffraction fringe patterns by changing the size of the single-slit aperture. Figures A.9a, A.9b, and A.9c compare the diffraction fringe pattern profiles produced by a slit-type aperture for three values of the Fresnel number ranging from 6.01 to 4.03. In this series of images, the slit width a = 100 μm and the wavelength λ = 351 nm. Comparison of Figs. A.8b with Fig. A.9a and Fig. A.8c with Fig. A.9b verifies the formal similarity of fringes corresponding to the same (approximately in these cases) value of Fresnel number. These experimental results (blue curves) are compared with MCRT (green curves) and analytical (red curves) simulations.

We have measured diffraction fringes produced by circular apertures, and these results are compared with MCRT and analytical results (Figs A.10 to A.12). The fringes in all three figures correspond to normal illumination of the aperture by an expanded 351-nm laser beam. In Fig. A.10, the aperture diameter is 100 μm with a screen distance of 1.9 mm, in Fig. A.11 the diameter is 200 μm with a screen distance of 7.6 mm, and in Fig. A.12 the diameter is 400 μm with a screen distance of 30.4 mm. The Fresnel number in all three figures is the same, F = 5.48; therefore, we

expect fringe patterns to have identical shapes even though they cover different surface areas on the screen.

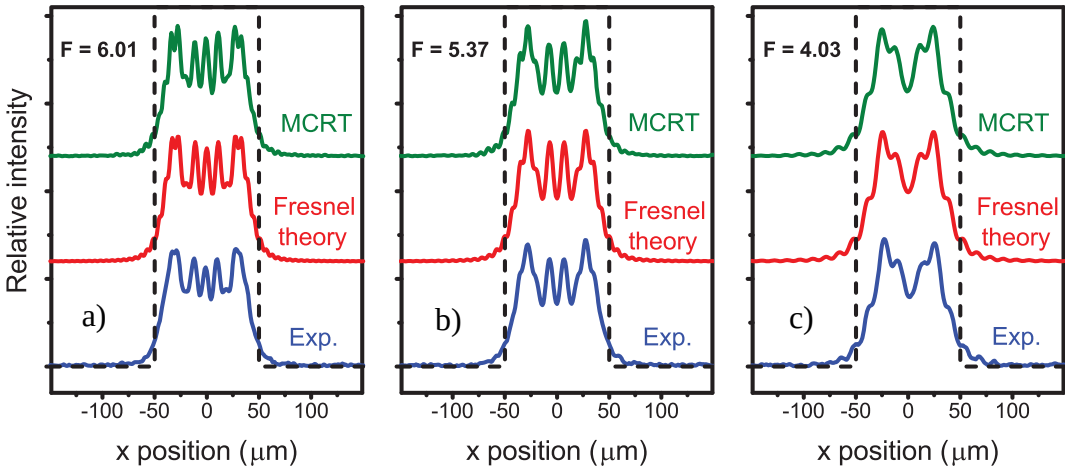

Figure A.9: *(Color online) Comparison of MCRT, theoretical, and measured diffraction fringes produced by a 100-μm slit illuminated by a 351-nm laser for a range of aperture-to-fringe distances.*

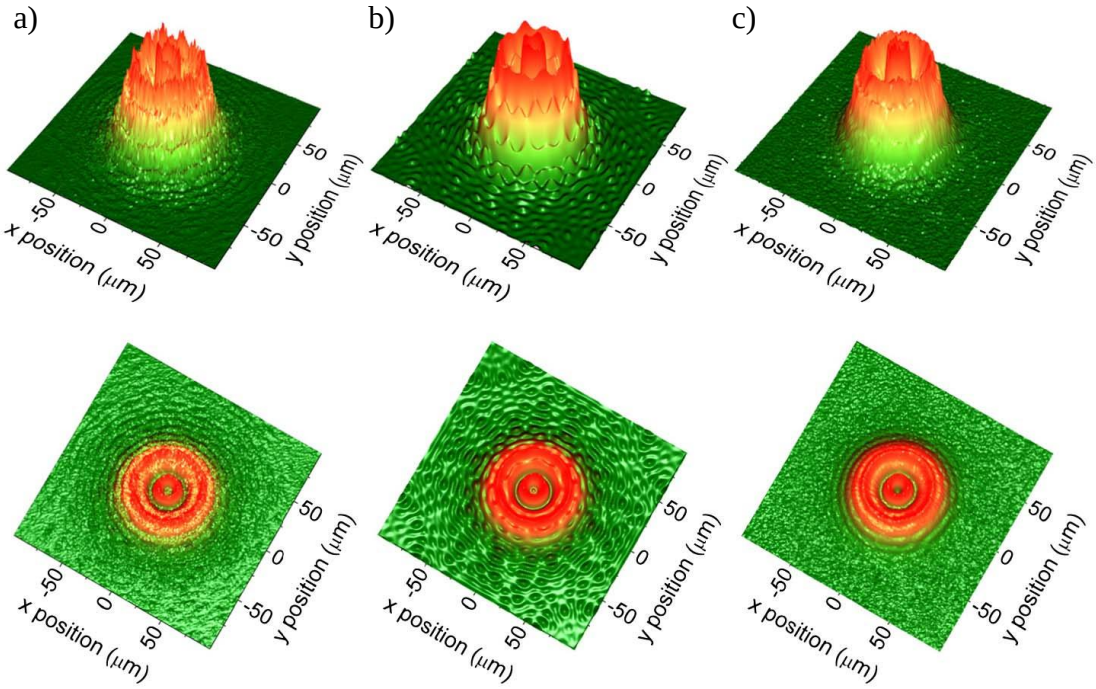

Figure A.10: *(Color online) Diffraction fringes computed (a) using the MCRT method, (b) using Fresnel theory, and (c) measured corresponding to normal illumination of a 100-μm diameter circular aperture by a 351-nm laser with a screen distance of z = 1.9 mm (F = 5.48).*

Intercomparing of the three figures reveals that the diffraction fringes are indeed formally similar even though the surface area they cover on the screen increases with increasing screen distance z, as expected. As a consequence of increasing surface area with increasing screen distance, the spatial resolution of the measured fringes increases going from Fig. A.10 to Fig. A.12. However, the sampling of the MCRT-based images decreases as a fixed number of rays traced is spread over a larger screen area. This leads to an increasing "fuzziness" of the MCRT-based images moving from Fig. A.10 to Fig. A.12. All three figures exhibit excellent agreement among the MCRT-based, analytical, and measured images.

Table A.1: *Summary of a comparison between MCRT simulation and Fresnel/Fraunhofer approach with experimental results.*

	Model	$\boldsymbol{R^2_{adj}}$	*RMSD*	$\boldsymbol{\chi^2_v}$
Single slit (200 μm)				
F = 0.80	MCRT	0.99820	4.09×10^{-4}	1.28
	Fraunhofer approximation	0.99756	4.79×10^{-4}	1.54
F = 3.75	MCRT	0.99611	2.51×10^{-4}	0.48
	Fresnel theory	0.98654	4.39×10^{-4}	0.36
F = 4.95	MCRT	0.99531	3.01×10^{-4}	0.46
	Fresnel theory	0.99439	3.29×10^{-4}	0.43
F = 5.48	MCRT	0.99278	3.66×10^{-4}	1.88
	Fresnel theory	0.99017	4.24×10^{-4}	0.68
F = 6.11	MCRT	0.99019	4.29×10^{-4}	1.91
	Fresnel theory	0.98680	4.97×10^{-4}	0.91
F = 10.18	MCRT	0.97186	7.72×10^{-4}	1.96
	Fresnel theory	0.98230	6.15×10^{-4}	1.34
Single slit (100 μm)				
F = 4.03	MCRT	0.98549	4.28×10^{-4}	0.62
	Fresnel theory	0.99224	3.13×10^{-4}	0.43
F = 5.37	MCRT	0.99472	2.56×10^{-4}	1.05
	Fresnel theory	0.99517	2.45×10^{-4}	0.81
F = 6.01	MCRT	0.98708	4.09×10^{-4}	1.62
	Fresnel theory	0.98703	4.09×10^{-4}	0.89

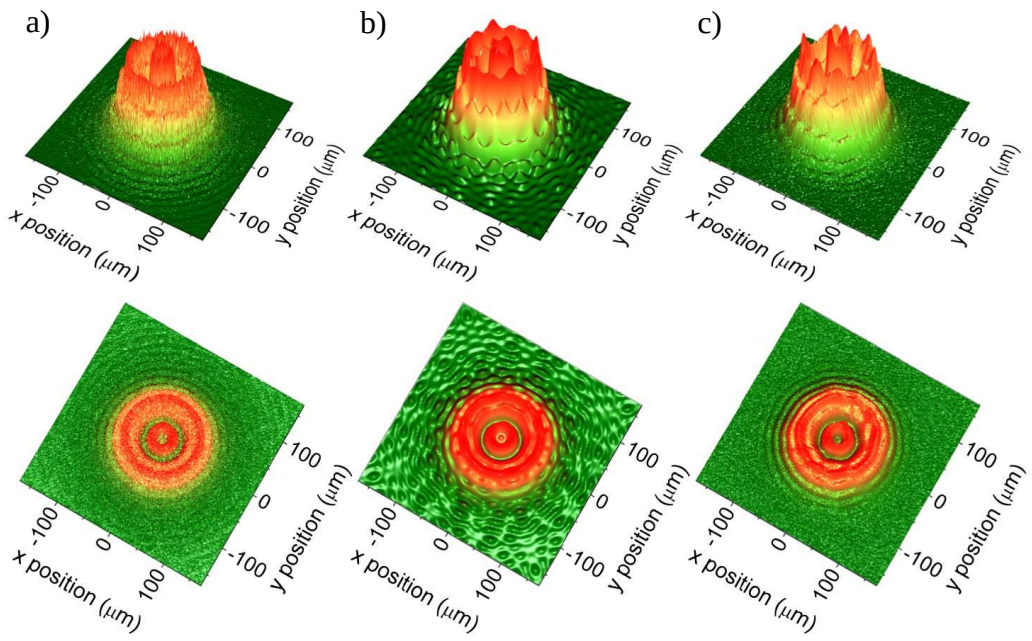

Figure A.11: *(Color online) Diffraction fringes computed (a) using the MCRT method, (b) using Fresnel theory, and (c) measured corresponding to normal illumination of a 200-μm diameter circular aperture by a 351-nm laser with a screen distance of z = 7.6 mm (F = 5.48).*

A comparison between the experimental data and the theoretical models has been performed by a careful application of standard statistical analysis including the adjusted coefficient of determination, R^2_{adj}, the root-mean-square deviation, RMSD, and the reduced chi-square statistics, χ^2_ν. In statistics, the most common measure is the coefficient of determination, R^2, that gives information about the goodness of fit of a model. The R^2 coefficient of determination provides an estimation of how well observed results are replicated by the model, based on the proportion of total variation of theoretical values.[202]

$$R^2 = 1 - \frac{RSS}{TSS} = 1 - \frac{\sum_{i=0}^{N} \left(I_i^{\text{exp}} - I_i^{\text{mod}}\right)^2}{\sum_{i=0}^{N} \left(I_i^{\text{exp}} - \bar{I}\right)^2} \qquad (11)$$

where *RSS* is the residual sum-of-squares, *TSS* is the total sum-of-squares, I_i^{exp} is the i^{th} observed value of *N* observations, I_i^{mod} is the corresponding theoretical value and $\bar{I}$ is mean of the observed data. In general, the larger value of R^2, the better the agreement between experimental results and theoretical model. In the linear context, this measure is very intuitive as values between 0 and 1 provide a ready interpretation of the degree to which the variance in the data is explained by the

theoretical model. The value of R^2 will always increase when a new independent value is added. This is counter to the intuitive expectation that a theoretical model with more independent variables should provide a better fit. To compensate for the possible bias due to different number of parameters, we employ the adjusted coefficient of determination, R^2_{adj}:

$$R^2_{\text{adj}} = 1 - \frac{N-1}{N-p-1} \times (1 - R^2) \qquad (12)$$

where p is independent variables. R^2_{adj} is always smaller than R^2. The independent variables are unknown parameters of our calculations, p = 6, including the slit width, the distance from the aperture to the screen,

the wavelength, the number aperture points, the number of rays traced per aperture point, and the number of bins on the screen. The value of p is much smaller than the number of observations with N = 401.

Using R^2 or adjusted R^2_{adj} alone is not sufficient; it is also necessary to diagnose regression results by a residual analysis. We employ here the root-mean-square deviation (RMSD) or the root-mean square error (RMSE), to assess the quality of a regression. The RMSD is a frequently used measure of differences between values predicted by a model and observed data. The RMSD provides an aggregation of magnitudes of errors between predictions and observed values. Thus, the RMSD,

$$RMSD = \sqrt{\frac{\sum_{i=0}^{N} \left(I_i^{\text{exp}} - I_i^{\text{mod}}\right)^2}{N}} \qquad (13)$$

is a measure of accuracy to compare forecasting errors of different models for a particular data set and not between data sets.

The variance of a least-squares regression analysis is also characterized by the chi-square statistics, χ^2 [36]:

$$\chi^2 = \sum_{i=0}^{N} \frac{\left(I_i^{\text{exp}} - I_i^{\text{mod}}\right)^2}{\sigma_i^2} \qquad (14)$$

where σ_i^2 is the uncertainty in individual measurements, I_i^{exp}. We further define the reduced chi-square, χ_v^2, as a useful measure by:

$$\chi_v^2 = \frac{1}{N-p} \sum_{i=0}^{N} \frac{\left(I_i^{\exp} - I_i^{\mathrm{mod}}\right)^2}{\sigma_i^2} \qquad (15)$$

where, $v = N - p$ is the degrees of freedom. As a general rule, a value of reduced chi-square, $\chi_v^2 \gg 1$, indicates a poor agreement between experimental results and the theoretical model. If the theoretical model is a good approximation, then the variances of both should be in good agreement, and the reduced chi-square should be approximately unity, $\chi_v^2 \sim 1$. If the reduced chi-square is too small, $\chi_v^2 \ll 1$, it may indicate that one has been too pessimistic about measurement errors.

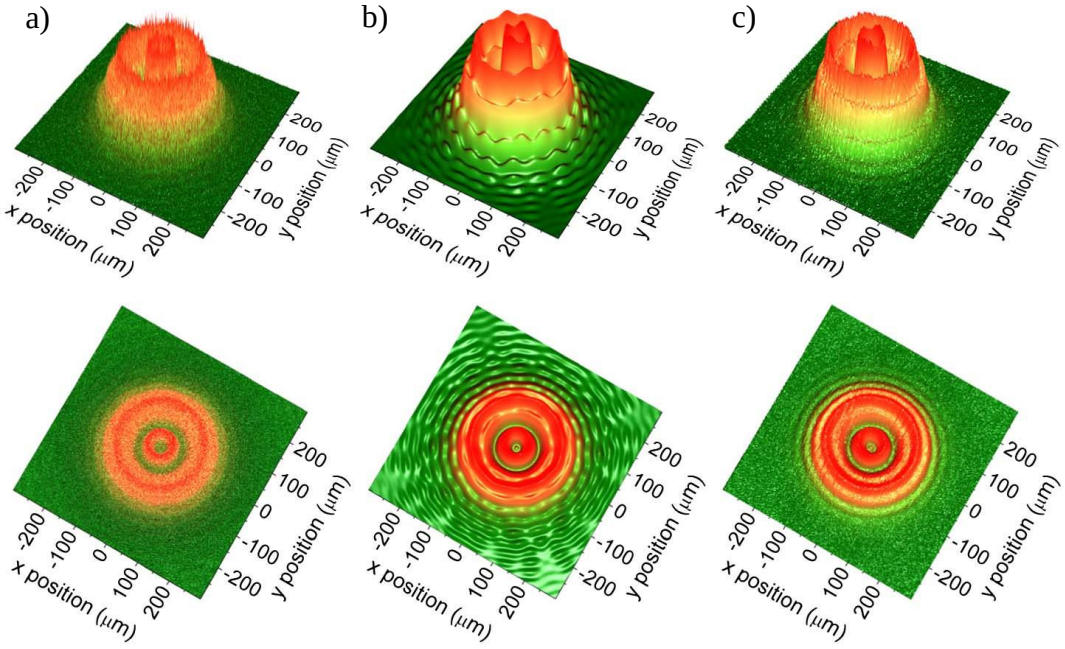

Figure A.12: *(Color online) Diffraction fringes computed (a) using the MCRT method, (b) using Fresnel theory, and (c) measured corresponding to normal illumination of a 400-μm diameter circular aperture by a 351-nm laser with a screen distance of z = 30.4 mm (F = 5.48).*

We have performed least-squares regression analyses including the adjusted coefficient of determination, R_{adj}^2, the root-mean-square deviation, *RMSD*, and the reduced chi-square statistics, χ_v^2, for the MCRT method and the analytical approach to model diffraction irradiation patterns with different distances from apertures to the observation. Table I provides calculation of these parameters for different values of Fresnel numbers and different sizes of single slits. The values of the adjusted coefficient of determination, R_{adj}^2, are near unity. This indicates an excellent

agreement between observation and both the MCRT and Fresnel/Fraunhofer models for the diffraction patterns.

The RMSD is very small for both models. These values also indicate that the MCRT as well as analytical methods are excellent models for the diffraction patterns. The values of the reduced chi-square, χ_{ν}^{2}, are approximately unity. Therefore, statistical analysis confirms the qualitative observation that measured fringe data can be explained very well using both the MCRT method and the Fresnel/Fraunhofer approach. All three statistical methods confirm excellent agreement among the MCRT method, the standard analytical approach, and measured diffraction patterns.

A.7 Conclusions

The obliquity rule based on dipole radiation from each diffraction site produces excellent agreement between the MCRT diffraction model and corresponding experimental results when care is taken to assure that the screen binning precision in the MCRT model matches the experimental measurement precision.

References

1. Akinwande D, *et al.* Graphene and two-dimensional materials for silicon technology. *Nature* **573**, 507 (2019).
2. Tong L, *et al.* Subwavelength-diameter silica wires for low-loss optical wave guiding. *Nature* **426**, 816 (2003).
3. J. W. High-Speed Silicon Photonics Modulators. *Proceedings of the IEEE* **106**, 2158 (2018).
4. Lourenco MA, Gwilliam RM, Homewood KP. Extraordinary optical gain from silicon implanted with erbium. *Appl Phys Lett* **91**, 141122 (2007).
5. Vinh NQ, Ha NN, Gregorkiewicz T. Photonic Properties of Er-Doped Crystalline Silicon. *P IEEE* **97**, 1269 (2009).
6. Przybylinska H, *et al.* Optically active erbium centers in silicon. *Phys Rev B* **54**, 2532 (1996).
7. Vinh NQ, Przybylinska H, Krasil'nik ZF, Gregorkiewicz T. Optical properties of a single type of optically active center in Si/Si:Er nanostructures. *Phys Rev B* **70**, 115332 (2004).
8. Dieke GH. *Spectra and energy levels of rare earth ions in crystals*. Wiley, New York (1968).
9. Kenyon AJ. Recent developments in rare-earth doped materials for optoelectronics. *Prog Quant Electron* **26**, 225 (2002).
10. Wojdak M, *et al.* Sensitization of Er luminescence by Si nanoclusters. *Phys Rev B* **69**, 233315 (2004).
11. Han HS, Seo SY, Shin JH. Optical gain at 1.54 mu m in erbium-doped silicon nanocluster sensitized waveguide. *Appl Phys Lett* **79**, 4568 (2001).
12. Daldosso N, *et al.* Role of the interface region on the optoelectronic properties of silicon nanocrystals embedded in SiO_2. *Phys Rev B* **68**, 085327 (2003).
13. Oton CJ, Loh WH, Kenyon AJ. Er(3+) excited state absorption and the low fraction of nanocluster-excitable Er(3+) in SiO(x). *Appl Phys Lett* **89**, 031116 (2006).
14. Favennec PN, Lharidon H, Salvi M, Moutonnet D, Leguillou Y. Luminescence of Erbium Implanted in Various Semiconductors - IV-Materials, III-V-Materials and II-VI Materials. *Electron Lett* **25**, 718 (1989).

15. Elmasry F, Okubo S, Ohta H, Fujiwara Y. Electron spin resonance study of Er-concentration effect in GaAs; Er, O containing charge carriers. *J Appl Phys* **115**, 193904 (2014).
16. Miniscalco WJ. Erbium-Doped Glasses for Fiber Amplifiers at 1500-nm. *J Lightwave Technol* **9**, 234 (1991).
17. Feng IW, *et al.* Photonic properties of erbium doped InGaN alloys grown on Si (001) substrates. *Appl Phys Lett* **98**, 081102 (2011).
18. Ugolini C, Nepal N, Lin JY, Jiang HX, Zavada JM. Erbium-doped GaN epilayers synthesized by metal-organic chemical vapor deposition. *Appl Phys Lett* **89**, 151903 (2006).
19. Ho VX, *et al.* Photoluminescence quantum efficiency of Er optical centers in GaN epilayers. *Sci Rep-Uk* **7**, 39997 (2017).
20. Ho VX, Al Tahtamouni TM, Jiang HX, Lin JY, Zavada JM, Vinh NQ. Room-Temperature Lasing Action in GaN Quantum Wells in the Infrared 1.5 mu m Region. *Acs Photonics* **5**, 1303 (2018).
21. Shibata H, *et al.* High thermal conductivity of gallium nitride (GaN) crystals grown by HVPE process. *Mater Trans* **48**, 2782 (2007).
22. Roder C, Einfeldt S, Figge S, Hommel D. Temperature dependence of the thermal expansion of GaN. *Phys Rev B* **72**, 085218 (2005).
23. Reeber RR, Wang K. Lattice parameters and thermal expansion of GaN. *J Mater Res* **15**, 40 (2000).
24. *Group IV Elements, IV-IV and III-V Compounds. Part b - Electronic, Transport, Optical and Other Properties*. Springer, Berlin, Heidelberg (2002).
25. Kim JH, Seong D, Ihm GH, Rhee C. Measurement of the thermal conductivity of Si and GaAs wafers using the photothermal displacement technique. *Int J Thermophys* **19**, 281 (1998).
26. Zagumennyi AI, Lutts GB, Popov PA, Sirota NN, Shcherbakov IA. The Thermal Conductivity of YAG and YSAG Laser Crystals. *Laser Phys* **3**, 1064 (1993).
27. Furuse H, Yasuhara R, Hiraga K. Thermo-optic properties of ceramic YAG at high temperatures. *Opt Mater Express* **4**, 1794 (2014).
28. Frindt RFY, A. D. Physical properties of layer structures: Optical properties and photoconductivity of thin crystals of molybdenum disulphide. *Proc R Soc A* **273**, 69 (1963).
29. Joensen P, Frindt, R. F. & Morrison, S. R. Single-layer MoS2. *Mater Res Bull* **21**, 457 (1986).

30. Novoselov KS, *et al.* Electric field effect in atomically thin carbon films. *Science* **306**, 666 (2004).
31. Novoselov KS, *et al.* Two-dimensional gas of massless Dirac fermions in graphene. *Nature* **438**, 197 (2005).
32. Dawlaty JMea. Measurement of the optical absorption spectra of epitaxial graphene from terahertz to visible. *Appl Phys Lett* **93**, 131905 (2008).
33. Mueller T, Xia, F. & Avouris, P. Graphene photodetectors for high-speed optical communications. *Nature Photon* **4**, 297 (2010).
34. Nair RR, *et al.* Fine structure constant defines visual transparency of graphene. *Science* **320**, 1308 (2008).
35. Kuzmenko AB, van Heumen E, Carbone F, van der Marel D. Universal optical conductance of graphite. *Phys Rev Lett* **100**, 117401 (2008).
36. Castro Neto AH, Guinea, F., Peres, N.M.R., Novoselov, K.S. & Geim, A.K. The electronic properties of graphene. *Rev Mod Phys* , **81**, 109 (2009).
37. Das Sarma S, Adam, S., Hwang, E.H. & Rossi, E. Electronic transport in two dimensional graphene. *Rev Mod Phys* **83**, 407 (2011).
38. Wallace PR. The band theory of graphite. *Physical Review* **71**, 622 (1947).
39. Wang L, *et al.* One-dimensional electrical contact to a two-dimensional material. *Science* **342**, 614 (2013).
40. Chen JH, Jang C, Xiao S, Ishigami M, Fuhrer MS. Intrinsic and extrinsic performance limits of graphene devices on SiO_2. *Nat Nanotechnol* **3**, 206 (2008).
41. Dean CR, *et al.* Boron nitride substrates for high-quality graphene electronics. *Nat Nanotechnol* **5**, 722 (2010).
42. Bennett BR, Magno R, Boos JB, Kruppa W, Ancona MG. Antimonide-based compound semiconductors for electronic devices: A review. *Solid State Electron* **49**, 1875 (2005).
43. Lyon TJ, *et al.* Probing Electron Spin Resonance in Monolayer Graphene. *Phys Rev Lett* **119**, 066802 (2017).
44. Mak KF, Sfeir MY, Misewich JA, Heinz TF. The evolution of electronic structure in few-layer graphene revealed by optical spectroscopy. *Proc Natl Acad Sci U S A* **107**, 14999 (2010).
45. Efetov DK, Kim P. Controlling Electron-Phonon Interactions in Graphene at Ultrahigh Carrier Densities. *Phys Rev Lett* **105**, (2010).

46. Low T, Avouris P. Graphene plasmonics for terahertz to mid-infrared applications. *ACS Nano* **8**, 1086 (2014).
47. Dawlaty JM, Shivaraman, S., Chandrashekhar, M., Rana, F. & Spencer, M. G. Measurement of ultrafast carrier dynamics in epitaxial graphene. *Appl Phys Lett* **92**, 42116 (2008).
48. Ping Ma YS, Benedikt Baeuerle, Arne Josten, Wolfgang Heni, Alexandros Emboras, Juerg Leuthold. Plasmonically Enhanced Graphene Photodetector Featuring 100 Gbit/s Data Reception, High Responsivity, and Compact Size. *ACS Photonics* **6**, 154 (2019).
49. Gan X, Shiue, R., Gao, Y., Meric, I., Heinz, T. F., Shepard, K., Hone, J., Assefa, S., Englund, D. Chip-integrated ultrafast graphene photodetector with high responsivity. *Nature Photon* **7**, 883 (2013).
50. Qin Y, *et al.* Lightweight, Superelastic, and Mechanically Flexible Graphene/Polyimide Nanocomposite Foam for Strain Sensor Application. *ACS Nano* **9**, 8933 (2015).
51. Russell Kai Liang Tan SPR, Niloofar Hashemi, Deepak George Thomas, Emrah Kavak, Reza Montazami, Nicole N. Hashemi Graphene as a flexible electrode: review of fabrication approaches. *J Mater Chem A* **5**, 17777 (2017).
52. Winnerl S, *et al.* Carrier relaxation in epitaxial graphene photoexcited near the Dirac point. *Phys Rev Lett* **107**, 237401 (2011).
53. Park J, Ahn YH, Ruiz-Vargas C. Imaging of photocurrent generation and collection in single-layer graphene. *Nano Lett* **9**, 1742 (2009).
54. Furchi M, *et al.* Microcavity-integrated graphene photodetector. *Nano Lett* **12**, 2773 (2012).
55. Muench JE, *et al.* Waveguide-Integrated, Plasmonic Enhanced Graphene Photodetectors. *Nano Lett* **19**, 7632 (2019).
56. Alcaraz Iranzo D, *et al.* Probing the ultimate plasmon confinement limits with a van der Waals heterostructure. *Science* **360**, 291 (2018).
57. Ni Z, *et al.* Plasmonic Silicon Quantum Dots Enabled High-Sensitivity Ultrabroadband Photodetection of Graphene-Based Hybrid Phototransistors. *ACS Nano* **11**, 9854 (2017).
58. Konstantatos G, *et al.* Hybrid graphene-quantum dot phototransistors with ultrahigh gain. *Nat Nanotechnol* **7**, 363 (2012).
59. Xu H, *et al.* High Detectivity and Transparent Few-Layer MoS_2 /Glassy-Graphene Heterostructure Photodetectors. *Adv Mater* **30**, e1706561 (2018).

60. Roy K, *et al.* Graphene-MoS_2 hybrid structures for multifunctional photoresponsive memory devices. *Nat Nanotechnol* **8**, 826 (2013).
61. Yu WJ, *et al.* Highly efficient gate-tunable photocurrent generation in vertical heterostructures of layered materials. *Nat Nanotechnol* **8**, 952 (2013).
62. Britnell L, *et al.* Strong light-matter interactions in heterostructures of atomically thin films. *Science* **340**, 1311 (2013).
63. Environmental Research Institute of Michigan. Infrared Information and Analysis (IRIA) Center., Wolfe WL, Zissis GJ, United States. Office of Naval Research. *The infrared handbook*. The Office (1978).
64. Vincent JD. *Fundamentals of infrared and visible detector operation and testing*, Second edition. edn. Wiley (2016).
65. Saleh BEA, Teich MC. *Fundamentals of photonics*, 2nd edn. Wiley Interscience (2007).
66. Rogalski A. Graphene-based materials in the infrared and terahertz detector families: a tutorial. *Adv Opt Photonics* **11**, 314 (2019).
67. Kufer D, Konstantatos G. Photo-FETs: Phototransistors Enabled by 2D and OD Nanomaterials. *Acs Photonics* **3**, 2197 (2016).
68. Al Tahtamouni TM, Stachowicz M, Li J, Lin JY, Jiang HX. Dramatic enhancement of 1.54 μm emission in Er doped GaN quantum well structures. *Appl Phys Lett* **106**, 121106 (2015).
69. Nishio J, Sugiura L, Fujimoto H, Kokubun Y, Itaya K. Characterization of InGaN multiquantum well structures for blue semiconductor laser diodes. *Appl Phys Lett* **70**, 3431 (1997).
70. Zeng KC, Li J, Lin JY, Jiang HX. Well-width dependence of the quantum efficiencies of $GaN/Al_xGa_{1-x}N$ multiple quantum wells. *Appl Phys Lett* **76**, 3040 (2000).
71. Ugolini C, Feng IW, Sedhain A, Lin JY, Jiang HX, Zavada JM. Formation energy of optically active Er^{3+} centers in Er doped GaN. *Appl Phys Lett* **101**, 051114 (2012).
72. Ugolini C, Nepal N, Lin JY, Jiang HX, Zavada JM. Excitation dynamics of the 1.54 μm emission in Er doped GaN synthesized by metal organic chemical vapor deposition. *Appl Phys Lett* **90**, 051110 (2007).
73. Dahal R, Lin JY, Jiang HX, Zavada JM. Er-Doped GaN and $In_xGa_{1-x}N$ for Optical Communications. *Top Appl Phys* **124**, 115 (2010).

74. George DK, *et al.* Excitation mechanisms of Er optical centers in GaN epilayers. *Appl Phys Lett* **107**, 171105 (2015).
75. Dahal R, Ugolini C, Lin JY, Jiang HX, Zavada JM. 1.54 μm emitters based on erbium doped InGaN p-i-n junctions. *Appl Phys Lett* **97**, 141109 (2010).
76. Steckl AJ, Park JH, Zavada JM. Prospects for rare earth doped GaN lasers on Si. *Mater Today* **10**, 20 (2007).
77. O'Donnell K, Dierolf V. *Rare-Earth Doped III-Nitrides for Optoelectronic and Spintronic Applications*. Springer (2010).
78. Steckl AJ, Zavada JM. Optoelectronic properties and applications of rare-earth-doped GaN. *Mrs Bull* **24**, 33 (1999).
79. Vinh NQ, Minissale S, Vrielinck H, Gregorkiewicz T. Concentration of Er^{3+} ions contributing to 1.5-μm emission in Si/Si:Er nanolayers. *Phys Rev B* **76**, 085339 (2007).
80. de Boer WDAM, McGonigle C, Gregorkiewicz T, Fujiwara Y, Tanabe S, Stallinga P. Optical excitation and external photoluminescence quantum efficiency of Eu^{3+} in GaN. *Sci Rep-Uk* **4**, 5235 (2014).
81. Denis A, Goglio G, Demazeau G. Gallium nitride bulk crystal growth processes: A review. *Mat Sci Eng R* **50**, 167 (2006).
82. Wang YQ, Steckl AJ. Three-color integration on rare-earth-doped GaN electroluminescent thin films. *Appl Phys Lett* **82**, 502 (2003).
83. Braud A, Doualan JL, Moncorge R, Pipeleers B, Vantomme A. Er-defect complexes and isolated Er center spectroscopy in Er-implanted GaN. *Mat Sci Eng B-Solid* **105**, 101 (2003).
84. Braud A. Excitation Mechanisms of RE Ions in Semiconductors. *Top Appl Phys* **124**, 269-307 (2010).
85. Lorenz K, Alves E, Gloux F, Ruterana P. RE Implantation and Annealing of III-Nitrides. *Top Appl Phys* **124**, 25 (2010).
86. Hansen DM, *et al.* Photoluminescence of erbium-implanted GaN and in situ-doped GaN:Er. *Appl Phys Lett* **72**, 1244 (1998).
87. Garter M, Scofield J, Birkhahn R, Steckl AJ. Visible and infrared rare-earth-activated electroluminescence from indium tin oxide Schottky diodes to GaN:Er on Si. *Appl Phys Lett* **74**, 182 (1999).

88. Makarova K, *et al.* Spectroscopic studies of Er-centers in MOCVD grown GaN layers highly doped with Er. *Mat Sci Eng B-Solid* **146**, 193 (2008).
89. Glukhanyuk V, Przybylinska H, Kozanecki A, Jantsch W. Optical properties of a single Er center in GaN. *Opt Mater* **28**, 746 (2006).
90. Stachowicz M, *et al.* Crystal field analysis of rare-earth ions energy levels in GaN. *Opt Mater* **37**, 165 (2014).
91. Bodiou L, Braud A. Direct evidence of trap-mediated excitation in GaN:Er(3+) with a two-color experiment. *Appl Phys Lett* **93**, 151107 (2008).
92. Song SF, *et al.* Electrical characterization of Er- and Pr-implanted GaN films. *Appl Phys Lett* **86**, 152111 (2005).
93. Filhol JS, Jones R, Shaw MJ, Briddon PR. Structure and electrical activity of rare-earth dopants in GaN. *Appl Phys Lett* **84**, 2841 (2004).
94. Dai HX, Pan JY, Lin CL. All-optical gain control of in-line erbium-doped fiber amplifiers for hybrid analog/digital WDM systems. *Ieee Photonic Tech L* **9**, 737 (1997).
95. Thomas DG, Hopfield JJ, Frosch CJ. Isoelectronic Traps Due to Nitrogen in Gallium Phosphide. *Phys Rev Lett* **15**, 857 (1965).
96. Klik MAJ, Gregorkiewicz T, Bradley IV, Wells JPR. Optically induced deexcitation of rare-earth ions in a semiconductor matrix. *Phys Rev Lett* **89**, 227401 (2002).
97. Takahei K, Taguchi A, Nakagome H, Uwai K, Whitney PS. Intra-4f-Shell Luminescence Excitation and Quenching Mechanism of Yb in Inp. *J Appl Phys* **66**, 4941 (1989).
98. Needels M, Schluter M, Lannoo M. Erbium Point-Defects in Silicon. *Phys Rev B* **47**, 15533 (1993).
99. Hoang K. First-principles identification of defect levels in Er-doped GaN. *Phys Status Solidi RRL*, **10**, 915 (2016).
100. Wang Q, Hui R, Dahal R, Lin JY, Jiang HX. Carrier lifetime in erbium-doped GaN waveguide emitting in 1540 nm wavelength. *Appl Phys Lett* **97**, 241105 (2010).
101. Feng IW, Li J, Lin JY, Jiang HX, Zavada J. Optical excitation cross section of erbium in GaN. *Appl Optics* **52**, 1132 (2013).
102. Priolo F, Franzo G, Coffa S, Carnera A. Excitation and nonradiative deexcitation processes of Er^{3+} in crystalline Si. *Phys Rev B* **57**, 4443 (1998).

103. Nepal N, *et al.* Optical enhancement of room temperature ferromagnetism in Er-doped GaN epilayers. *Appl Phys Lett* **95**, 022510 (2009).
104. Kenyon AJ. Erbium in silicon. *Semicond Sci Tech* **20**, R65 (2005).
105. Steckl AJ, *et al.* Rare-earth-doped GaN: Growth, properties, and fabrication of electroluminescent devices. *Ieee J Sel Top Quant* **8**, 749 (2002).
106. Shaklee KL, Leheny RF. Direct Determination of Optical Gain in Semiconductor Crystals. *Appl Phys Lett* **18**, 475 (1971).
107. Johnson JC, Choi HJ, Knutsen KP, Schaller RD, Yang PD, Saykally RJ. Single gallium nitride nanowire lasers. *Nat Mater* **1**, 106 (2002).
108. McGehee MD, Heeger AJ. Semiconducting (conjugated) polymers as materials for solid-state lasers. *Adv Mater* **12**, 1655 (2000).
109. Strauf S, *et al.* Self-tuned quantum dot gain in photonic crystal lasers. *Phys Rev Lett* **96**, 127404 (2006).
110. Bjork G, Karlsson A, Yamamoto Y. Definition of a Laser Threshold. *Phys Rev A* **50**, 1675 (1994).
111. Tessler N. Lasers based on semiconducting organic materials. *Adv Mater* **11**, 363 (1999).
112. Coldren LA, Corzine SW. *Diode Lasers and Photonic Integrated Circuits*. Wiley (1995).
113. Siegman AE. *Lasers* (1986).
114. Liu AS, *et al.* A high-speed silicon optical modulator based on a metal-oxide-semiconductor capacitor. *Nature* **427**, 615 (2004).
115. Xu QF, Schmidt B, Pradhan S, Lipson M. Micrometre-scale silicon electro-optic modulator. *Nature* **435**, 325 (2005).
116. Assefa S, Xia FNA, Vlasov YA. Reinventing germanium avalanche photodetector for nanophotonic on-chip optical interconnects. *Nature* **464**, 80 (2010).
117. Xia FN, Sekaric L, Vlasov Y. Ultracompact optical buffers on a silicon chip. *Nat Photonics* **1**, 65 (2007).
118. Pavlov SG, *et al.* Stimulated emission from donor transitions in silicon. *Phys Rev Lett* **84**, 5220 (2000).
119. Rong HS, *et al.* A continuous-wave Raman silicon laser. *Nature* **433**, 725 (2005).
120. Pavesi L, Dal Negro L, Mazzoleni C, Franzo G, Priolo F. Optical gain in silicon nanocrystals. *Nature* **408**, 440 (2000).

121. Cloutier SG, Kossyrev PA, Xu J. Optical gain and stimulated emission in periodic nanopatterned crystalline silicon. *Nat Mater* **4**, 887 (2005).
122. Wirths S, *et al.* Lasing in direct-bandgap GeSn alloy grown on Si. *Nat Photonics* **9**, 88 (2015).
123. Grydlik M, *et al.* Lasing from Glassy Ge Quantum Dots in Crystalline Si. *Acs Photonics* **3**, 298 (2016).
124. Grydlik M, *et al.* Laser Level Scheme of Self-Interstitials in Epitaxial Ge Dots Encapsulated in Si. *Nano Lett* **16**, 6802 (2016).
125. Chen R, *et al.* Nanolasers grown on silicon. *Nat Photonics* **5**, 170 (2011).
126. Sun Y, *et al.* Room-temperature continuous-wave electrically injected InGaN-based laser directly grown on Si. *Nat Photonics* **10**, 595 (2016).
127. Vinh NQ, Przybylinska H, Krasil'nik ZF, Gregorkiewicz T. Microscopic structure of Er-related optically active centers in crystalline silicon. *Phys Rev Lett* **90**, 066401 (2003).
128. Krasilnik ZF, *et al.* Erbium doped silicon single- and multilayer structures for light-emitting device and laser applications. *J Mater Res* **21**, 574 (2006).
129. Feng IW, Li J, Sedhain A, Lin JY, Jiang HX, Zavada J. Enhancing erbium emission by strain engineering in GaN heteroepitaxial layers. *Appl Phys Lett* **96**, 031908 (2010).
130. Dahal R, Ugolini C, Lin JY, Jiang HX, Zavada JM. 1.54 um emitters based on erbium doped InGaN p-i-n junctions. *Appl Phys Lett* **97**, 141109 (2010).
131. Ramvall P, Tanaka S, Nomura S, Riblet P, Aoyagi Y. Observation of confinement-dependent exciton binding energy of GaN quantum dots. *Appl Phys Lett* **73**, 1104 (1998).
132. Look DC, Sizelove JR. Predicted maximum mobility in bulk GaN. *Appl Phys Lett* **79**, 1133 (2001).
133. Cao Y, Jena D. High-mobility window for two-dimensional electron gases at ultrathin AlN/GaN heterojunctions. *Appl Phys Lett* **90**, 182112 (2007).
134. Ho VX, *et al.* Temperature dependence studies of Er optical centers in GaN epilayers grown by MOCVD. *Mrs Advances* **2**, 135 (2017).
135. Xing GC, *et al.* Low-temperature solution-processed wavelength-tunable perovskites for lasing. *Nat Mater* **13**, 476 (2014).
136. Wu SF, *et al.* Monolayer semiconductor nanocavity lasers with ultralow thresholds. *Nature* **520**, 69 (2015).

137. Li MJ, *et al.* Ultralow-threshold multiphoton-pumped lasing from colloidal nanoplatelets in solution. *Nat Commun* **6**, 8513 (2015).
138. Strauf S, *et al.* Self-tuned quantum dot gain in photonic crystal lasers. *Phys Rev Lett* **96**, 127404 (2006).
139. Koppens FHL, Mueller T, Avouris P, Ferrari AC, Vitiello MS, Polini M. Photodetectors based on graphene, other two-dimensional materials and hybrid systems. *Nat Nanotechnol* **9**, 780 (2014).
140. Bonaccorso F, Sun Z, Hasan T, Ferrari AC. Graphene photonics and optoelectronics. *Nat Photonics* **4**, 611 (2010).
141. Novoselov KS, *et al.* Two-dimensional atomic crystals. *P Natl Acad Sci USA* **102**, 10451 (2005).
142. Urich A, Unterrainer K, Mueller T. Intrinsic Response Time of Graphene Photodetectors. *Nano Lett* **11**, 2804 (2011).
143. Park J, Ahn YH, Ruiz-Vargas C. Imaging of Photocurrent Generation and Collection in Single-Layer Graphene. *Nano Lett* **9**, 1742 (2009).
144. Freitag M, Low T, Xia FN, Avouris P. Photoconductivity of biased graphene. *Nat Photonics* **7**, 53 (2013).
145. Nikitskiy I, *et al.* Integrating an electrically active colloidal quantum dot photodiode with a graphene phototransistor. *Nat Commun* **7**, 11954 (2016).
146. Liu CH, Chang YC, Norris TB, Zhong ZH. Graphene photodetectors with ultra-broadband and high responsivity at room temperature. *Nat Nanotechnol* **9**, 273 (2014).
147. Kagan CR, Lifshitz E, Sargent EH, Talapin DV. Building devices from colloidal quantum dots. *Science* **353**, (2016).
148. Konstantatos G, *et al.* Hybrid graphene-quantum dot phototransistors with ultrahigh gain. *Nat Nanotechnol* **7**, 363 (2012).
149. Yu XC, *et al.* Narrow bandgap oxide nanoparticles coupled with graphene for high performance mid-infrared photodetection. *Nat Commun* **9**, 4299 (2018).
150. Ni ZY, *et al.* Plasmonic Silicon Quantum Dots Enabled High-Sensitivity Ultrabroadband Photodetection of Graphene-Based Hybrid Phototransistors. *Acs Nano* **11**, 9854 (2017).

151. Sun ZH, Liu ZK, Li JH, Tai GA, Lau SP, Yan F. Infrared Photodetectors Based on CVD-Grown Graphene and PbS Quantum Dots with Ultrahigh Responsivity. *Adv Mater* **24**, 5878 (2012).
152. Guo WH, Xu SG, Wu ZF, Wang N, Loy MMT, Du SW. Oxygen-Assisted Charge Transfer Between ZnO Quantum Dots and Graphene. *Small* **9**, 3031 (2013).
153. Chen ZF, *et al.* High Responsivity, Broadband, and Fast Graphene/Silicon Photodetector in Photoconductor Mode. *Adv Opt Mater* **3**, 1207 (2015).
154. Chen SY, *et al.* Biologically inspired graphene-chlorophyll phototransistors with high gain. *Carbon* **63**, 23 (2013).
155. Marschall R, Wang LZ. Non-metal doping of transition metal oxides for visible-light photocatalysis. *Catal Today* **225**, 111 (2014).
156. Park GS, *et al.* In situ observation of filamentary conducting channels in an asymmetric Ta_2O_{5-x}/TaO_{2-x} bilayer structure. *Nat Commun* **4**, 2382 (2013).
157. Gritsenko VA, *et al.* Charge Transport and the Nature of Traps in Oxygen Deficient Tantalum Oxide. *Acs Appl Mater Inter* **10**, 3769 (2018).
158. Gu TK, Tada T, Watanabe S. Conductive Path Formation in the Ta_2O_5 Atomic Switch: First-Principles Analyses. *Acs Nano* **4**, 6477 (2010).
159. Freeman Y. *Tantalum and Niobium-Based Capacitors: Science, Technology, and Applications*. Springer; 1st Ed. (2018).
160. Alimardani N, King S, French BL, Tan C, Lampert BP, Conley JF. Investigation of the impact of insulator material on the performance of dissimilar electrode metal-insulator-metal diodes. *J Appl Phys* **116**, (2014).
161. Kozawaguchi H, Tsujiyama B, Murase K. Thin-Film Electroluminescent Device Employing Ta_2O_5 Rf Sputtered Insulating Film. *Jpn J Appl Phys* **21**, 1028 (1982).
162. Graf D, *et al.* Raman mapping of a single-layer to double-layer graphene transition. *Eur Phys J-Spec Top* **148**, 171 (2007).
163. Friedemann M, *et al.* Versatile sputtering technology for Al2O3 gate insulators on graphene. *Sci Technol Adv Mat* **13**, 025007 (2012).
164. Lemme MC, *et al.* Gate-Activated Photoresponse in a Graphene p-n Junction. *Nano Lett* **11**, 4134 (2011).

165. Peters EC, Lee EJH, Burghard M, Kern K. Gate dependent photocurrents at a graphene p-n junction. *Appl Phys Lett* **97**, 193102 (2010).
166. Shin H, Park SY, Bae ST, Lee S, Hong KS, Jung HS. Defect energy levels in Ta_2O_5 and nitrogen-doped Ta_2O_5. *J Appl Phys* **104**, 116108 (2008).
167. Morikawa T, Saeki S, Suzuki T, Kajino T, Motohiro T. Dual functional modification by N doping of Ta_2O_5: p-type conduction in visible-light-activated N-doped Ta_2O_5. *Appl Phys Lett* **96**, 142111 (2010).
168. Bondi RJ, Fox BP, Marinella MJ. Non-metallic dopant modulation of conductivity in substoichiometric tantalum pentoxide: A first-principles study. *J Appl Phys* **121**, 214102 (2017).
169. Yamanaka K, Sato S, Iwaki M, Kajino T, Morikawa T. Photoinduced Electron Transfer from Nitrogen-Doped Tantalum Oxide to Adsorbed Ruthenium Complex. *J Phys Chem C* **115**, 18348 (2011).
170. Murase T, Irie H, Hashimoto K. Visible light sensitive photocatalysts, nitrogen-doped Ta_2O_5 powders. *J Phys Chem B* **108**, 15803 (2004).
171. Ho VX, Wang Y, Cooney MP, Vinh NQ. Graphene-based photodetector at room temperature. *Proceedings of SPIE* **10729**, 1072907 (2018).
172. Liu JJ, Yin YL, Yu LH, Shi YC, Liang D, Dai DX. Silicon-graphene conductive photodetector with ultra-high responsivity. *Sci Rep-Uk* **7**, 40904 (2017).
173. Yu QK, *et al.* Control and characterization of individual grains and grain boundaries in graphene grown by chemical vapour deposition. *Nat Mater* **10**, 443 (2011).
174. Ullah R, Sun HQ, Ang HM, Tade MO, Wang SB. Comparative Investigation of Photocatalytic Degradation of Toluene on Nitrogen Doped Ta_2O_5 and Nb_2O_5 Nanoparticles. *Ind Eng Chem Res* **52**, 3320 (2013).
175. Chun WJ, *et al.* Conduction and valence band positions of Ta_2O_5, TaON, and Ta_3N_5 by UPS and electrochemical methods. *J Phys Chem B* **107**, 1798 (2003).
176. Irie H, Watanabe Y, Hashimoto K. Nitrogen-concentration dependence on photocatalytic activity of $TiO_{2-x}N_x$ powders. *J Phys Chem B* **107**, 5483 (2003).
177. Zhang YZ, *et al.* Broadband high photoresponse from pure monolayer graphene photodetector. *Nat Commun* **4**, 1811 (2013).

178. Yu XC, *et al.* A high performance, visible to mid-infrared photodetector based on graphene nanoribbons passivated with HfO_2. *Nanoscale* **8**, 327 (2016).
179. Yu XC, *et al.* Atomically thin noble metal dichalcogenide: a broadband mid-infrared semiconductor. *Nat Commun* **9**, 1545 (2018).
180. Chen XL, *et al.* Widely tunable black phosphorus mid-infrared photodetector. *Nat Commun* **8**, 1672 (2017).
181. Long MS, *et al.* Room temperature high-detectivity mid-infrared photodetectors based on black arsenic phosphorus. *Sci Adv* **3**, 1700589 (2017).
182. Chou TS. Monte-Carlo Approach to Optical Analysis. *Opt Eng* **13**, 299 (1974).
183. Tira NE, Mahan JR, Lee RB. Dynamic Electrothermal Model for the Earth Radiation Budget Experiment Nonscanning Radiometer with Applications to Solar Observations and Evaluation of Thermal Noise. *Opt Eng* **29**, 351 (1990).
184. Haeffelin MPA, Mahan JR, Tira NE, Meekins JL, Lee RB, Keynton RJ. High-order end-to-end model for the ERBE scanning thermistor bolometer radiometers. *SPIE, Passive Infrared Remote Sensing of Clouds and the Atmosphere* **1934**, 150 (1993).
185. Villeneuve PV, Mahan JR. Sensitivity of the earth-atmosphere bidirectional reflectivity functions to variations in cloud parameters *SPIE, Atmospheric Sensing and Modeling II, Paris, France, September 25-28* **2582**, 233 (1995).
186. Priestley KJ, Mahan JR, Haeffelin MPA, Savransky M, Nguyen TK. Thermistor bolometer radiometer signal contamination due to parasitic heat diffusion. *SPIE, Advanced and Next-Generation Satellites* **2583**, 72 (1995).
187. Nester AMS, Haeffelin MPA, Nevarez FJ, Mahan JR, Kato S, Rutledge CK. Experimental and theoretical study of uncertainty in pyranometers for surface radiation. *SPIE, Sensors, Systems, and Next-Generation Satellites III* **3870**, 536 (1999).
188. Coffey KL, Nevarez FJ, Mahan JR, Priestley KJ. Optical model of a next-generation instrument for monitoring atmospheric energetics from space. *SPIE, Design and Engineering of Optical Systems II* **3737**, 180 (1999).
189. Mahan JR. *Radiation Heat Transfer: A Statistical Approach*. John Wiley & Sons, New York, ISBN 0-471-21270-9 (2002).
190. Likeness BK. Stray Light Simulation With Advanced Monte Carlo Techniques. *SPIE, Stray Light Problems in Optical Systems* **0107**, 80 (1977).

191. Volpe FA, Letourneau PD, Zhao A. Huygens-Fresnel wavefront tracing. *Comput Phys Commun* **212**, 123 (2017).
192. Heinisch RP, Chou TS. Numerical Experiments in Modeling Diffraction Phenomena. *Appl Optics* **10**, 2248-& (1971).
193. Coffey KL, Priestley KJ, Mahan JR, Sanchez WC. Diffraction models of radiation entering an aperture for use in a Monte Carlo ray-trace environment *SPIE, Current Developments in Optical Design and Engineering VII* **3429**, 213 (1998).
194. Coffey KL. Next-Generation Earth Radiation Budget Concepts, Master of Science Thesis, Department of Mechanical Engineering, Virginia Polytechnic Institute and State University, Blacksburg, VA. (1998).
195. Hecht E. *Optics*. Fifth edition, Pearson, ISBN 10: 1-292-09693-4 (2017).
196. Mahan JR, Barki AR, Priestley KJ. Diffraction and polarization effects in Earth radiation budget measurements. *Appl Optics* **55**, D54 (2016).
197. Mahan JR, Tira NE, Lee RB, Keynton RJ. Comparison of the Measured and Predicted Response of the Earth Radiation Budget Experiment Active Cavity Radiometer during Solar Observations. *Appl Optics* **28**, 1327 (1989).
198. Mahan JR, Walker JA, Stancil MM. Bidirectional reflection effects in practical integrating spheres. *Appl Optics* **54**, 8951 (2015).
199. Sorensen IJ, Mahan JR, Barry MY, Kist EH. Parameter estimation and optimal design of thermal radiation detectors using engineering prototypes and numerical models *SPIE, Sensors, Systems, and Next-Generation Satellites III* **3870**, 480 (1999).
200. Goodman JW. *Introduction to Fourier Optics*. Fourth edition, W. H. Freeman & Company, New York, ISBN 978-1-319-15304-5 (2017).
201. Born M, Wolf E. *Principles of optics*. Seventh edition, Cambridge University Press (1999).
202. Bevington PR, Robinson DK. *Data reduction and error analysis for the physical sciences*. 2nd Ed. McGraw-Hill (1992).